# Development of Microfluidic Devices for Studying Protein Conformational Dynamics via HDX/TRESI-MS

**TAMANNA ROB**

A dissertation submitted to the Faculty of Graduate Studies in the partial fulfillment of the requirements for the degree of

Doctor of Philosophy

Graduate Program in Chemistry

York University
Toronto, Ontario
June, 2013

# ABSTRACT

Studies of protein conformational dynamics can lead to a deeper understanding of biological functions of proteins, protein/protein interactions, catalysis and allostery. Most of the conformers involved in biological pathways are short-lived. These conformers represent challenging analytical targets since they are weakly populated at equilibrium and demand ultra-rapid online analytical techniques. To address this demand, the development of new tools that will offer enhanced time and spatial resolution in measurements is essential. Towards that end, we took advantage of microfluidics to fabricate custom polymeric devices that would allow direct mass spectrometric measurements of protein dynamics. This dissertation presents successful development of new tools and demonstrates their practical applications in studying dynamics of weakly structured regions of proteins on the millisecond time scale, which is unattainable by conventional biophysical techniques.

This thesis introduces a simple, rapid, inexpensive and easily modifiable fabrication protocol which enables the integration of multiple functionalities on a single platform that accommodates complete ‘bottom up’ continuous/pulse labelling Hydrogen-deuterium exchange (HDX) work flow. These integrated devices can be directly interfaced with mass spectrometry as custom electrospray ionization (ESI) sources to conduct site specific mass spectrometric protein conformational analysis. The continuous HDX labelling device enables structural analysis of ubiquitin and distinguishes loop dynamics in cytochrome c. The effect of ligand binding in conformational dynamics in a molten globule protein DAHP synthase was also monitored *via* continuous HDX labelling. Another analogous device, capable of performing millisecond HDX pulse labelling, reveals allosteric hot spots in TEM-1 which is an antibiotic resistant β-lactamase. Complementary experiments with multiple antibiotics compare the allosteric responses of TEM-1 upon inhibitor or substrate binding. The results exhibit an exciting correlation between allosteric dynamic responses and functionally relevant mutations at the periphery of the protein. This strong correlation demonstrates that this device can be applied in predicting sites of probable mutations. This dissertation successfully introduces integrated microfluidic devices that represent a promising tool for studying dynamics of weakly structured proteins, intrinsically disordered proteins and allostery.

# Dedication

***To those who loved me for who I am-***

Ammu (Prof. Nilufar Nahar), Abbu (MD. Abdur Rob),
Apa (Fahmida Rob Dipa), Shompuni (Farhana Rob Shompa)
Grandma (Rawshon Ara)

Delwar Hossain
And
My cutie pie Rionna Hossain

# Acknowledgement

My heartfelt appreciation and thanks to my advisor Dr. Derek James Wilson for his supervision and advice. Without his support and firm belief in the ‘power of plastic’, this project would not have been possible. Special thanks to him for the freedom he gives to his students - he truly lets his students grow up as a responsible researcher and enjoy the grad school.

I would like thank my committee members, Prof. K.W. Michael Siu and Dr. Gerald Audette for their valuable time, thoughtful criticisms and suggestions.

I am also thankful Prof. Paul Berti and his student Naresh Balachandran from McMaster University for providing purified DAHP synthase.

I am grateful to Dr. Dasantila Golemi-Kotra for allowing me to work with TEM-1 enzyme. Her insightful discussions and suggestions motivated me to see through the data in a different perspective. I owe her special thanks for her loving encouragement and support to me and my family during our time at York.

Thanks to all the present and past members of Wilson group. It is a privilege to be a part of such an awesome team. I would also like to extend my thanks to all present and past members of CRMS. I am grateful to all of them for their friendship, sharing the best and worst moments of my doctoral journey and making my grad life more enjoyable. I would like to specially thank Yanfang Liang, Peter Liuni and Irine Saminathan for their support and encouragement to face many academic and personal challenges whenever I needed it the most. I would also like to express my special thanks to two more dear friends: Preet Kamal Gill for burning the candle at both ends to purify TEM-1 enzyme for me and Shaolong Zhu for writing a computer program for analyzing the HDX data. I highly appreciate John P. van Nostrand and Greg Kouniyagi for their constant technical support and sharing their Mass Spec knowledge with me.

I would like to acknowledge NSERC and Department of Chemistry, York University for the scholarship and support. My special thanks to two lovely ladies- Magy Baket and Mary Mamais for their smiles and support. They made my grad life easy in so many ways.

My earnest appreciation goes to my parents and sisters for their unwavering love and support. They set the minimum bar of Ph.D. before I went to kindergarten and finally I am there. I am profoundly in debt to my grandma who convinced me that science is more interesting than painting.

I am deeply thankful to my husband Delwar Hossain for his support, patience and sacrifices. Finally, I want to thank my daughter Rionna for coming to my life. It is a blessing to have a wonderful baby like her!

# List of publications

1. **Rob, T.,** Gill, P.K., Kotra, D. G. and Wilson D.J. (2012) An electrospray MS-coupled microfluidic device for sub-second H/D exchange pulse –labelling reveals allosteric effects in enzyme inhibition. *Lab on a chip,* DOI:10.1039/C3LC00007A **[Chapter 5]**

2. **Rob, T.,** Liuni, P., Gill, P.K., Zhu, S., Balachandran, N., Berti, P., and Wilson D.J. (2012) Measuring Dynamics in weakly structured regions of protein using microfluidics-enabled sub-second H/D exchange Mass Spectrometry. *Analytical Chemistry*, 84(8):3771-3779 **[Chapter 3]**

3. **Rob, T.** and Wilson D.J. (2012) Time-resolved Mass Spectrometry for Monitoring Millisecond Time-scale Solution Phase Processes. *Euro. J. Mass Spectrom.*,18(2): 205-214 (Review)

4. Liuni, P., **Rob, T.** and Wilson D.J. (2010) A microfluidic reactor for rapid, low-pressure proteolysis with on-chip electrospray ionization. *Rapid Commun. Mass Spectrom*. 24(31): 315-320

5. **Rob, T.** and Wilson D.J. (2009) A Versatile Microfluidic Chip for Millisecond Time-scale Kinetic Studies by Electrospray Mass Spectrometry. *JASMS*, 20(1): 124-130 **[Chapter 2]**

# Table of Contents

**Chapter 2. Versatile Microfluidic Chip for Millisecond Time-scale Kinetic Studies by Electrospray Mass Spectrometry** ........................................................................ 42

# List of Figures

# List of Tables

# List of Abbreviations and Symbols

| | |
|---|---|
| AMS | Accelerator Mass Spectrometry |
| B | Magnetic sector |
| CEM | Chain Ejection model |
| CI | Chemical ionization |
| $CO_2$ | Carbon dioxide |
| CRM | Charged Residue model |
| D | Diffusion coefficient |
| DAHP | 3-deoxy-D-arabinoheptulosonate 7-phosphate |
| DC | Direct current |
| DESI | Desorption electrospray ionization |
| E4P | D-erythrose 4-phosphate |
| ECD | Electron capture dissociation |
| EI | Electron ionization |
| EM | Electron microscopy |
| ESI | Electrospray Ionization |
| ETD | Electron transfer dissociation |
| FI | Field ionization |
| FTICR | Fourier transform ion cyclotron resonance |
| FT-OT | Fourier transform orbitrap |
| G3P | Glycerol-3-phosohate |
| IEM | Ion Evaporation model |
| kV | Kilo Volt |
| LASER | Light amplification by stimulated emission of radiation |
| LOC | Lab on a chip |

| | |
|---|---|
| LTQ | Linear quadrupole ion trap |
| MALDI | Matrix-assisted laser desorption ionization |
| MCP | Micro channel plate |
| MF | Microfluidics |
| MS | Mass Spectrometry |
| ms | Millisecond |
| Nd: YAG | Neodymium – yttrium aluminum garnet |
| NMR | Nuclear magnetic resonance |
| PDMS | Poly(dimethylsiloxane) |
| PEP | Phosphoenolpyruvate |
| PF | Protection factor |
| Phe | Phenylalanine |
| PMMA | Poly(methyl methacrylate) |
| Q | Quadrupole mass filter |
| QIT | Quadrupole ion trap |
| Re | Reynolds number |
| RF | Radio frequency |
| TDC | Time-to-digital converters |
| TOF | Time of flight |
| TRESI | Time resolved electrospray Ionization |
| Trp | Tryptophan |
| Tyr | Tyrosine |
| | |
| $t_d$ | Diffusion time |
| *m/z* | Mass-to-charge ratio |
| µTAS | Micro Total Analysis System |

# CHAPTER 1

# INTRODUCTION

## 1.1 Conformational Dynamics

Understanding the structure and dynamics of proteins at molecular level with high resolution is one of the most compelling challenges in bioanalytical chemistry. Proteins are the most important functional biomolecules in biological system. Virtually they participate in almost every process within living organisms- catalyzing metabolic reactions, replicating DNA, responding to stimuli through post translational modification, and transporting molecules from one location to another and many more [1]. Protein molecules are highly dynamic rather than static; they function by changing their conformation ensembles [2, 3]. It is now widely recognized that knowledge about static structure alone is not often sufficient to understand real-time protein functions. The details of *how* proteins do *what* they do – remains one of the challenging questions in biochemistry [4, 5]. This challenge inspired us to improve currently available analytical techniques to investigate protein fluctuations on the millisecond time scale. Using our novel technique, we were able to distinguish dynamic properties of different regions of proteins which are inaccessible *via* current approaches.

Proteins are large biopolymers made of twenty basic amino acids which can be assembled in a very specific permutations and combinations to craft complex proteins. Amino acids are attached together by strong covalent polypeptide bonds forming the backbone of a long chain protein. Nascent proteins are linear polymers that must fold into precise three-dimensional conformations commonly termed as their ‘native’ form which are usually ordered arrangements and low energy conformational ensembles. Rather than undergoing randomized conformational search, initially random coils of protein follow specific folding pathways to achieve highly specific three-dimensional arrangements that are thermodynamically stable under physiological conditions. Folding mechanisms are dictated ultimately by the primary amino acid sequence of protein. Each amino acid has its own unique Chemistries as each of them has a unique functional group in its side chain. Relatively weak noncovalent interactions between side chains and the functional groups of the polypeptide backbone play crucial role in folding process. In order to function, native protein needs to access higher energy conformational ensembles which are relatively less ordered. During folding/unfolding, the protein rearranges itself *via* many ‘transient’ conformations which are structurally and energetically similar to each other but usually indistinguishable by contemporary optical methods.

While rearranging conformations *via* (un)folding mechanisms, proteins may undergo ‘*misfolding*’ to attain thermodynamically more favourable highly ordered states compared to their native states. These transient conformations and misfolded proteins often cause many modified or toxic functionalities resulting in pathological states [6-8]. For example Alzheimer’s, a neurodegenerative disease, is believed to result from the accumulation of amyloid fibrils composed of misfolded proteins. Several other human disease including diabetes, Parkinson’s, Creutzfeldt-Jacob disease and Huntington's disease have also been associated with misfolded proteins [9-12]. Therefore, understanding a protein’s folding mechanism and/or its dynamics can provide insights to combat these critical concerns. Fortunately, experimental and theoretical/computational investigations have resulted in substantial progress in this direction over the past few years.

Scientists have utilized an ‘energy landscape’ of proteins (Figure 1.1) to describe protein’s potential surface. As evident from Figure 1.1, many of the transient states are gateways to the folding and aggregation regions of the protein’s conformational energy landscape [13-15]. Therefore, knowledge of conformational fluctuations may represent a promising therapeutic strategy in designing drug molecules to prevent protein misfolding and/or aggregation [16, 17].

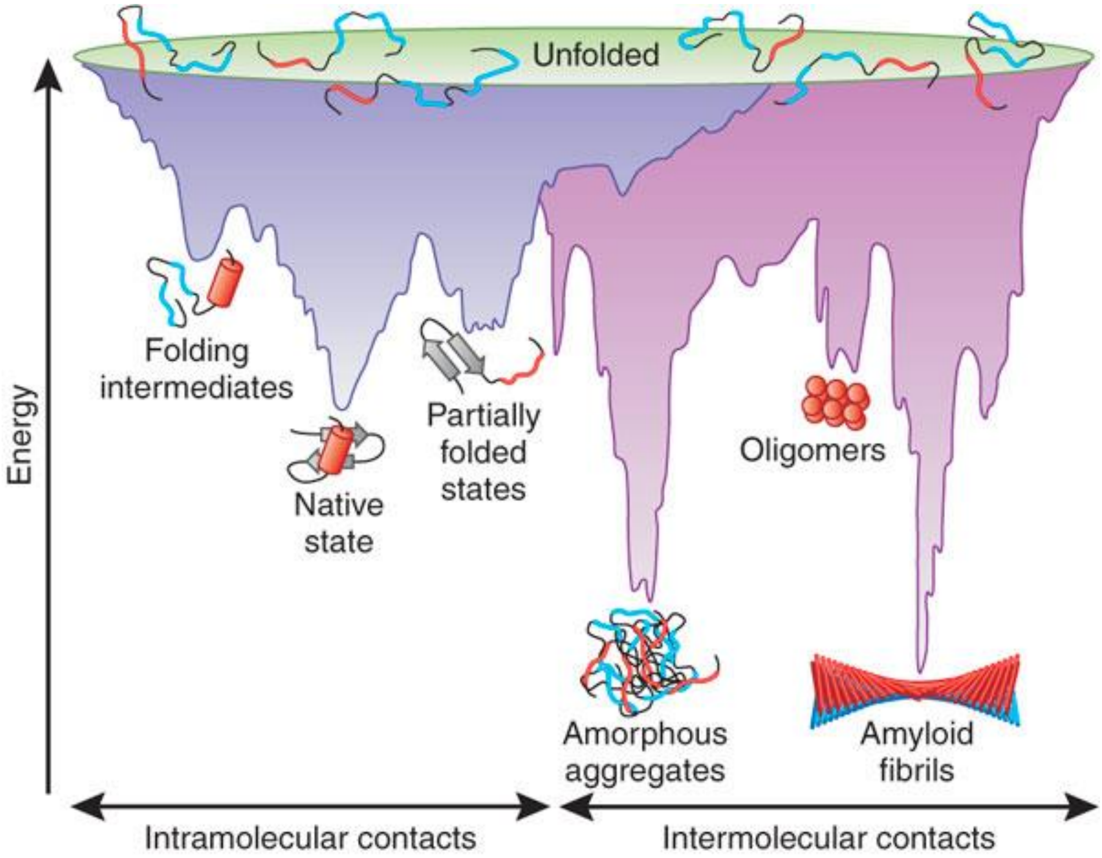

**Figure 1.1.** The ‘energy landscape’ of proteins. The purple surface shows the multitude of conformations 'funneling' to the native state via intramolecular contacts and the pink area shows the conformations moving toward amorphous aggregates or amyloid fibrils via intermolecular contacts. Both parts of the energy surface overlap. Aggregate formation can occur from intermediates populated during *de novo* folding or by destabilization of the native state into partially folded states and is normally prevented by molecular chaperones. Cell-toxic oligomers may occur as off-pathway intermediates of amyloid fibril formation. This figure is adapted from reference [18].

## 1.2 Allostery in Proteins

Allostery is a biological phenomenon of fundamental importance to many biological processes, including but not limited to cell signaling and the regulation of metabolism [19]. Allostery is the process where very subtle changes in structure at one location of a protein can be transferred to one or more distinctly distant sites, causing a change in biological reactivity. Allosteric interactions are often triggered by small changes at or around the active site of a protein *via* disruption of ionic linkages at specific contact points. One of the most famous example of allostery is oxygen binding in hemoglobin [1]. When the first oxygen molecule binds to one of the subunits of haemoglobin, a message is communicated to the other subunit *via* subtle conformational (structural) changes. This concept extends the possibility of using small molecule ligands, often known as 'effectors', to a protein at one site to induce conformational changes that will affect the subsequent binding of a second ligand at another site. Allosteric changes in conformation induced by ligand binding can also give rise to either reduction (allosteric inhibition) or enhancement (allosteric activation) of activity, depending on the particular system. Each enzyme molecule has only a limited number of active sites, usually no more than one per subunit which accounts for substrate saturation effect in enzyme kinetics. In addition to the active sites, allosteric enzymes have effector specific binding sites known as regulatory sites which are physically distinct from its active site. Effector molecules act by reversible, noncovalent binding to regulatory sites while allosteric ligand binding can be either reversible or irreversible.

Allosteric enzymes are substantially larger than non-regulatory enzymes which behave differently upon binding to any specific effector. Allosteric regulation can be 'homotropic' where the allosteric modulator is a substrate for its target enzyme, as well as a regulatory molecule of the enzyme's activity. Most often, a homotropic modulator is an activator of the enzyme. When the substrate and the effector are different species, the observed allosteric regulation is heterotropic. A heterotropic allosteric modulator may be either an activator or an inhibitor of the enzyme. For example, $O_2$ is a homotropic allosteric modulator of heamoglobin as binding of one $O_2$ enhances the probability of second $O_2$ binding while $H^+$, $CO_2$, and 2,3-bisphosphoglycerate are heterotropic allosteric modulators of heamoglobin. Furthermore, some allosteric proteins are capable of demonstrating both homotropic and heterotropic interactions as they can be regulated by both their substrates and other molecules.

Since allosteric regulation is highly selective, allosteric sites may represent a potential target for novel drug development. Allostery is an inherently dynamic phenomenon, since information must be transmitted from the allosteric site to the active site by subtle structural changes. In spite of individual successes in understanding the structural elements of allostery in well-investigated systems, much less success has been achieved in identifying a set of quantitative and transferable ground rules that provide an understanding of how allostery works in general. Towards this challenge, we have applied our novel device to study allosteric systems in TEM-1 beta lactamase which revealed some unprecedented correlation between allostery and functionally relevant natural mutations in TEM-1.

## 1.3 Mass Spectrometry

Mass spectrometry has become an indispensable analytical technique because of its supreme sensitivity, speed and diversity of application [20]. Over last two decades, continuous instrumental improvements have raised it to be the most widely used techniques in bio-analytical chemistry, including proteomics, metabolomics, high throughput drug discovery and metabolism, protein structure and dynamics etc.  It is routinely applied as the main analytical tool in forensic science, environmental science, food control, natural products or process monitoring, trace elemental analysis, health and beauty product development, and in many other industries [21] .Furthermore, its unprecedented capability to yield analytical information makes it also suitable for studying fundamental processes such as ion-molecule reactions, reaction kinetics, inorganic chemical reaction and mechanisms, atomic physics, geochronology and determination of thermodynamic parameters ( $\Delta G^{o}_{f}$, $K_a$, etc.), and many others [21-23].

**1.3.1 Principles.** The basic principle of mass spectrometry (MS) is to generate charged ions from desired analyte by a variety of techniques, separate theses ions according to their mass-to-charge ratio (*m/z*) and then detect them qualitatively and/or quantitatively. Moreover, there are some instruments that are capable of separating ions based on the size and shape in addition to their *m/z*. A mass spectrometer consists of three major components: the ion source, the mass analyzer and the detector which operates under high vacuum conditions. All modern MS instruments are completely computer controlled including data acquisition and data processing and even instrument calibration. A mass spectrum is the two dimensional representation of signal intensity or ion counts versus *m/z* where peak intensity directly reflects the abundance of the ions registered in the detector.  Figure 1.2 shows a general scheme of a mass spectrometer.

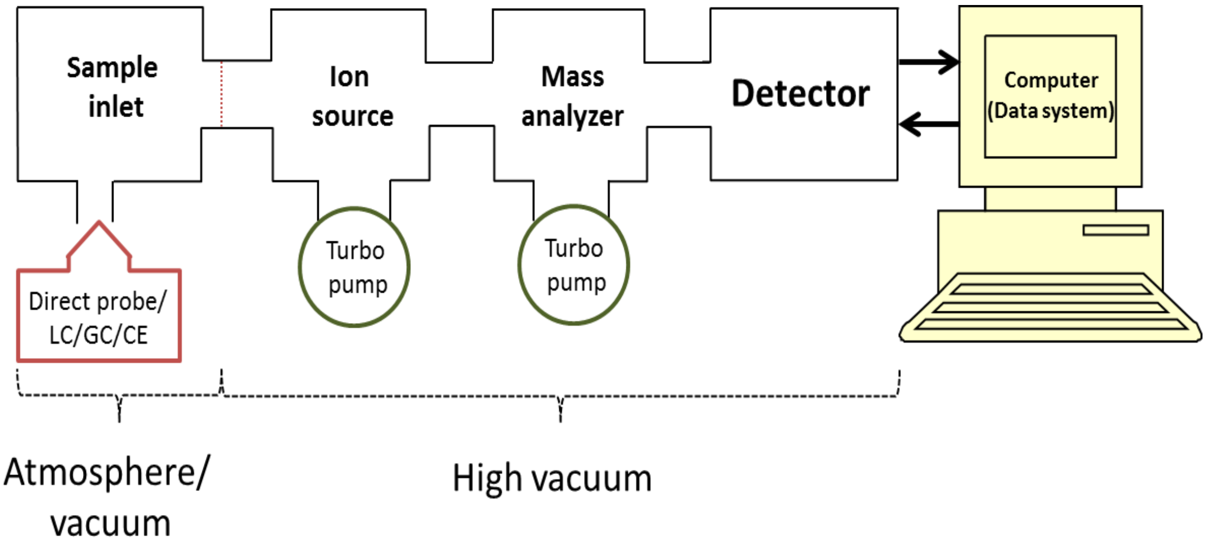

**Figure 1.2.** A general scheme of a typical mass spectrometer. Several types of sample inlets can be interfaced to ion source which can be either commercially available source or custom made. Highly efficient turbo pumps enable the transfer of charged ions into the mass analyzer to separate them. A 'back end' detector senses these ions and signals are processed by computer controlled data system.

**1.3.2 Ionization Techniques.** The choice of ion generation is dependent on the nature of analyte and most crucial for the desired application. The number of currently available ionization techniques is quite large and new ion generation methods are continuously being developed. The classical procedure of gas phase ionization such as electron ionization (EI), chemical ionization (CI), field ionization (FI) etc. are very energetic and cause extensive fragmentation, thus their use is limited to volatile or thermally stable compounds. Some ion sources like inductive coupled plasma or glow discharge are suitable for isotopic ratio measurements as they provide extremely accurate quantitative data. However, large fragile analytes like proteins or noncovalently bound complexes are only amenable to soft ionization techniques like electrospray ionization (ESI), desorption electrospray ionization (DESI) and matrix-assisted laser desorption ionization (MALDI). All of these ionization approaches can be implemented under atmospheric pressure while maintaining the structural integrity of the analyte. Additionally, singly or multiply charged ions are produced from analytes depending on the condition and ionization technique used. Since ESI is considered one of the most compatible techniques for studying intact proteins, it was selected for current studies to transfer proteins and other analytes into the gas phase.

**1.3.2.1 Electrospray Ionization.** Electrospray ionization (ESI) is a gentle ionization technique that was first introduced by Dole and coworkers in 1968 [24]. In 1984, Yamashita and Fenn successfully coupled ESI to MS to ionize intact proteins directly from solution to the gas phase environment of mass spectrometers [25, 26]. Soon after, ESI was adopted as the preferred ionization technique for large, non-volatile biomolecules, starting a new era of MS-enabled chemical and biological studies. Fenn and Tanaka (who developed MALDI) were awarded Nobel Prize in 2002 for their transformational contribution to MS-based science. In ESI, sample is dissolved in an appropriate volatile solvent and transported through a capillary placed at high positive or negative potential. The ions are generated by applying a potential difference of 2-6 kV between this needle and a counter-electrode that are separated by 0.3 – 2 cm [21]. The electric field causes charge accumulation on the surface of solvent at the tip of the capillary which then form a cone shaped liquid jet, known as Taylor cone. Eventually the charge repulsion breaks the Taylor cone into a highly charged spray of droplets (Figure 1.3).

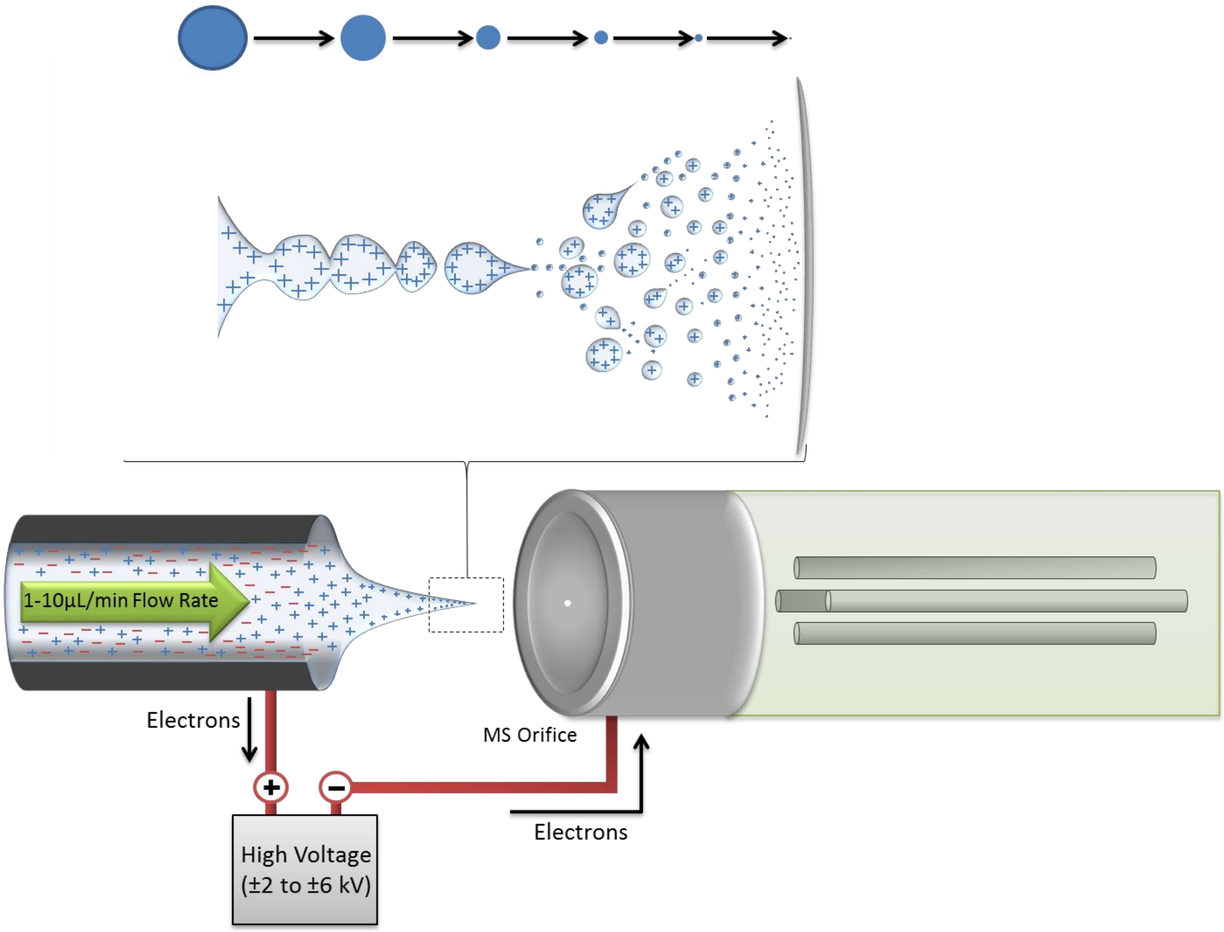

**Figure 1.3.** Schematic depiction of an ESI source operated at positive ion mode, adapted from reference [27]. Shown to the left is a thin metal capillary containing analyte solution where high electric field potential cause the formation of a Taylor cone. In a positive ion mode, positively charged particles congregate at the tip of the Taylor cone, resulting in the ejection of positively charged parent droplets at the liquid-air interface, while negatively charged particles align to the outer walls of the capillary (the opposite occurs for negative ion mode).

These droplets are then ejected from the Taylor cone and shrink through evaporation, most often assisted by a coaxial flow of inert nitrogen known as the nebulizer gas. During this evaporation process, all the charges begin to concentrate on the droplet surface. Eventually Coulombic repulsion overcomes the surface tension resulting in the release of numerous solvent-stripped charged ions at atmospheric pressure. These ions are then attracted by the oppositely charged curtain plate and pass through a small aperture into an intermediate vacuum region. An electric field focuses these ions to travel through a small orifice transferring them into the high vacuum zone of mass analyzer.

Though ESI is a widely used ionization technique, its exact mechanism of ion formation is still not well understood and there are many theories proposed to explain the mechanisms of multiple charged ion formation. A classical model of ESI, the Charged Residue model (CRM), was introduced by Dole in 1968. It assumes complete desolvation process is achieved *via* successive loss of all solvent molecules and leaving a 'charge residue' on the molecules [24]. A later theory, the Ion Evaporation model (IEM) proposed by Iribarne and Thompson, describes the formation of desolvated ions through direct field assisted evaporation from the surface of highly charged microdroplets [28, 29]. Recently Konermann proposed another model known as Chain Ejection model (CEM) that describes the production of a multiply charged stretched out ion by long chain polymers or biomolecules like protein, more particularly for unfolded protein [30]. In summary, IEM describes generation of smaller ion while CRM and CEM holds valid for large molecule release mechanism. These three ion release mechanisms are compared on Figure 1.4.

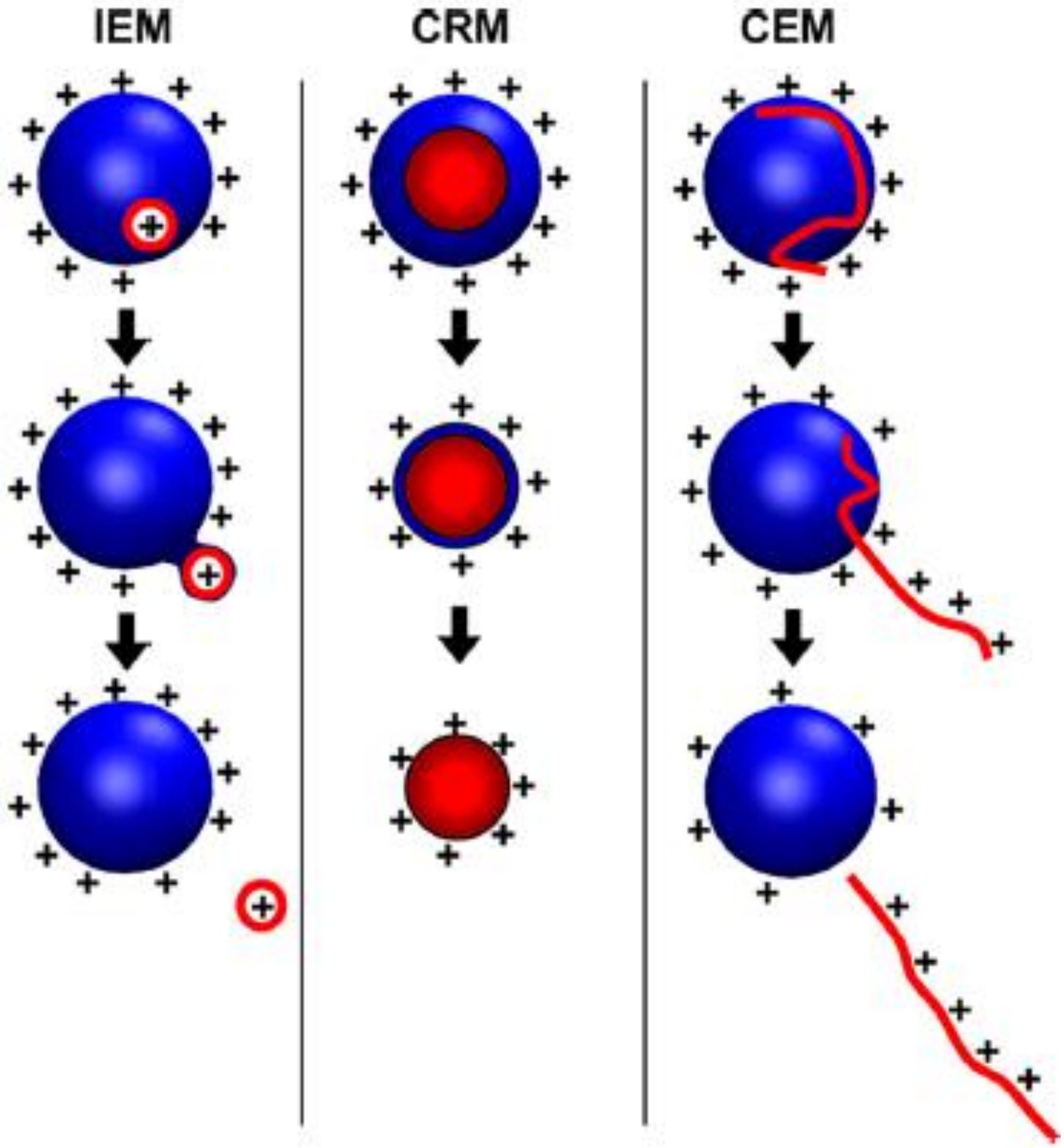

**Figure 1.4.** Summary of different ESI mechanisms. (a) IEM: Small ion ejection from a charged nano droplet. (B) CRM: Release of a globular protein into the gas phase. (C) CEM: Ejection of an unfolded protein. This figure is adapted from reference [30].

**1.3.3 Mass Analyzers.** A mass analyzer is the component of the MS that separates charged species according to their mass-to-charge ratio (*m/z*) and outputs them to the detector where they are detected as digital signals. Currently there are several types of mass analyzers available commercially such as quadrupole mass filter (Q), time-of-flight (TOF), magnetic sector (B), quadrupole ion trap (QIT ), Linear quadrupole ion trap (LTQ), Fourier transform orbitrap (FT-OT), Fourier transform ion cyclotron resonance (FTICR), accelerator mass spectrometry (AMS) [31]. All of these instruments use static or dynamic electric and magnetic fields, sometimes alone or in combination. However, the basic differences between different types of analyzer are in the manner in which they utilize electric or magnetic fields to achieve separation. Each mass analyzer has its advantages and limitations that should be considered before selecting it for a particular application. The performance of a mass analyzer is typically considered in terms of certain features: resolution and mass accuracy, mass range, possibility of tandem measurement, precision of isotopic pattern, analysis speed etc. This dissertation work was carried out on a hybrid instrument Qq-TOF (QStar Elite) form AB SCIEX, Concord, ON.

**1.3.3.1 Quadrupole time-of-flight (Qq-TOF).** The quadrupole time-of-flight (Qq-TOF) is a high performance hybrid mass spectrometer specially designed for protein identification and characterization using two quadrupoles (Q1 and Q2) to select and/or transmit ions to the TOF region for detection (Figure 1.5 a**).** Additionally it has another quadrupole (Q0) before the functional analyzer (Q1) for ion focusing and collisional cooling that ensures maximum ion transmission. The quadrupole analyzers use the trajectories in oscillating electric fields to separate ions according to their *m/z* ratio. The first mass analyzer is a linear quadrupole (Q) that employs a combination of direct current (DC) and radio frequency (RF) potential whereas the second one is a RF –only quadrupole (q).

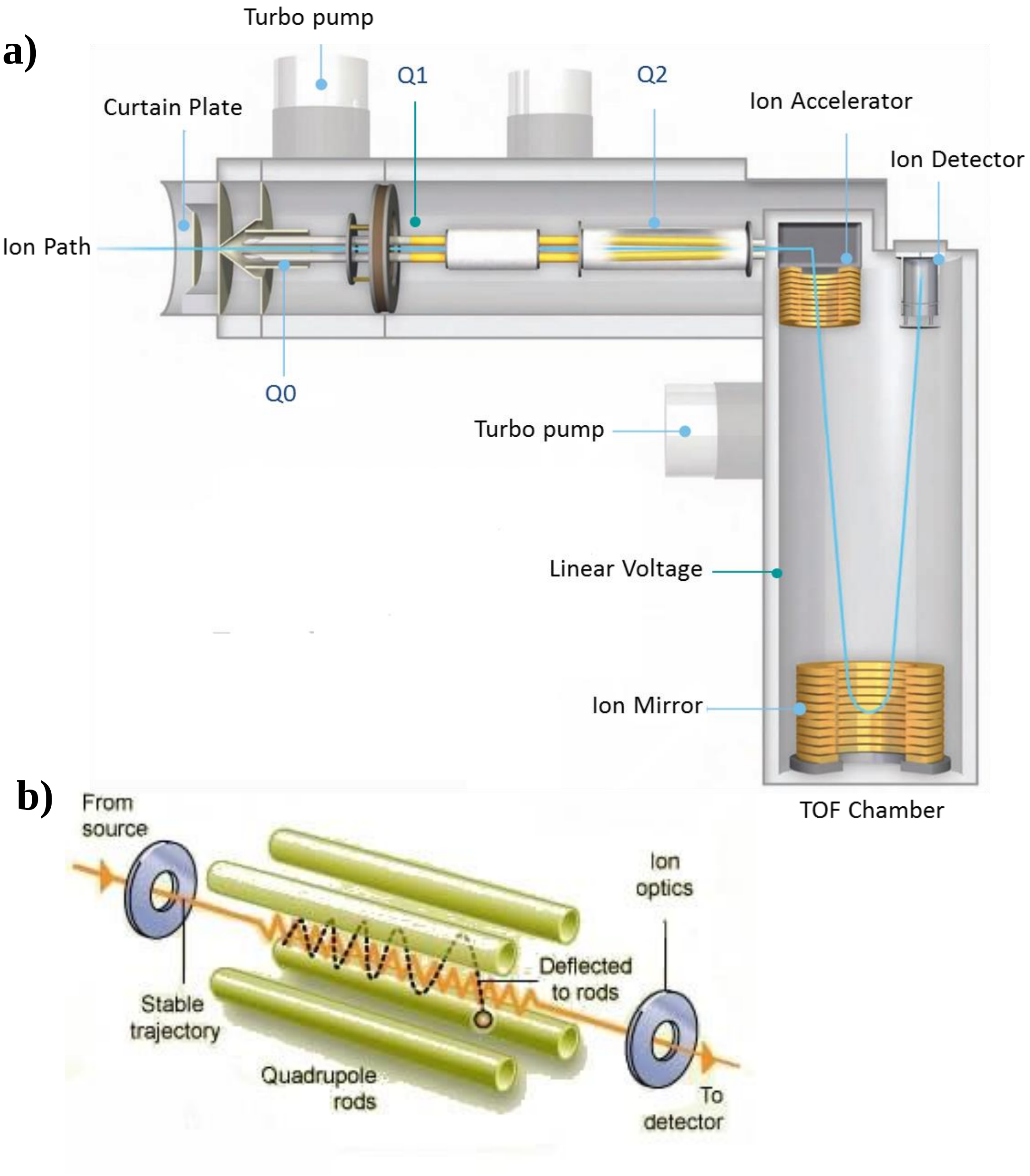

**Figure 1.5.** a) Ion path chamber detail in the QStar Elite system. b) Arrangement of four parallel cylindrically shaped rods of Quadrupole analyzer. The figures are adapted from user manual of Qstar Elite.

Quadrupole analyzers are made up of four parallel cylindrically shaped rod electrodes [32, 33]. These rods are arranged symmetrically in space extending in the *z*-direction and mounted in a square configuration (Figure 1.5 b). Opposite rods are connected in pairs where electrical potential is applied that comprise both DC and RF component. At any given time, potential experienced by both pairs of rods have same magnitude but opposite sign. A positive ion entering the quadrupole assembly in the *z*-direction will be drawn towards a negative rod. The magnitude and signs of potential applied on the rods are periodic ensuing an alternating attraction and repulsion in *x*- and *y*- direction in time. Ions of a specific mass have certain oscillation amplitude. Therefore, for any given values of DC and RF potentials, only a certain *m/z* range ions experience proper potential to have a stable trajectory. These ions travel in *z*-direction and finally reach the detector while ions that do not have the right *m/z* potential range will collide with the rods and discharge. Therefore, *m/z* range scanning is dependent on the ratio of DC and RF voltages. A mass spectrum is acquired by utilizing the first Q for mass scanning. The second quadrupole (q) of Qq-TOF is operated in the RF- only mode where a wide *m/z* range is allowed to pass through the system. Additionally, it can perform as a collision cell: neutral gas can be introduced to this region allowing fragmentation of desired ions that can be separated by the TOF analyzer on downstream.

A time-of-flight (TOF) analyzer separates ions by time where separation is based on the kinetic energy and velocity of the ions [34]. Ions of different *m/z* are allowed to drift through a field free region under very high vacuum. All the ions entering the accelerating region of TOF at any given time ideally have same kinetic energy but different velocity depending on their mass. During their flight along a known path, the lighter ions will go reach the detector faster than the heavier ones, thus arrival times can be converted into a mass spectrum. The TOF of the Q-star

Elite compensates any kinetic energy distribution by an electrostatic mirror that lies at a higher potential than the acceleration potential. This reflector allows the faster ions to penetrate deeper into the electric field than the slower ones which increases the flight path of the ions with slightly faster initial velocity. The micro channel plate (MCP) detector outputs the signal *via* time-to-digital converters (TDC) which is then processed by computer.

## 1.4 Mass Spectrometry Based Techniques for Studying Protein Conformations and Dynamics.

Understanding protein structures and their dynamics at high resolution is of great interest to resolve many biological mysteries. Nuclear magnetic resonance (NMR) and X-ray crystallography are two main tools of structural biology that enable complete 3D protein structural analysis. However, proteins are inherently dynamic and their dynamics is often related to their biological functions: protein-protein interactions, ligand binding, complex formation or structural effects of post translational modifications are strongly modulated by conformational perturbations. Unfortunately, experimental probing of many of these conformation changes is beyond the range of classical structural biology approaches using NMR and X-ray. X-ray is unable to provide dynamic views of low energy state conformations in real time scale and the data acquisition time in NMR is longer than the time scale at which the structural changes occur in biological processes. Additionally, both of these techniques have some significant limitations to determine the structures and dynamics of proteins or/and their complexes including size (upto 50 kDa), crystallizability, diffraction quality of crystals, solubility and amounts of sample required. On the other hand, in recent years other techniques like electron microscopy (EM) or tomography techniques have substantially improved to perform at low temperature making them more appropriate for monitoring whole cells or extremely large complexes. This leaves a ‘size gap’ in the range of proteins or protein complexes 50-200 kDa [35]. Structural mass spectrometry (MS) has been emerged as a tool that can fill this technological gap.

The usage of MS in structural studies has dramatically increased with the technological advances in terms of its ability to provide highly resolved structural information. The three main techniques of structural MS include Hydrogen-deuterium exchange (HDX), covalent labeling strategies (mainly hydroxyl radical) and chemical cross linking [22]. In the present work, ESI-MS HDX approach was used on a microfluidic platform, facilitating site specific conformational studies on several proteins and their complexes.

**1.4.1 Hydrogen-Deuterium Exchange (HDX) Mass Spectrometry.** Hydrogen-deuterium exchange (HDX) is a powerful and commonly-used technique in both NMR and MS based protein structure and dynamics studies. In the early 1990s, HDX was combined with MS, inspired by related NMR methods. Combining the information from classical approaches with HDX data, a thorough understanding of protein functions can be achieved [36-38]. HDX is a sensitive probe for solvent accessibility and detecting the presence or absence of hydrogen bonding or other sequestration of labile hydrogen atoms from solvent within the protein in solution [39, 40]. However, HDX is mostly dependent on the H- bonding present in any protein.

The amide protons of protein backbone are exchangeable with the deuterium atoms from the solvent surrounding the protein at different measurable exchange rates. The amide protons that are more solvent accessible or lack strong hydrogen bonding will undergo exchange faster than that are buried participating in hydrogen bonds [38, 41]. The mass increase due to more deuterium incorporation instead of hydrogen is monitored *via* mass spectrometry. The rate at which deuterium is taken up reflects protein’s structural stability and solvent accessibility.

**1.4.1.1 Hydrogen-Deuterium Exchange (HDX) Mechanism.** Hydrogen-deuterium exchange (HDX) reactions can progress *via* three different mechanisms: base-catalyzed exchanged and two different acid-catalyzed exchanges [42]. However, the based-catalyzed mechanism (Figure 1.6) is more relevant to biological process and used for current dissertation work.

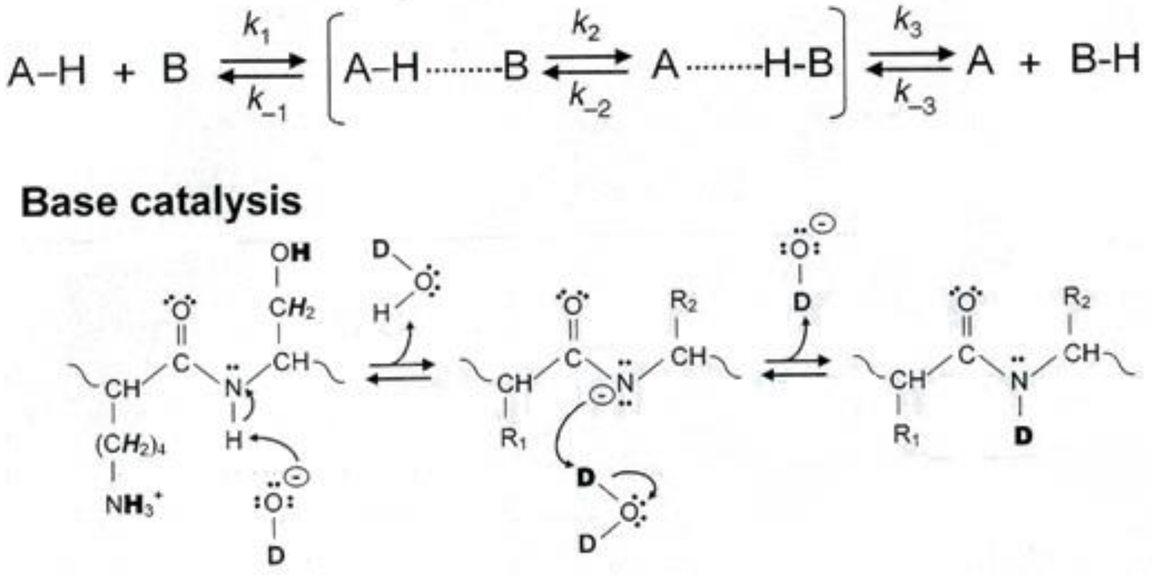

**Figure 1.6.** Based-catalyzed hydrogen-deuterium exchange (HDX) mechanisms of amide protons in peptides or proteins.

The rate of backbone amide hydrogen the exchange is a function of pH which usually plays a vital role in controlling reaction time in HDX-MS based techniques. Figure 1.7 shows the pH dependence of several types of labile hydrogens that are common in protein or peptide. Most of the backbone amides have a lower $pH_{min}$ values compared to the side chain protons [43].

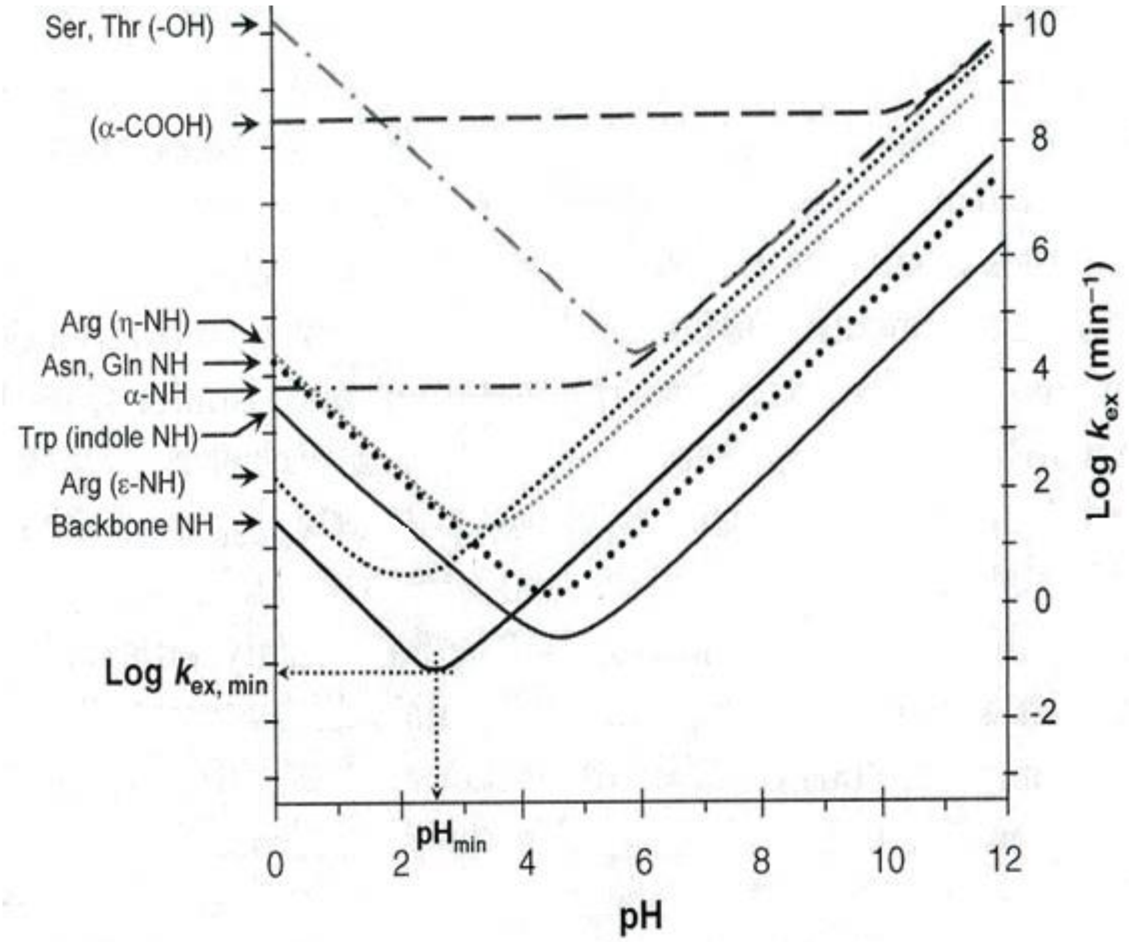

**Figure 1.7.** Hydrogen-deuterium exchange (HDX) mechanism is a function of pH of amide protons in peptides or proteins. This figure is adapted from a book [22].

In HDX experiments, the pH is often adjusted to 2.5 after labeling to quench the backbone amide exchange while most of the side chains continue exchanging resulting in a loss of label. Therefore, the observed HDX profile is essentially a contribution of only the backbone amides on an entire peptide or protein except proline (which has no backbone amide) and the first reside on a peptide (corresponding to the free N-terminus). Additionally, HDX is also influenced by certain other factors such as, temperature, solvent, pressure, adjacent side chains and ionic strength.

The hydrogen/deuterium exchange rate of an unstructured protein is called the ‘intrinsic’ rate ($k_{\text{int}}$) which is expressed as the sum of acid, base and water mediated catalyzed contributions at a certain pH (Equation 1.1) [43, 44].

$$k_{\text{int}} = k_{\text{acid}}\,[\mathrm{H_3O^+}] + k_{\text{base}}\,[\mathrm{OH^-}] + k_{\text{water}} \tag{1.1}$$

Based on a simple two state kinetic model, Englander *et.al* related observed HDX kinetics of backbone amide to thermodynamics by the following formulas.

$$\text{Closed} \underset{k_{\text{cl}}}{\overset{k_{\text{op}}}{\rightleftarrows}} \text{open} \xrightarrow{k_{\text{int}}} \text{exchanged} \tag{1.2}$$

$$k_{\text{ex}} = k_{\text{op}} \times k_{\text{int}} \,/\, (k_{\text{cl}} + k_{\text{int}})$$

Where $k_{op}$ and $k_{cl}$ are the rates at which the amide hydrogen converts from closed state to open state and vice versa [45]. When HDX is faster than the rate of closing ($k_{int} >> k_{cl}$) it follows a EX1 mechanism. On the other hand, for most proteins at or under neutral pH, $k_{cl} >> k_{int}$ and HDX is mediated via EX2 mechanism and equation 1.2 is simplified as below [46]. A detail of this equation is also discussed in Data Analysis Method section of Chapter 3.

$$\begin{aligned} k_{ex} &= k_{op} \text{ x } k_{int} / k_{cl} \\ &= K_{op} \text{ x } k_{int} \end{aligned} \tag{1.3}$$

The closing equilibrium constant can be related to a term ‘protection factor (PF)’ given by,

$$\mathrm{PF} = k_{int} \;/\; k_{ex} \tag{1.4}$$

The protection factor reflects the physical environment of an amide that is correlated with the thermodynamic stability of the closed state [47]. Thus PF is an important parameter to estimate the conformational flexibility that can serve as thermodynamic sensor of local structural stability in any protein. This topic will be discussed in details in the data analysis section of Chapter 3.

**1.4.1.2 Deuterium Incorporation into Protein.** Deuterium incorporation into protein can be done following two different strategies: pulse labeling and continuous labelling. Figure 1.8 summarizes both approaches. Continuous labeling is performed by monitoring deuterium exchange rate at various incubation times under conditions where native conformation of protein is stable. Therefore, approach provides information about conformational dynamics of native protein [20, 48, 49]. Complementary to this approach, pulse labeling involves labeling with deuterium for a very short time after the protein is forced to undergo structural changes where the incubation period with perturbing reagent is varied [50, 51]. The observed HDX profile is a snap shot of protein structure that exited at the time of pulse and provides information of the kinetics of the structural perturbation process.

**1.4.1.3 Measuring HDX with MS: Global Versus Local Exchange.** HDX experiments can be designed in two different manners depending on the goal of the studies. Deuterium uptake on the whole protein can be monitored to estimate the overall exchange behaviour which is known as Global exchange approach. For site specific studies, proteins can be fragmented into smaller peptides to locate the local environment. Proteolytic digestion is relatively more versatile and popular approach (known as 'bottom-up' approach) which is usually followed by LC separation before mass analysis [52]. Alternatively, post ionization gas phase 'non-ergodic" fragmentation techniques like electron capture dissociation (ECD) or electron transfer dissociation (ETD) can provide near single residue resolved information but their usage is limited to the size of the protein (known as 'top-down' approach) [53-56].

Site specific measurement of deuterium incorporation can be achieved by fragmentation of the intact protein either before ionization or post ionization gas phase fragmentation techniques. In either case the exchange reaction is quenched by lowering the pH at 2.5 prior to fragmentation to minimize the back exchange probability [57, 58]. Digestion of labeled protein can only be carried out using acid proteases typically with pepsin (usually porcine) that showed the best performance for digestion under quench conditions [41, 57, 59]. To the date, two other acid proteases have been used either alone or in combination with pepsin: the type XII protease from *Aspergillus saitoi* and type XVIIIfrom *Rhizopus* sp., both of them are less efficient than pepsin [60].

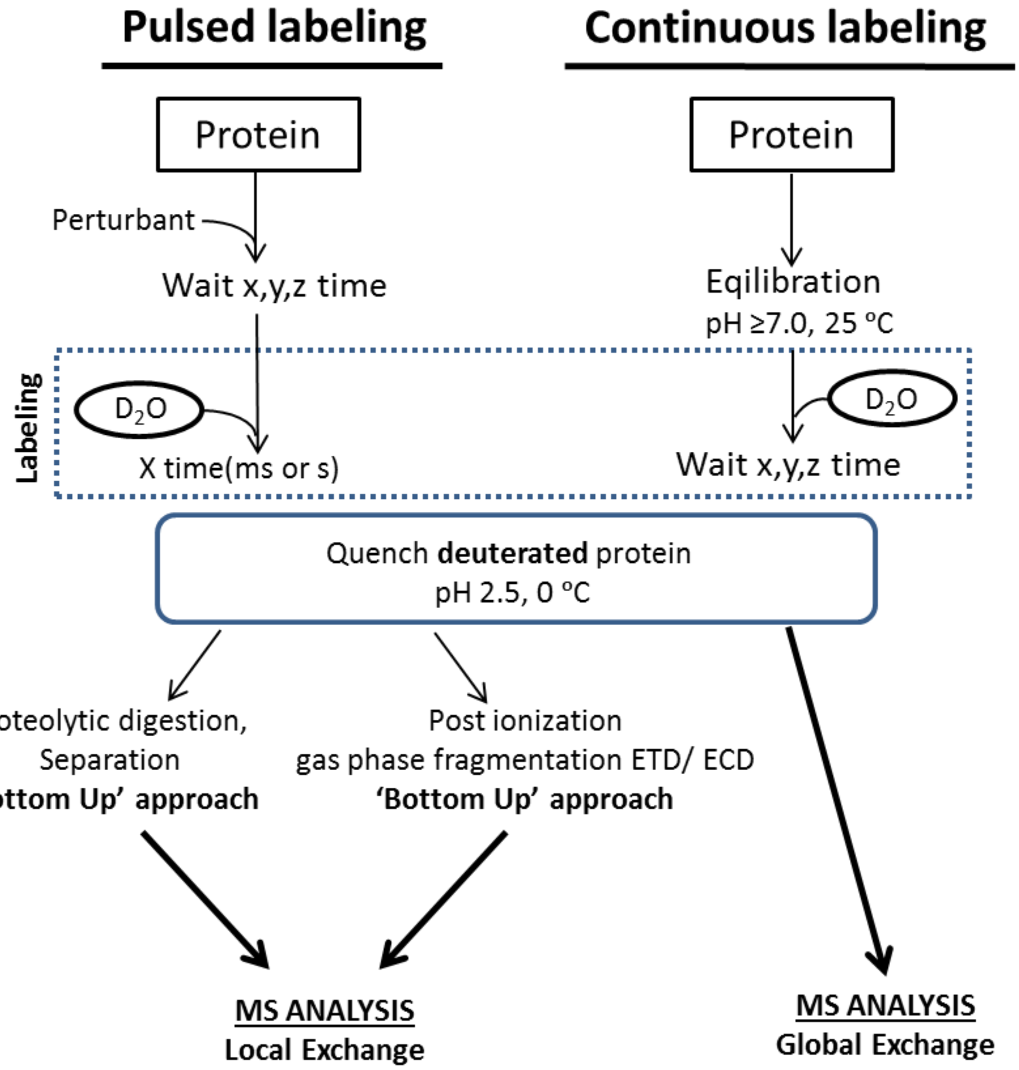

**Figure 1.8.** General work flow scheme for HDX-MS experiments.

**1.4.1.4. HDX with Time Resolved Electrospray Ionization (TRESI).** Time-Resolved Electrospray Ionization mass spectrometry (TRESI-MS) has been established as an extraordinarily enabling technology in the study of conformational changes occurring on the millisecond (ms) timescale during biological activity. TRESI-MS allows for the simultaneous detection of virtually all reactive species undergoing a reaction process which is almost always inaccessible *via* conventional optical based analytical techniques. The development of ESI MS enabled continuous-flow rapid mixing tool by Wilson and Konermann, made a breakthrough in time – resolved (TR) experimental techniques [61]. Their TR apparatus (Figure.1.9) is essentially a concentric capillary mixer with adjustable reaction chamber volume that can be used as an alternative ESI source. Reactant solutions are continuously introduced to the mixer from both syringes while they are only allowed to mix in a narrow region towards the outlet of the device. This approach facilitates efficient diffusive mixing of reagents which initiates the reaction of interest. The reaction time can be controlled by changing the position of the mixer within the outer capillary or/and changing the flow rates. The reaction time associated with mixing is known as the 'dead time' and largely determines the earliest time point accessible by the apparatus. The approximate reaction time can be calculated based on the total flow rate and reaction volume (Equation 1.5).

$$t = V_r / v_t + V_m / v_t \tag{1.5}$$

where,

$t$ = reaction time
$v_t$ = total solution flow rate
$V_r$ = volume of the reaction chamber
$V_m$ = volume of the mixing region

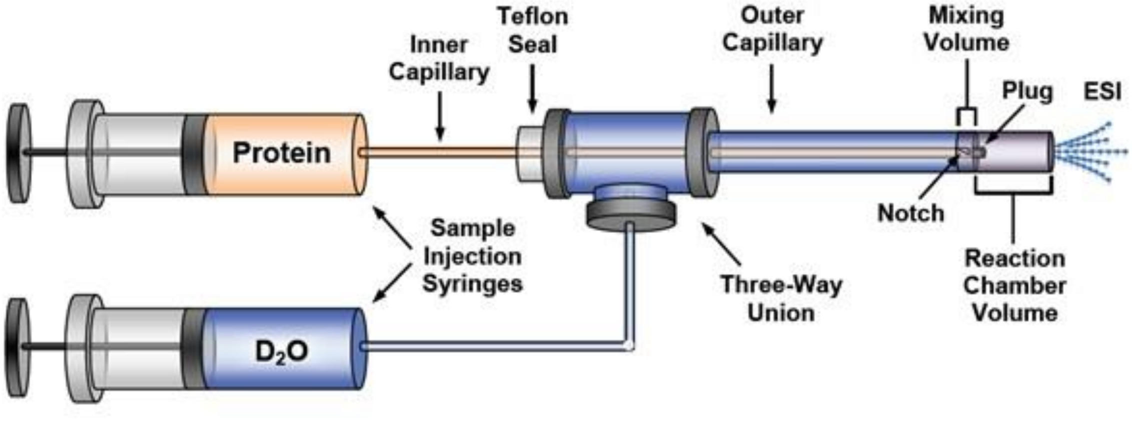

**Figure 1.9**. Schematic depiction of a Capillary-based rapid mixer with adjustable reaction chamber volume for TRESI-MS. An inner fused silica capillary is inserted through an outer metal capillary of larger diameter through a three-way union. Two different solutions, one containing the protein and the second a deuterium donor, are supplied at the inlets of the capillaries by automated Hamilton syringes at rates maintaining laminar flow throughout the apparatus. A small notch, about 2 mm away from the plugged end of the inner capillary, enables the solution from the inner capillary to escape and mix rapidly with the solution in the outer capillary in the inter-capillary space. The region between the notch and the outlet of the apparatus at the end of the outer capillary represents the reaction chamber volume. The outer capillary is used as an ESI source. This figure is adapted from a reference [62].

TRESI-MS has contributed substantially to the characterization of short-lived intermediates involved in millisecond time-scale (bio)chemical processes. The aim of this research was to integrate more multistep MS- based experimental approaches (such as HDX, proteolysis) with TRESI in order to facilitate more detailed structural analysis of conformational intermediates. This dissertation represents the successful integration of TRESI with ‘bottom up’ HDX approach on a microfluidic platform enabling the characterization of dynamic regions in native proteins and proteins undergoing conformational changes during biological activity which has been discussed in Chapter 3, 4, 5 and 6.

## 1.5 MICROFLUIDICS

Microfluidics (MF) is the science and technology of precise manipulation of fluids in networks of micro channels that can transport typically microliters to femtoliters volumes of fluid [63, 64]. This miniaturization technique has worked its way in many applications since it was first introduced in the beginning of the 1980s. Development of gas chromatography at Stanford by S.C. Terry in 1979 is a milestone in the history of MF. Soon after that, researchers at IBM developed ink jet printer nozzles less than 100 µm in diameter which is probably the most mature MF microfluidic technology that is prevailing in ink-jet printing industry for last 20 years [65-67].

Microfluidic systems offer distinctive properties such as

- Aqueous flow is generally laminar, not turbulent.
- Diffusion is an efficient process for mixing the dissolved contents of two or more fluids.
- Particles can be separated based on their size (by diffusion).
- Compared with other analytical devices, microfluidic devices allows rapid reaction and analysis times [68].
- Only small volumes of samples and reagents are required facilitating efficient heat and mass transfer.

- Allows the parallelization and integration of multiple sample processing approaches.
- Produces little waste which is very important in working with biologically hazardous material [69].
- Facilitates the measurement of the reproducibility of biochemical (or more importantly, cell biological) experiments which involves a large number of parallel run experiments [70].

Beyond that, microfluidic system offer several new advantages to carry out specialized types of biochemical synthesis. In contrast to traditional isolated application specific approaches, MF provides a set of fluidic unit operations which can be designed for automated multiple application chemical, biochemical or medical process. High throughput microfluidic systems have been applied as a powerful tool in different stages of variety of fields, including analytical chemistry, genomics, proteomics, drug discovery and delivery, diagnostics, combinatorial synthesis, single cell analysis, protein separation, crystallization, biosensing, and for a variety of laboratory automation applications in the pharmaceutical and healthcare industries [70, 71]. The scope of the applications of MF boundless as it offers fundamentally new capabilities for controlling concentrations of molecules in space and time [72]. The most important functionalities are sample preparation, mixing, transportation, separation and biosensing detection. The terms ‘lab on a chip’ (LOC) and Micro Total Analysis System (μTAS) are synonyms for devices that takes advantages of micro flow and integrate a multiple sample handling functionalities on a small scale on a single platform [63, 73]. Many complex chemical and biological systems require multidimensional analysis for identification and quantification of individual components but cannot afford to waste sample at various sample handling steps.  LOC and μTAS support integration of a number of different surface geometries and chemistries to address this issue enabling direct analysis of many challenging and complex biological systems including whole cells, nucleic acids, proteins, enzymes.

### 1.5.1 Fabrication Techniques and Materials

The choice of appropriate material is important in application specific device development and should include considerations such as machinability and ease of fabrication, cost, process time, chemical compatibility, molecular adsorption, surface charge, optical properties. Glass, quartz, silicon, polymeric substrates like poly(dimethylsiloxane) (PDMS), poly(methyl methacrylate) (PMMA), polycarbonate, Teflon and many other elastomers or even metals like aluminum or copper have be used successfully to fabricate MF devices [74-78]. Conventional approaches in the fabrication of microfluidic devices includes photolithography, chemical etching, hot embossing, laser ablation, thin-film deposition, electroplating, thermal or chemical bonding and bond breaking or formation using UV, chemical degradation [79]. Many of these commonly used fabrication protocols are lengthy requiring days to week from design to completion [80]. This work presents a simple and fast fabrication technique that uses laser ablation to generate microchannels on PMMA.

**1.5.2 The Microfluidic Environment and Mixing Principles.** In microfluidics, the flow pattern is governed by channel geometry along with two important inherent properties of a fluid: surface tension and viscosity. When fluid passes through a micro channel, the molecules of the fluid in contact with the stationary solid surface tends to slow down due to the frictional resistance which is related to Reynolds number (Re). Conversely, the fluid at the center of the stream experiences higher velocity which generates a distribution of flow velocities within the microfluidic channel [81, 82].

**1.5.2.1 Reynolds Number (Re).** In fluid mechanics, the effect of viscosity on flow characteristics is interpreted in terms of Reynolds number (Re). Re is the ratio of inertia forces to viscous forces that quantifies the relative importance of these two types of forces for given flow conditions. Systems that operate at the same Reynolds number will have the same flow characteristics even if the fluid, speed and characteristic lengths vary. The general expression of the Reynolds number (Re) is

$$\boldsymbol{Re = VL\rho / \mu} \tag{1.6}$$

where,

$\boldsymbol{V}$ = average velocity of flow
$\boldsymbol{L}$ = a characteristic length
$\boldsymbol{\mu}$ = the viscosity of the fluid
$\boldsymbol{\rho}$ = density of the fluid

High values of the Re (on the order of 10 million) indicate that viscous forces are small and the flow is essentially having no boundary layers [83]. On the other hand, low values of the parameter (on the order of 1 hundred) indicate that viscous forces are dominating parameters influencing the fluid flow [83, 84]. The Reynolds number provides the criterion for Laminar and turbulent flows.

**1.5.2.2 Laminar Flow**. Flows of fluid can be classified into variety of categories with consideration of the flow characteristics with respect to time and the distance along the flow path. In 1883, Professor Osborne Reynolds of Manchester University classified fluid flow into two distinct types: Laminar and turbulent flow [85]. Laminar flow has a smooth appearance in which flow occurs in layers with one gliding over the other with little or no mixing. Most viscous fluids flow under laminar regime having a distinct boundary layer. On the other hand, turbulent flow is characterized by mixing of fluids by eddies of varying size within the flow. Any fluid flow may be laminar providing it occurs at a small enough velocity or around microscopic dimensions when the Re number drops to around 2000 [63, 85]. However the transition between laminar and turbulent flow occurs between Re of 2300 - 4000 and this transition can be modulated by changing the flow velocity. Under a critical value of Re ($Re \leq 2300$), fluids follow unidirectional but steady parallel paths where only molecular diffusion may generate fine spread out between two layers [86, 87]. The typical channel depth used for this work is under 200 μm where the Re value is around 1 [73, 83, 88]. Therefore the fluid flows under our experimental conditions will be laminar flow.

**1.5.2.3 Mixing in Microfluidic Devices.** Many of MF applications require mixing of two or more reagents which is often a challenging task under laminar flow condition. Diffusion can play a dominant role in microfluidic mixing while in macroscopic systems, mixing can be achieved through turbulent flow or vigorous stirring [89]. Reactions initiated in micro-sized systems that are strictly diffusion-limited occur significantly faster than they would at the larger scale. Mixing performance can be increased by increasing mixing time and contact surface so that the diffusion occurs efficiently. The diffusion time ($t_d$) increases proportionally with the diffusion length or diameter of the reactor but inversely with diffusion coefficient (D) which is shown in the following equation.

$$t_d = d^2 / D \tag{1.7}$$

Therefore, the diffusion coefficient (D) is a good approximation to evaluate the feasibility of diffusion limited mixing (as well as reaction) of multiple analytes in a micro channel that rely solely on diffusion. Diffusion is also strongly influenced by nonreacting species or solvent molecules that need to be under consideration as well (solvent shells can contribute to the apparent D). Since diffusion coefficient (D) is a measurement of how fast reagent molecules can move in a medium such as water, in a laminar flow system, molecules with a higher D value will travel faster into another layer and will ensure mixing of analytes [88]. Mixing of any large biomolecule with a small molecule under laminar condition is therefore has to rely on the diffusion of small molecules since the D values of biomolecules are usually very small (decrease with the increasing molecular size) [69, 90, 91]. Table 1.1 shows diffusion coefficients for small and large molecules in water [83].

**Table 1.1. Diffusion coefficients for small and large molecules in water at 25 ºC**

| Molecule | Molecular Weight /kg $mol^{-1}$ | $D/10^{-10}$ $m^2s^{-1}$ |
|---|---|---|
| Proton | 0.001 | ~50 |
| Water | 0.018 | 22.6 |
| Methanol | 0.032 | 15.8 |
| Ethanol | 0.046 | 12.4 |
| Sucrose | 0.342 | 5.216 |
| Ribonuclease | 13.7 | 1.19 |
| Urease | 480 | 0.346 |
| Myosin | 493 | 0.116 |
| Collagen | 345 | 0.069 |

All of the systems studied in this dissertation involve single or multiple mixing steps between protein molecules with aqueous acetic acid or deuterium oxide. Therefore, the mixing length and time was optimized experimentally to ensure complete diffusion of protons into protein layer. In most of the cases, internal standards were applied to adjust optimum diffusion length and flow rates. When it occurred, poor mixing performance was evident in the mass spectrum, appearing as complicated and non-Gaussian deuterium distributions.

**1.5.3 VersaLASER.** In This work, we use a 30 watt carbon dioxide ($CO_2$) laser for ablation of PMMA. Carbon dioxide ($CO_2$) lasers convert 20% of the input power into laser light which is highly efficient [92, 93]. Its operation can be initiated electronically under a variety of conditions, emitting a steady narrow beam at low gas pressure or pules at high pressure. Certain parameters such as mode, wavelength, type of laser operation (continuous wave or pulsed) and focal length are fixed for selected laser and beam delivery system while only the laser power is varied to obtain a desired laser energy level. The $CO_2$ laser has relatively low precision requirements but generates high power as it uses laser energy intensities between 20 $kW/cm^2$ and 60 $kW/cm^2$ [92]. The $CO_2$ laser is capable of generating an emission band between 9 and 11 μm in the infrared region which involves vibrational transitions of the $CO_2$ molecule. But the 10 μm output is generally used as it can be transmitted through atmosphere efficiently and is absorbed strongly by a wide range of materials making $CO_2$ lasers suitable for cutting, drilling and welding of metals and non-metals [93]. Presently the use of lasers is rapidly growing in modern industrial applications as new alternative to traditional manufacturing processes.

VersaLASER™ is a computer controlled $CO_2$ laser device assisted by drawing software (i.e. CorelDraw X3) that is capable of transforming images or drawings into engravings on variety of materials. Materials such as plastics, woods, fabrics, metals, glass and ceramic can be effectively processed with a short production time around minutes depending on the complexity of the design. The drawing generated on the graphic software is color coded where blue denotes for marking, red for cutting and black for deep engraving (raster). This laser system uses high quality digital motors with highly reliable and simple optical encoders to function as a printer at different laser power and mode. The laser can be focused manually based on material thickness, allowing precise control of channel width and depth which is extremely important for predicting the nature of the fluid flowing through this micro channels.

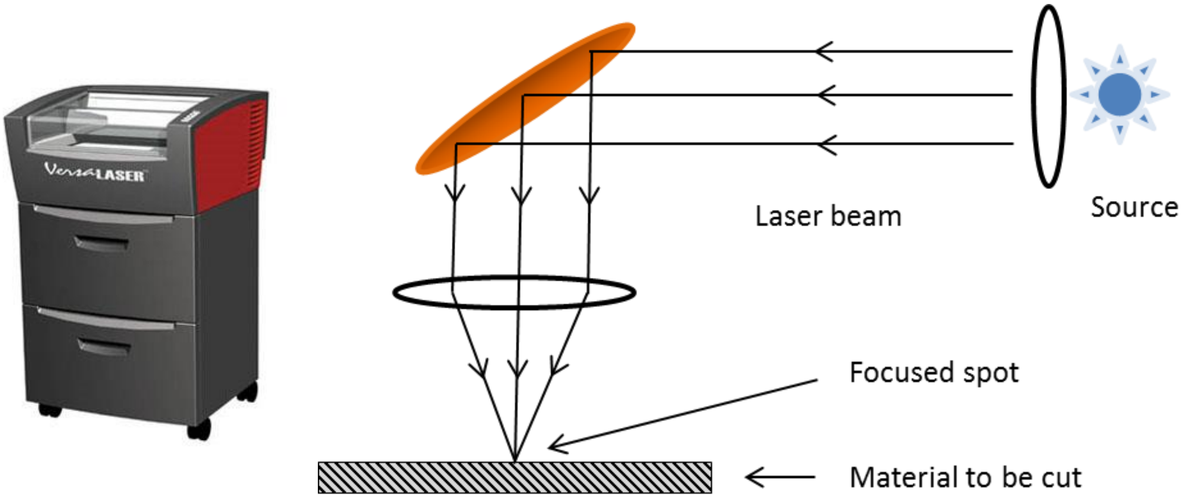

**Figure 1.10.** a) Universals VersaLASER™ b) a schematic representation of work process of versa laser.

**1.5.4 Poly(methyl methacrylate) PMMA.** Poly(methyl methacrylate) (PMMA) is a synthetic polymer of methyl methacrylate with the trade name Plexiglas® or acrylic glass. PMMA is a crystal clear thermoplastic material that can be used as an economical replacement of glass. The exceptional characteristics of PMMA are its optical clarity, low UV sensitivity, good mechanical stability, surface hardness and excellent resistance to aging and weather including UV radiation.

PMMA has good antiscratch properties and retains its gloss coating even after prolonged use; however it is susceptible to cracking under tensile stress. Despite of its superb environmental stability, PMMA demonstrates poor solvent resistance to many organic solvents on an account of its easily hydrolyzed ester groups. Therefore any scientific application that involves PMMA is limited to a narrow solvent choice [94]. PMMA swells and eventually dissolves in any inappropriate solvent which may interfere with reagents used in experiments and cause excessive background noise in mass spectra.

PMMA is often preferred in microfluidic device fabrication because of it is moderate properties, easy handling and low cost [80]. In recent years, $CO_2$ lasers have been used to for engraving micro channels on PMMA as it absorbs IR light in 2.8- 25 μm wavelength band which is compatible with $CO_2$ lasers [74, 95]. PMMA vaporizes to gaseous compounds including its monomers upon laser ablation ensuring very clean and fine channel formation. As PMMA is an organic polymer, release of its monomer vapour to environment upon laser cutting does not cause pollution. This ablation process is implemented not only in microfluidic device fabrication but also in visual communication food-contact applications and the medical sector.

PMMA is the most frequently used material in microfluidic research because of its other advantages in terms of faster design times, low cost, possibilities of obtaining flexibility deformable shapes and the ability to seamlessly impregnate nanoscale features [75, 95, 96]. In this work, PMMA was chosen as a substrate for MF device fabrication using laser ablation mainly because of its faster process time and low cost. The fabrication process is discussed in details in experimental section of Chapter 2.

# REFERENCES

1. David L. Nelson, M.M.C., *Lehninger's Principles of Biochemistry*. 2013: W.H.Freeman & Co Ltd.
2. Henzler-Wildman, K. and D. Kern, *Dynamic personalities of proteins.* Nature, 2007. **450**(7172): p. 964-972.
3. Pocker, Y. and S.B. Biswas, *Conformational Dynamics of Insulin in Solution - Circular Dichroic Studies.* Biochemistry, 1980. **19**(22): p. 5043-5049.
4. Van Nuland, N.A.J., et al., *Real-time NMR studies of protein folding.* Accounts Chem. Res., 1998. **31**(11): p. 773-780.
5. Miranker, A., et al., *Detection of Transient Protein-Folding Populations by Mass Spectrometry.* Science, 1993. **262**(5135): p. 896-900.
6. Carrell, R.W. and D.A. Lomas, *Conformational disease.* Lancet, 1997. **350**(9071): p. 134-138.
7. Bellotti, V. and F. Chiti, *Amyloidogenesis in its biological environment: challenging a fundamental issue in protein misfolding diseases.* Curr. Opin. Struct. Biol., 2008. **18**(6): p. 771-779.
8. Bucciantini, M., et al., *Inherent toxicity of aggregates implies a common mechanism for protein misfolding diseases.* Nature, 2002. **416**(6880): p. 507-511.
9. Calamai, M., et al., *Relative influence of hydrophobicity and net charge in the aggregation of two homologous proteins.* Biochemistry, 2003. **42**(51): p. 15078-15083.
10. Chiti, F., et al., *Studies of the aggregation of mutant proteins in vitro provide insights into the genetics of amyloid diseases.* P. Natl. Acad. Sci. USA, 2002. **99**: p. 16419-16426.
11. Chiti, F., et al., *Kinetic partitioning of protein folding and aggregation.* Nat. Struct. Biol., 2002. **9**(2): p. 137-143.
12. Calamai, M., F. Chiti, and C.M. Dobson, *Amyloid fibril formation can proceed from different conformations of a partially unfolded protein.* Biophys. J., 2005. **89**(6): p. 4201-4210.

13. Frauenfelder, H., S.G. Sligar, and P.G. Wolynes, *The Energy Landscapes and Motions of Proteins.* Science, 1991. **254**(5038): p. 1598-1603.

14. Dill, K.A. and H.S. Chan, *From Levinthal to pathways to funnels.* Nature Structural Biology, 1997. **4**(1): p. 10-19.

15. Hartl, F.U. and M. Hayer-Hartl, *Converging concepts of protein folding in vitro and in vivo.* Nat. Struct. Mol. Biol., 2009. **16**(6): p. 574-581.

16. Mandelkow, E.M. and E. Mandelkow, *Biochemistry and cell biology of tau protein in neurofibrillary degeneration.* Cold Spring Harb Perspect Med, 2012. **2**(7): p. a006247.

17. Keppel, T.R., B.A. Howard, and D.D. Weis, *Mapping Unstructured Regions and Synergistic Folding in Intrinsically Disordered Proteins with Amide H/D Exchange Mass Spectrometry.* Biochemistry, 2011. **50**(40): p. 8722-8732.

18. Hartl, F.U. and M. Hayer-Hartl, *Converging concepts of protein folding in vitro and in vivo.* Nat Struct Mol Biol, 2009. **16**(6): p. 574-581.

19. Zuiderwegy, D.K.a.E.R., *The Role of Dynamics in Allosteric Regulation.* Curr. Opin. Struct. Biol., 2003. **13**: p. 748-757.

20. Wales, T.E. and J.R. Engen, *Hydrogen exchange mass spectrometry for the analysis of protein dynamics.* Mass Spectrometry Reviews, 2006. **25**(1): p. 158-170.

21. Stroobant, E.d.H.a.V., *Mass Spectrometry: Principles and Applications* 2007: Wiley.

22. Chance, M., *Mass Spectrometry Analysis for Protein-Protein Interactions and Dynamics*, 2008, Wiley.

23. Gross, J.H., *Mass Spectrometry*, in *digital Encyclopedia of Applied Physics*. 2003, Wiley-VCH Verlag GmbH & Co. KGaA.

24. Dole, M., L.L. Mack, and R.L. Hines, *Molecular Beams of Macroions.* J. Chem. Phys., 1968. **49**(5): p. 2240-50.

25. Yamashita, M. and J.B. Fenn, *Electrospray ion-source - Another Variation on the Free-Jet Theme.* J. Phys. Chem., 1984. **88**(20): p. 4451-4459.

26. Fenn, J.B., et al., *Electrospray ionization for mass-spectrometry of large biomolecules.* Science, 1989. **246**(4926): p. 64-71.

27. Liuni, P. and D.J. Wilson, *Understanding and optimizing electrospray ionization techniques for proteomic analysis.* Expert Rev Proteomics, 2011. **8**(2): p. 197-209.

28. Iribarne, J.V. and B.A. Thomson, *Evaporation of small ions from charged droplets.* J. Chem. Phys., 1976. **64**(6): p. 2287-2294.

29. Thomson, B.A. and J.V. Iribarne, *Field-induced ion evaporation from liquid surfaces at atmospheric-pressure.* J. Chem. Phys., 1979. **71**(11): p. 4451-4463.

30. Konermann, L., et al., *Unraveling the Mechanism of Electrospray Ionization.* Analytical Chemistry, 2012. **85**(1): p. 2-9.

31. Rolf Ekman, A.K., Dominic M. Desiderio, Nico M. Nibbering, *Mass spectrometry : instrumentation, interpretation, and applications* Wiley-Interscience series on mass spectrometry. 2009, Hoboken, N.J. : John Wiley & Sons.

32. Ferguson, R.E., K.E. McCulloh, and H.M. Rosenstock, *Observation of the Products of Ionic Collision Processes and Ion Decomposition in a Linear, Pulsed Time-of-Flight Mass Spectrometer.* The Journal of Chemical Physics, 1965. **42**(1): p. 100-106.

33. Franklin, J.L., P.M. Hierl, and D.A. Whan, *Measurement of the Translational Energy of Ions with a Time-of-Flight Mass Spectrometer.* The Journal of Chemical Physics, 1967. **47**(9): p. 3148-3153.

34. Chernushevich, I.V., A.V. Loboda, and B.A. Thomson, *An introduction to quadrupole–time-of-flight mass spectrometry.* J. Mass. Spectrom., 2001. **36**: p. 849-865.

35. Sali, A., et al., *From words to literature in structural proteomics.* Nature, 2003. **422**(6928): p. 216-25.

36. Engen, J.R. and D.L. Smith, *Investigating protein structure and dynamics by hydrogen exchange MS.* Analytical Chemistry, 2001. **73**(9): p. 256A-265A.

37. Kaltashov, I.A. and S.J. Eyles, *Studies of biomolecular conformations and conformational dynamics by mass spectrometry.* Mass Spectrom Rev, 2002. **21**(1): p. 37-71.

38. Chowdhury, S.K., V. Katta, and B.T. Chait, *Probing Conformational Changes in Proteins by Mass Spectrometry.* J. Am. Chem. Soc., 1990. **112**(24): p. 9012-9013.

39. Englander, S.W., *Protein folding intermediates and pathways studied by hydrogen exchange.* Annu. Rev. Biophys. Biomol. Struct., 2000. **29**: p. 213-238.

40. Englander, S.W., et al., *Mechanisms and uses of hydrogen exchange.* Current Opinion in Structural Biology, 1996. **6**(1): p. 18-23.

41. Zhang, Z.Q. and D.L. Smith, *Determination of amide hydrogen-exchange by mass-spectrometry- A new tool for protein-structure elucidation.* Protein Science, 1993. **2**(4): p. 522-531.

42. Perrin, C.L., *Proton exchange in amides: Surprises from simple systems.* Accounts of Chemical Research, 1989. **22**(8): p. 268-275.

43. Dempsey, C.E., *Hydrogen exchange in peptides and proteins using NMR-spectroscopy.* Prog. Nucl. Mag. Res. Sp., 2001. **39**(2): p. 135-170.

44. Bai, Y.W., et al., *Primary Structure Effects on Peptide Group Hydrogen-exchange.* Proteins, 1993. **17**(1): p. 75-86.

45. Englander, S.W. and N.R. Kallenbach, *Hydrogen-exchange and structural dynamics of proteins and nucleic-acids.* Quarterly Reviews of Biophysics, 1983. **16**(4): p. 521-655.

46. Sivaraman, T., C.B. Arrington, and A.D. Robertson, *Kinetics of unfolding and folding from amide hydrogen exchange in native ubiquitin.* Nat Struct Biol, 2001. **8**(4): p. 331-3.

47. Zhang, Z.Q., C.B. Post, and D.L. Smith, *Amide hydrogen exchange determined by mass spectrometry: Application to rabbit muscle aldolase.* Biochemistry, 1996. **35**(3): p. 779-791.

48. Krishna, M.M.G., et al., *Hydrogen exchange methods to study protein folding.* Methods, 2004. **34**(1): p. 51-64.

49. Engen, J.R., et al., *Identification and localization of slow, natural, cooperative unfolding in the hematopoietic cell kinase SH3 domain by amide hydrogen exchange and mass spectrometry.* Biochemistry, 1997. **36**(47): p. 14384-91.

50. Douglas A. Simmons, S.D.D.a.L.K., *Conformational Dynamics of Partially Denatured Myoglobin Studied by Time-Resolved Electrospray Mass Spectrometry with Online Hydrogen-Deuterium Exchange.* Biochemistry, 2003. **42**: p. 5896-5905.

51. Deng, Y., Z. Zhang, and D.L. Smith, *Comparison of continuous and pulsed labeling amide hydrogen exchange/mass spectrometry for studies of protein dynamics.* J Am Soc Mass Spectrom, 1999. **10**(8): p. 675-84.

52. Bogdanov, B. and R.D. Smith, *Proteomics by FTICR mass spectrometry: Top down and bottom up.* Mass Spectrom. Rev., 2005. **24**(2): p. 168-200.

53. Kaltashov, I.A., C.E. Bobst, and R.R. Abzalimov, *H/D Exchange and Mass Spectrometry in the Studies of Protein Conformation and Dynamics: Is There a Need for a Top-Down Approach?* Anal. Chem., 2009. **81**(19): p. 7892-7899.

54. Kaltashov, I.A. and S.J. Eyles, *Crossing the phase boundary to study protein dynamics and function: combination of amide hydrogen exchange in solution and ion fragmentation in the gas phase.* J Mass Spectrom, 2002. **37**(6): p. 557-65.

55. Zubarev, R.A., N.L. Kelleher, and F.W. McLafferty, *Electron capture dissociation of multiply charged protein cations. A nonergodic process.* J. Am. Chem. Soc., 1998. **120**(13): p. 3265-3266.

56. Nemeth-Cawley, J.F., B.S. Tangarone, and J.C. Rouse, *"Top down" characterization is a complementary technique to peptide sequencing for identifying protein species in complex mixtures.* J. Proteome Res., 2003. **2**(5): p. 495-505.

57. Rosa, J.J. and F.M. Richards, *An experimental procedure for increasing the structural resolution of chemical hydrogen-exchange measurements on proteins: application to ribonuclease S peptide.* J Mol Biol, 1979. **133**(3): p. 399-416.

58. Zhang, Z.Q. and D.L. Smith, *Determination of Amide Hydrogen Exchange by Mass Spectrometry - A New Tool for Protein Structure Elucidation.* Protein Sci., 1993. **2**(4): p. 522-531.

59. Smith, D.L., Y. Deng, and Z. Zhang, *Probing the non-covalent structure of proteins by amide hydrogen exchange and mass spectrometry.* J Mass Spectrom, 1997. **32**(2): p. 135-46.

60. Cravello, L., D. Lascoux, and E. Forest, *Use of different proteases working in acidic conditions to improve sequence coverage and resolution in hydrogen/deuterium exchange of large proteins.* Rapid Commun Mass Spectrom, 2003. **17**(21): p. 2387-93.

61. Wilson, D.J. and L. Konermann, *A Capillary Mixer with Adjustable Reaction Chamber Volume for Millisecond Time-Resolved Studies by Electrospray Mass Spectrometry.* Anal. Chem., 2003. **75**: p. 6408 - 6414.

62. Resetca, D. and D.J. Wilson, *Characterizing Rapid, Activity-Linked Conformational Transitions in Proteins via Sub-Second Hydrogen Deuterium Exchange Mass Spectrometry.* FEBS Journal, 2013.
63. Manz, A., N. Graber, and H.M. Widmer, *Miniaturized total chemical analysis systems: A novel concept for chemical sensing.* Sensors and Actuators B: Chemical, 1990. **1**(1-6): p. 244-248.
64. Chován, T. and A. Guttman, *Microfabricated devices in biotechnology and biochemical processing.* TiBS, 2002. **20**(3): p. 116-122.
65. Bassous, E., H.H. Taub, and L. Kuhn, *Ink jet printing nozzle arrays etched in silicon.* Applied Physics Letters, 1977. **31**(2): p. 135-137.
66. Petersen, K.E. and K.E. Petersen, *Fabrication of an integrated, planar silicon ink-jet structure.* Electron Devices, IEEE Transactions on, 1979. **26**(12): p. 1918-1920.
67. Gravesen, P., J. Branebjerg, and O.S. Jensen, *Microfluidics-a review.* Journal of Micromechanics and Microengineering, 1993. **3**(4): p. 168.
68. Wang, Y., et al., *Microarrays assembled in microfluidic chips fabricated from poly(methyl methacrylate) for the detection of low-abundant DNA mutations.* Anal. Chem., 2003. **75**(5): p. 1130-1140.
69. Yager, B.H.W.a.P., *Microfluidic Diffusion-Based Separation and Detection.* Science, 1999. **283**(5400): p. 346-347.
70. Lazar, I.M., J. Grym, and F. Foret, *Microfabricated devices: A new sample introduction approach to mass spectrometry.* Mass Spectrometry Reviews, 2006. **25**(4): p. 573-594.
71. Aebersold, R. and M. Mann, *Mass spectrometry-based proteomics.* Nature, 2003. **422**(6928): p. 198-207.
72. Domon, B. and R. Aebersold, *Review - Mass spectrometry and protein analysis.* Science, 2006. **312**(5771): p. 212-217.
73. Regenfuss, P., et al., *Mixing Liquids in Microseconds.* Rev. Sci. Instrum., 1985. **56**(2): p. 283-290.
74. Krenkova, J. and F. Foret, *Immobilized microfluidic enzymatic reactors.* Electrophoresis, 2004. **25**(21-22): p. 3550-63.

75. Jeonghoon, L., A.S. Steven, and K.M. Kermit, *Microfluidic chips for mass spectrometry-based proteomics.* J. Mass. Spectrom., 2009. **44**(5): p. 579-593.

76. Pinto, D.M., Y.B. Ning, and D. Figeys, *An enhanced microfluidic chip coupled to an electrospray Qstar mass spectrometer for protein identification.* Electrophoresis, 2000. **21**(1): p. 181-190.

77. Hoffmann, P., et al., *Microfluidic glass chips with an integrated nanospray emitter for coupling to a mass spectrometer.* Angew. Chem.-Int. Edit., 2007. **46**(26): p. 4913-4916.

78. Zhang, B.L., F. Foret, and B.L. Karger, *High-throughput microfabricated CE/ESI-MS: Automated sampling from a microwell plate.* Anal. Chem., 2001. **73**(11): p. 2675-2681.

79. Ramsey, R.S. and J.M. Ramsey, *Generating Electrospray from Microchip Devices Using Electroosmotic Pumping.* Analytical Chemistry, 1997. **69**(6): p. 1174-1178.

80. Sun, X., et al., *Rapid prototyping of poly(methyl methacrylate) microfluidic systems using solvent imprinting and bonding.* Journal of Chromatography A, 2007. **1162**(2): p. 162-166.

81. Xue, Q.F., et al., *Multichannel microchip electrospray mass spectrometry.* Anal. Chem., 1997. **69**(3): p. 426-430.

82. Song, H., J.D. Tice, and R.F. Ismagilov, *A microfluidic system for controlling reaction networks in time.* Angew. Chem.-Int. Edit., 2003. **42**(7): p. 768-772.

83. Joseph H. Spurk, N.A., *Fluid mechanics*. 2nd ed. 2008, Berlin Springer.

84. Stone, H.A., A.D. Stroock, and A. Ajdari, *Engineering flows in small devices: Microfluidics toward a lab-on-a-chip.* Annual Review of Fluid Mechanics, 2004. **36**: p. 381-411.

85. Brody, J.P., et al., *Biotechnology at low Reynolds numbers.* Biophys. J., 1996. **71**(6): p. 3430-3441.

86. Hardt, S., et al., *Passive micromixers for applications in the microreactor and mu TAS fields.* Microfluid. Nanofluid., 2005: p. 108-118.

87. Hartman, R.L. and K.F. Jensen, *Microchemical systems for continuous-flow synthesis.* Lab on a Chip, 2009. **9**(17): p. 2495-2507.

88. Khan, I.A., *Fluid mechanics*. 1987, New York : Holt: Rinehart & Winston.

89. Stroock, A.D., et al., *Chaotic mixer for microchannels.* Science, 2002. **295**(5555): p. 647-651.

90. Yam, K.L., D.K. Anderson, and R.E. Buxbaum, *Diffusion of Small Solutes in Polymer-Containing Solutions.* Science, 1988. **241**(4863): p. 330-332.

91. Brody, J.P. and P. Yager, *Diffusion-based Extraction in a Microfabricated Device.* Sensors and Actuators a-Physical, 1997. **58**(1): p. 13-18.

92. *Lasers in manufacturing* 1st ed, ed. J.P. Davim. 2012, Hoboken, NJ: Wiley.

93. Hecht, J., *Understanding lasers an entry-level guide*. 3rd ed. 2008: John Wiley & Sons.

94. Miyazaki, M., et al., *Enzymatic processing in microfluidic reactors.* Biotechnol Genet Eng Rev, 2008. **25**: p. 405-28.

95. Erickson, D. and D.Q. Li, *Integrated microfluidic devices.* Anal. Chim. Acta, 2004. **507**(1): p. 11-26.

96. Fan, H.Z., et al., *Fabrication and performance of poly(methyl methacrylate) microfluidic chips with fiber cores.* J. Chromatogr. A, 2008. **1179**(2): p. 224-228.

# CHAPTER 2

## A Versatile Microfluidic Chip for Millisecond Time-scale Kinetic Studies by Electrospray Mass Spectrometry

*__Adapted from__ J. Am. Soc. Mass Spectr. 20 (1): 124-130*

## 2.1 INTRODUCTION

Microfluidics involves the fabrication of micro-scale features, usually in glass [1-3] or polymer substrates [4, 5], to enable the precise handling of small volume liquid samples. Micro-scale liquid handling facilitates mass and heat transfer, reduced sample consumption and high throughput *via* parallelization while minimizing sample loss and cross contamination [6-8]. Virtually any laboratory process involving fluid handling can be miniaturized to capitalize on these advantages. There is therefore widespread interest in the development of modular 'lab on a chip' devices with integrated sample preparation, separation and reactor functionality [9]. There are a number of options for 'on-chip' analysis including sensors that are optically [10-12], electrically [13, 14] or even mechanically based [15].

While technically 'off-chip', ESI-MS is effectively an 'on-chip' analysis if it is initiated directly from the microfluidic channel outlet [16-18]. Generation of stable ESI signals from the outlets of microfluidic devices is challenging. Contact between liquid expelled from the outlet and the edge of the chip typically results in large, unstable Taylor cones. Several approaches have been devised to improve signal stability in ‘on-chip’ ESI experiments including the integration of hydrophobic membranes [19] or porous polymer monoliths [20] at the channel outlet. The simplest approach is to limit the eluent/chip contact surface area by spraying from the corner of the chip or by tapering the outlet [16].

ESI Coupled Microfluidic Devices (ECMDs) have been devised for numerous applications, particularly in the area of proteomics [8]. The complimentary advantages of microfluidic liquid handling and ESI-MS based analysis make these devices a natural answer to the challenges of proteomic studies. Apart applications in the area of proteomics, however, the vast potential of ECMDs remains largely untapped. One ‘underrepresented’ application is rapid microfluidic mixing for time-resolved studies by ESI-MS [16, 21].

Time-resolved electrospray ionization Mass Spectrometry (TR ESI-MS) is a powerful approach for the characterization of short-lived, ‘transient’ intermediates in biochemical reactions [22-29]. Transient intermediates are critical to the biological activity of proteins, from enzymatic reactions [26, 30] to protein folding [31, 32], and are therefore potential targets for rational drug design. The transient adoption of partially unfolded conformations is also a factor in pathogenic protein aggregation, amyloidosis, which is associated with a number of human diseases including Alzheimer’s, Parkinson’s and Creutzfeldt-Jacob disease [33, 34]. By TR ESI-MS, transient protein folding species are identified by their charge-state distribution [35] or (with an additional mixing step) by their hydrogen/deuterium exchange (HDX) profile [36]. Transient covalent or non-covalent modifications are detected as mass shifts in the protein molecular ion corresponding the mass of the binding partner [23]. This represents considerably more detail than what can typically be acquired in conventional optical time-resolved studies, and the analysis does not require artificial chromophoric labels.

In order for TR ESI-MS to present a viable alternative to optical time-resolved methods, however, it must be possible to acquire complete a reaction time-courses in a single experiment. This motivated the development of ‘Stopped Flow ESI-MS’ by Kolakowski and Konermann in 2000 [28, 29]. In 2003, Wilson and Konermann introduced a continuous flow capillary mixer for TR ESI-MS that facilitated full time-course acquisitions on time-scales comparable to optical stopped flow experiments [22]. This approach has enabled numerous investigations [22-24, 35-38], but the concentric capillary design is limiting in terms of reproducibility of fabrication and is not well suited to the inclusion of directly coupled sample preparation or separation steps.

This work introduces a new microfluidic device for TR ESI-MS. The device incorporates an internal capillary mixer that is similar to the one in reference [22], but formed by laser ablation with greatly improved reproducibility. The microfluidic design is simple, involving two intersecting channels, two inlets and a tapered outlet for stable, low dead-volume ‘on-chip’ ESI. Fabrication is fast, straightforward, reproducible and inexpensive. Device performance is characterized by monitoring acid induced cytochrome c unfolding kinetics, in the course of which a previously unreported intermediate is detected. To enable the extraction of reliable rate constants, a theoretical framework for the analysis of kinetic data acquired under laminar flow in a square channel is devised.

## 2.2 EXPERIMENTAL

**2.2.1 Chemicals and Supplies.** Horse heart cytochrome c was purchased from Sigma (St. Louis, MO). Ultrapure water was generated in-house on a Millipore Milli-Q Advantage A10 system. High purity acetic acid (99.7+ %) was purchased from Sigma. Blank PMMA substrates with dimension (l = 8.9 cm, w = 3.8 cm, h = 0.3 cm) were supplied by Professional Plastics (Fullerton, CA). Polyimide coated glass capillaries (O.D. 153 μm, I.D. 75 μm) were supplied by Polymicro Technologies (Pheonix, AZ). Metal capillaries (O.D. 400 μm, I.D. 200 μm) were from Small Parts, Inc. (Miramar, FL). PTFE tubing (O.D. 1/16″, I.D. 400 μm) was purchased from McMaster Plastics (Scarborough, ON). Standard 1/16″ fittings were supplied by Upchurch (Oak Harbour, WA).

**2.2.2 Microfluidic Device Fabrication.** The microfluidic reactor was fabricated using a VersaLaser™ engraving device (Universal Laser, Scottsdale, AZ). The microfluidic channel design was generated in CorelDraw X3 (Corel, Ottawa, ON). Laser power and mode were differentiated by color (red = vector mode cutting, blue = vector mode marking, black = raster mode). Microfluidic channel widths were adjusted to 155 μm ± 2 by slightly defocusing the laser. The channels were engraved into blank PMMA substrate to a depth of 155 μm ± 2 using two vector marking runs at 2.2 J/cm$^2$. The distal end of the device was cut to a sharp tip using vector cutting mode at 4.6 J/cm$^2$. At the proximal end of the device, channels were connected to external 1/16″ Upchurch fittings by using thin-walled metal capillaries as 'step up' unions. The metal capillaries were melted into the channel inlets at one end and pressure fit into 1/16″ O.D. PTFE tubing at the other.  A second blank PMMA substrate was used as the cover. The chip and cover were placed in a vice (~5 MPa) and thermally bonded in a convection oven (120 °C for 40 min). Fluids were introduced into the device using Harvard 11+ infusion pumps (Holliston, MA). Typical flow rates were 7.0 µL/min for both reactants. A picture of the device is shown in Figure 2.1A. The main microfluidic channel was sized to accommodate a 153 µm O.D. fused silica 'mixing capillary'. The distal end of the capillary was sealed with molten fused silica by cutting at high laser power. Vector marking mode (+7%) was used to cut a notch in the capillary 2 mm from the sealed end. A microscopic view of the mixer inside the main microfluidic channel is provided in Figure 2.1B. Fluid passing through the capillary exits through the notch and is forced into the narrow space between the capillary and the channel walls. Here it mixes with fluid that has passed through the channel around the inner capillary. The observed reaction time is adjusted by changing the position of the mixing capillary within the channel. Early reaction times are observed when the mixer is positioned close to the ESI outlet. Steadily distancing the mixer from the ESI outlet yields mass spectra corresponding to steadily later reaction times.

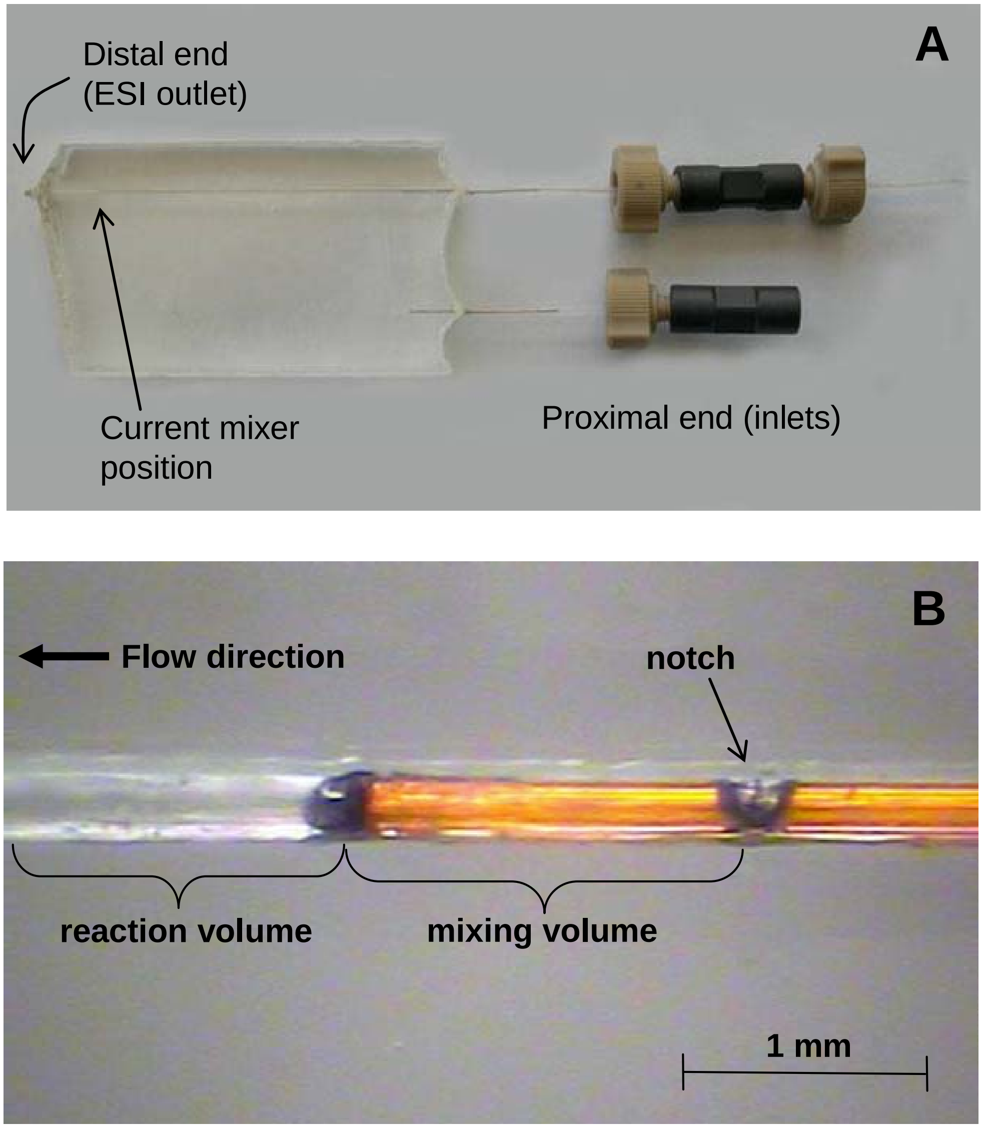

**Figure 2.1**. A macroscopic view of the reactor is shown in panel **A**. The main channel runs the length of the device and accommodates a 153 μm O.D. fused silica ‘mixing capillary’. A second channel delivers fluid into the main channel and around the mixing capillary. Panel **B** provides a microscopic view of the distal end of the mixing capillary within the main channel. The total volume of the mixing region is ~ 10 nL. Moving the mixing capillary within the main channel changes the reaction volume and thus the delay between mixing and ESI.

**2.2.3 TR ESI-MS experiments.** Time-resolved mass spectrometry was carried out on a QStar Elite Q-TOF instrument (MDS Analytical Technologies, Concord, ON) with an in-house built source assembly. The source recognition logic was circumvented using a custom switch. The instrument was operated in positive ion mode with source voltage +5500 V and moderate declustering conditions (Declustering potential (DP) = 60 – 90 V, Focusing Ring (FP) = 200 – 250 V). In a typical kinetic run, the distal end of the mixing capillary was initially positioned at the ESI outlet of the main microfluidic channel. The solution passing through the mixing capillary was 10 μM cytochrome c in ultrapure water. The solution passing around the mixing capillary was 10% (v/v) acetic acid in ultrapure water. Both solutions were injected at a rate of 7 μL/min. Kinetics were measured by withdrawing the mixing capillary at a rate of $2.0 \times 10^{-4}$ m/s such that the reaction volume (the volume between the end of the mixing capillary and the ESI outlet) increased at a rate of 0.3 μL/min. As the mixing capillary was withdrawn, full ESI mass spectra were acquired at a rate of 1 $s^{-1}$. This corresponds to a mass spectrum every 20 ms of reaction time. However, the relationship between delay volume and analyte age is complicated by laminar flow as discussed in the theory and data analysis section.

## 2.3 THEORY and DATA ANALYSIS

**2.3.1 Laminar Flow in a Square Channel.** At ESI-compatible flow rates, flow through microfluidic channels is laminar. Square channel laminar flow is characterized by a 3 dimensional parabolic velocity profile (Figure 2.2).

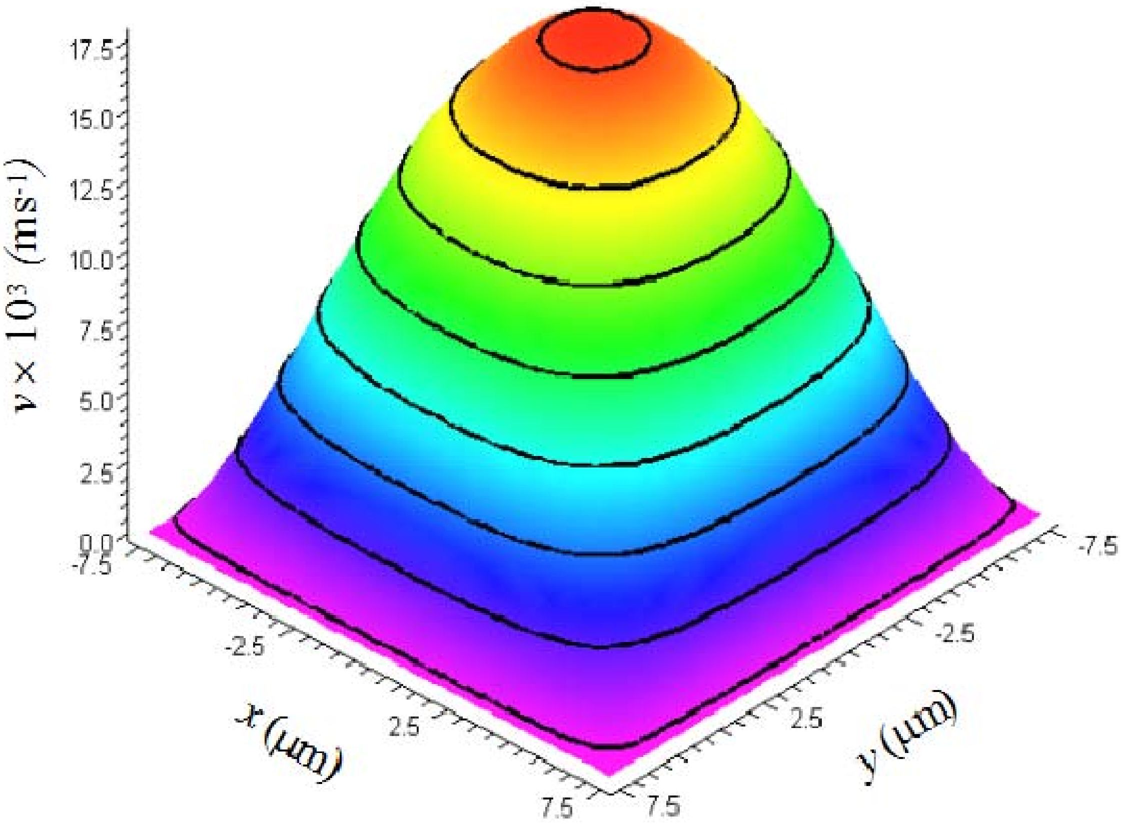

**Figure 2.2**. A model of the laminar flow velocity profile within the reaction channel, based on expression (2.1). Solid lines represent contours with constant velocity. The radially asymmetric shape of the contours emphasizes that rectangular channel velocity profiles cannot be accurately approximated by assuming a circular geometry.

The general expression for the velocity profile in a rectangular channel is given by [39]:

$$v(x,y) = v_{\max}\left(1-\left(\frac{|x|}{X}\right)^{n_x}\right)\left(1-\left(\frac{|y|}{Y}\right)^{n_y}\right) \tag{2.1}$$

Equation (2.1) uses a Cartesian coordinate system whose origin is at the center of the channel. $X$ and $Y$ are the distances from the center of the channel to the wall in the width and height dimensions, respectively (*i.e.* $X$ = ½ channel width, $Y$ = ½ channel height). The coordinates $x$ and $y$ can therefore have values in the ranges $-X..X$ and $-Y..Y$. The exponents $n_x$ and $n_y$ are calculated from the aspect ratio of the channel, $\alpha$ = height/width. For $\alpha \geq \frac{1}{3}$, $n_x = 2 + 0.3(\alpha-\frac{1}{3})$ and $n_y = 1.7 + 0.5\alpha^{-1.4}$ [39]. In the present case, the channel is square, such that $n_x = n_y = 2.2$. The maximum flow velocity $v_{\max}$ can be calculated from the average flow velocity $v_{\text{avg}}$ by:

$$v_{\max} = v_{avg}\left(\frac{n_x+1}{n_x}\right)\left(\frac{n_y+1}{n_y}\right) \tag{2.2}$$

The laminar flow velocity profile convolutes our kinetic data; analytes occupying the center of the channel will be ‘younger’ when they arrive at the ESI source than analytes near the channel walls. To account for this, we can derive a probability distribution function $P(a)$ that gives the probability of detecting an analyte of age $a$ for a given reaction channel length $l$. Combining $P(a)$ with an expression for analyte concentration as a function of age $C(a)$ and integrating from $a = l/v_{max}$ to $a = \infty$, gives the average concentration of analyte at the ESI outlet $C_{avg}$, which is assumed to be proportional to the ESI signal intensity [40]:

$$C_{avg} = \int_{l/v_{\max}}^{\infty} P(a)C(a)da \tag{2.3}$$

This approach for analyzing kinetic data acquired under laminar flow conditions was introduced by Konermann in 1999 [40]. However, in that work $P(a)$ was derived for a circular geometry. In a circular tube, the laminar flow velocity profile is radially symmetric and therefore dependent on a single geometric parameter $r$ (distance from the tube center). In a rectangular channel, the velocity profile is a function of both $x$ and $y$. We must therefore use a different approach to calculate $P(a)$.

For a given $l$, we can define a function $G(a_0)$ that gives the total number of particles with velocity $v \geq l/a_0$ (age $a \leq a_0$) passing through the detector per unit time:

$$G(a_0) = \rho \int_{-y_b}^{y_b} \int_{-x_b}^{x_b} v(x,y)dxdy \tag{2.4}$$

The constant $\rho$ represents an analyte concentration factor. To simplify the integral, we can take advantage of the $x$ and $y$ axis symmetry of $v(x,y)$ and restrict our derivation to the $+x$, $+y$ quadrant. The range of $x$ and $y$ is thereby constrained to x = 0..X and y = 0..Y and the expression is multiplied by 4. An additional simplification for square channels is that X=Y and $n_x = n_y$.

Incorporating these simplifications, and using the condition $v \geq l/a_0$, the upper limits of integration are:

$$y_b = Y\left(1 - \frac{l}{a_0 v_{\max}}\right)^{\frac{1}{n}} \quad \text{and} \quad x_b = Y\left(1 - \frac{l}{a_0 v_{\max}\left(1 - \left(\frac{y}{Y}\right)^n\right)}\right)^{\frac{1}{n}} \qquad (2.5)$$

And expression (2.4) becomes:

$$G(a_0) = 4Y\rho v_{\max}\int_{y=0}^{y_b}\int_{x=0}^{x_b}\left(1 - \left(\frac{x}{Y}\right)^n\right)\left(1 - \left(\frac{y}{Y}\right)^n\right)dxdy \qquad (2.6)$$

Using the limits $y_b$ and $x_b$, expression (2.6) defines a cross sectional area of $v(x, y)$ bounded by the velocity contour $v = l/a_0$ . The expression can be integrated analytically in one dimension, but the resulting integral must be solved numerically for most cases of $a_0$.

From expression (2.6), it is evident that the fraction of analyte passing through the detector within the area bounded by $G(a_0)$ is $G(a_0)/G(a_0=\infty)$. This fraction can also be defined as the probability of detecting an analyte with age $a \leq a_0$. It follows, therefore, that the probability of detecting an analyte with a *particular* age, $P(a)$ is:

$$P(a) = \frac{G(a_0) - G(a_0 - \Delta a)}{G(a_\infty)} \qquad (2.7)$$

where Δa is the width of the age interval. Note that calculations of P(a) become more accurate as Δa → 0. Figure 2.3 plots $P(a)$ for several reaction channel lengths. $P(a)$ can now be substituted into Equation (2.3) for 'square channel laminar flow corrected' analysis of the kinetic data. This derivation of $P(a)$ is more general than those developed previously. It can be used for any channel geometry provided that there is at least one axis of symmetry.

**2.3.2 Other considerations**. The analytical framework introduced above applies only to a fully realized laminar flow. Laminar flow develops over an entrance length $l_{\mathrm{ent}}$ that is easily approximated for a rectangular geometry; $l_{\mathrm{ent}} \approx 2.4\, A/P$ where $A$ and $P$ are the area and perimeter the perimeter of the microfluidic channel [41]. In the present study, $l_{\mathrm{ent}} = 4.5 \times 10^{-5}$ m, less than 1/5 the shortest $l$ used ($2.0 \times 10^{-4}$ m). We therefore consider the effects of $l_{\mathrm{ent}}$ on the kinetic data to be negligible. Data analysis might also be convoluted by Taylor dispersion-based distortion of the laminar flow velocity profile. However, on the scale of the reaction channel (155 μm × 155 μm), significant distortion of the laminar flow profile occurs on the order of seconds [22], much longer than the timescale of our kinetic experiments (final time point = 0.65 sec). The effects of Taylor dispersion can therefore also be neglected.

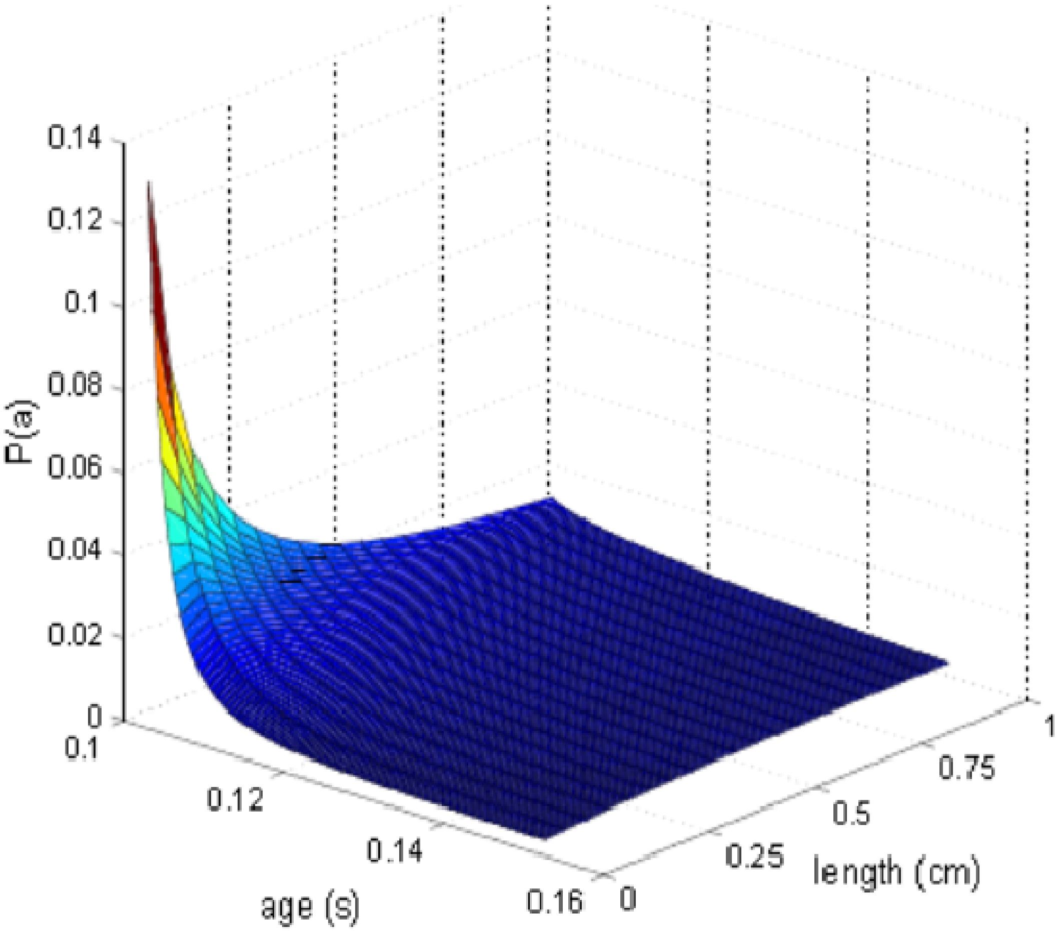

**Figure 2.3** A probability density *P*(*a*, *l*) giving the probability of detecting particles of particular ages at various reaction channel lengths. In expression (2.3), *P*(*a*) is combined with a function describing changing concentration as a function of age due to the reaction, *C*(*a*), to give a laminar flow corrected time-dependent ESI signal intensities.

## 2.4 RESULTS AND DISCUSSIONS

**2.4.1 Fabrication.** One of the aims of this work was to devise fast, simple and reproducible protocol for Electrospray coupled microfluidic device (ECMD) fabrication. Conventional approaches for the fabrication of ECMDs include photolithography [42, 43] and polymer imprint techniques [20, 44]. Elegant, highly detailed microscale features can be generated using these methods, but they require specialized facilities, equipment and expertise. While efforts are being made to simplify photolithographic and polymer imprint fabrication [43], most protocols still require days to go from design to completion. In the present study, microchannels and the microfluidic mixer were formed by laser ablation using an inexpensive VersaLaser™ engraving device.

Laser ablation has some disadvantages relative to other microfabrication techniques. Firstly, the generation of ultrafine features is limited by the dot size of the laser and thermal conduction causing melting around the laser dot. Equipped with high resolution optics, the engraving device used in the present study can generate a dot size of ~ 15 μm, which, in PMMA, corresponds to a minimum feature size of ~ 30 μm. Since the microfluidic reactor is composed of features that are much larger than this (155 μm), the standard resolution optics were sufficient. Secondly, microfluidic channels generated by laser ablation are not perfectly rectangular, but rounded at their base. The extent of this effect depends on a number of factors including the quality of laser and optics used, but always increases with the aspect ratio $\alpha$. We found that the VersaLaser™ could generate an essentially rectangular channel in PMMA up to $\alpha \approx 1.3$, which is well above our requirements ($\alpha = 1$).

The main advantage of our fabrication approach is that it is exceedingly straightforward. In this study, designs were generated using widely available illustration software (CorelDraw X3) and then simply ‘printed’ onto the PMMA substrate. The fabrication process therefore requires no specialized expertise or facility. The production cycle is also extremely rapid. Prototypes of the microfluidic reactor generally required < 2.5 hours from design to completion.

**2.4.2 Mixing.** In time-resolved experiments, mixing is almost always the main contributor to dead-time. The design of efficient mixers is a major branch of microfluidics research [45-47]. Approaches such as hydrodynamic focusing or the generation of chaotic flow can result in extremely efficient mixing on the micro-scale [16, 45, 47]. The microfluidic reactor introduced in the present study incorporates a mixer that is integrated into the distal end of the mixing capillary (Figure 2.3). The mixer operates by forcing reactant solutions to flow together through the narrow space between the mixing capillary and the channel walls. Since this space is defined by a round capillary tightly fit into a square channel, the minimum mixing efficiency occurs at the corners where the distance between the capillary and the channel walls is ~ 65 μm. For a mixer length of 2 mm, the total volume of the mixing region is ~ 10 nL. This corresponds to an average mixing time of ~ 43 ms in our experiments.

Given the complications of flow within the mixer (*i.e.* complex geometry, a developing laminar flow profile *etc.*) it is not feasible to devise a theoretical model to predict mixing efficiency. However an estimate of diffusion length, $L_D = (4Dt)^{1/2}$ where $D$ is the diffusion coefficient of protons in bulk water ($\sim 1\times10^{-8}$ m$^2$s$^{-1}$) [48], gives an average distance of 41.5 μm in 43 ms. Therefore, assuming that the laminar flow layer containing excess protons occupies half of the distance from the capillary to the channel wall, it is not unreasonable to expect complete equilibration of proton concentration within the mixer based on diffusion alone. Furthermore, massive rearrangement of the laminar flow profile upon the incorporation of fluid exiting the notch may significantly enhance mixing efficiency [49].

Mixing efficiency was gauged experimentally by changing the length of the mixer and monitoring the effects on the measured cytochrome c unfolding kinetics. It was observed that when the notch was positioned between 0.5 and 1.5 mm from the end of the mixing capillary, a fraction of the folded protein population did not undergo rapid unfolding, but rather decreased slowly and linearly as a function of time (data not shown). Both the magnitude of this persistent folded population, and the rate at which it was eliminated, were dependent on mixer length. This is exactly the result expected if mixing is incomplete upon transfer to the reaction channel. Unmixed fluid passing into the reaction channel will form a laminar flow layer within which native conditions persist. This layer will slowly be eliminated via inefficient diffusive mixing with surrounding flow layers. Ultimately, it was determined that a mixer length of 2 mm was required for complete mixing prior to transfer into the reaction channel.

**2.4.3 On-Chip Electrospray and Instrument Dead-time.** The two main considerations for TR ESI-MS experiments with respect to electrospray performance are Taylor cone volume and stability. Taylor cone volume is especially significant because it contributes to the dead-time of the experiment. Taylor cones generated ‘on-chip’ tend to be larger than those produced at conventional capillary outlets due to interactions between the eluent and the edge of the substrate

[50]. In this respect, the use of PMMA, which is quite hydrophilic, is disadvantageous. In the present study, an effort was made to reduce spreading by tapering the ESI outlet to a sharp point. In addition, source potentials were at least 300 V higher than the minimum required to generate a stable Taylor cone. From scaled pictures taken on a CCD camera (Figure 2.4A), and assuming a radially symmetric shape, Taylor cone volumes were estimated to be in the range of 1 – 3 nL, corresponding to 4 – 12 ms of dead-time at 14 μL/min. The dead-time of the microfluidic reactor was therefore 43 ms (mixing) + 12 ms (taylor cone) + 1 ms (desolvation [51]) ≈ 56 ms.

Taylor cone stability is the dominant factor affecting variability in ESI signal intensity. In TR ESI-MS experiments, Taylor cone instability results in noisy and in extreme cases un-interpretable kinetic data. Signal stability for ECMDs with ‘on-chip’ ESI is generally lower than that of capillary-based devices and the present microfluidic reactor is no exception. Figure 2.4B shows a typical TIC of 5 μM cytochrome c in 5% (v/v) acetic acid at a reaction time of 250 ms (roughly halfway through the unfolding process). Over 5 minutes of data collection, the standard deviation for TIC signal intensity was 5,219 or 2.8%. This degree of signal stability was more than sufficient to provide reliable kinetic data.

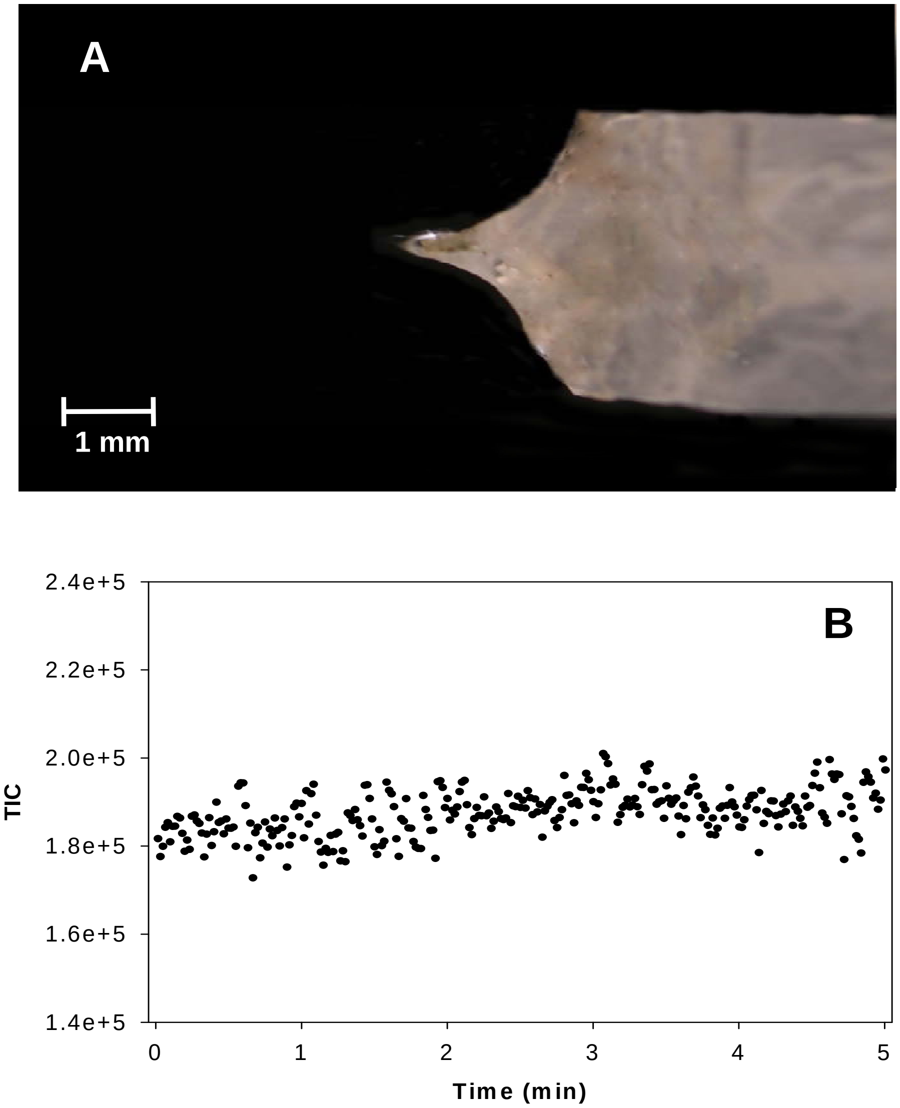

**Figure 2.4**. Panel **A** shows a representative image from a series of images used to estimate Taylor cone volume. The ESI outlet of the device was ~ 4 mm from the curtain plate (digitally removed from the image) which was held at -1000 V. Source potential was +5500 V. A stable Taylor cone was observed at a source potential of +5250 V under these conditions. Panel **B** shows the TIC for a 5 μM solution of cytochrome c in 5% acetic acid. The mixing capillary was positioned to allow 250 ms of reaction time. Source conditions were the same as panel **A**. The signal has a standard deviation of 5219 or 2.8%.

**2.4.4 Cytochrome c Unfolding.** Cytochrome *c* is a small heme protein from the inner membrane of the mitochondrion. In comparison to other proteins, the biophysical properties of cytochrome c have been extensively characterized [31, 52-56]. Cytochrome *c* is highly amenable to ESI, making it a convenient test subject for new MS-based analytical approaches [57-60]. The folding kinetics of cytochrome *c* are well studied [61] and were among the first processes to be investigated by time-resolved ESI-MS [25]. Kinetic cytochrome *c* *un*folding studies are less common, possibly due to the assumption that transient intermediates will not become populated under strongly denaturing conditions and that therefore unfolding will be mechanistically uninteresting [62]. Kinetic unfolding intermediates of cytochrome *c* have been detected in optical studies, however [55, 63].

Acid induced cytochrome *c* unfolding was used to gauge the effectiveness of our microfluidic reactor for monitoring millisecond time-scale kinetics. The reactor was first operated in 'spectral mode' in which the mixer is fixed at various positions within the main channel. Spectral mode allows the reaction to be monitored indefinitely at fixed time-points, facilitating the acquisition of high signal-to-noise mass spectra. Figure 2.5 shows mass spectra corresponding to cytochrome *c* unfolding at 70 ms (A), 200 ms (B) and 650 ms (C). Between 70 ms and 200 ms, there is a shift in the dominant charge state from 8+ to 9+, suggesting the involvement of a partially unfolded, 'native-like' intermediate in the unfolding process. The transition from the intermediate to the unfolded protein appears to occur in a single step.

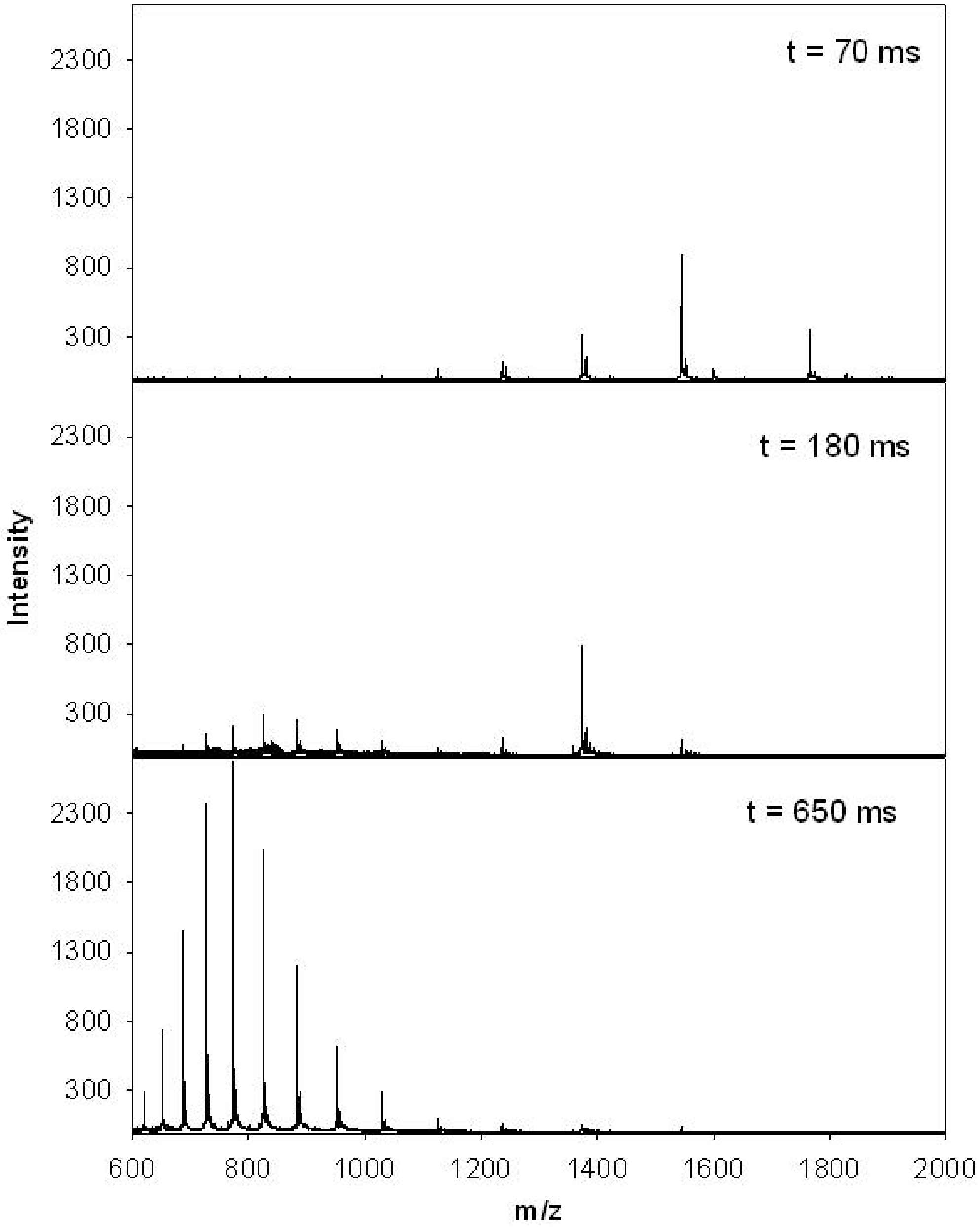

**Figure 2.5.** TR ESI mass spectra of kinetic cytochrome c unfolding at 70 ms, 200 ms and 650 ms. Conditions after mixing were 5 μM cytochrome c in 5% (v/v) acetic acid. A rapid transition was observed from a folded form of the protein with dominant charge state 8+ to an unfolding intermediate with dominant charge state 9+. The transition from 9+ to a broad distribution centered on 16+ occurred over a longer time-frame.

A more detailed analysis can be carried out in 'kinetics mode' where the mixing capillary is steadily withdrawn while mass spectra are collected. Figure 2.6 shows the results of a typical kinetics mode experiment. Each trace represents the ion current for peaks corresponding to various charge states of cytochrome *c* from 7+ to 19+. The observed kinetics can be roughly subdivided into three categories: Charge states 7+ and 8+ undergo monophasic exponential decay. Charge states 9+ and 10+ exhibit classic intermediate kinetics *i.e.* an exponential rise followed by an exponential decay. The intensities of charge states 11+ - 18+ increase exponentially after a brief delay.

The data were fit to expression (2.3) using a FORTRAN program developed previously [22] adjusted for square channel laminar flow as described in theory section. Fits are shown as solid lines in Figure 2.6. The data were analyzed using an implicit global analysis strategy based on that in reference [35]. The concentration vs. time dependences for each cytochrome *c* charge state, $C(a, m/z)$, were assumed to correspond to a sum of exponentials plus an offset. It was found that two exponentials were sufficient to obtain satisfactory fits to all of the kinetic data. The first exponential, associated with the formation of the intermediate, had a rate constant $k_{1\mathrm{obs}} = 32\ \mathrm{s}^{-1} \pm 5$. This is in agreement with stopped-flow fluorescence data acquired by Bhuyan *et al.* [56] in 3.1 M GdnHCl, although it is difficult to make a direct comparison given the significantly different conditions employed in that study. The second exponential is associated with the transition from the intermediate to the 'unfolded' protein. This process was found to occur at $k_{2\mathrm{obs}} = 7.5\ \mathrm{s}^{-1} \pm 0.1$. This rate agrees with the slow unfolding phase observed by Bhuyan *et al.* by stopped flow far UV-CD [56].

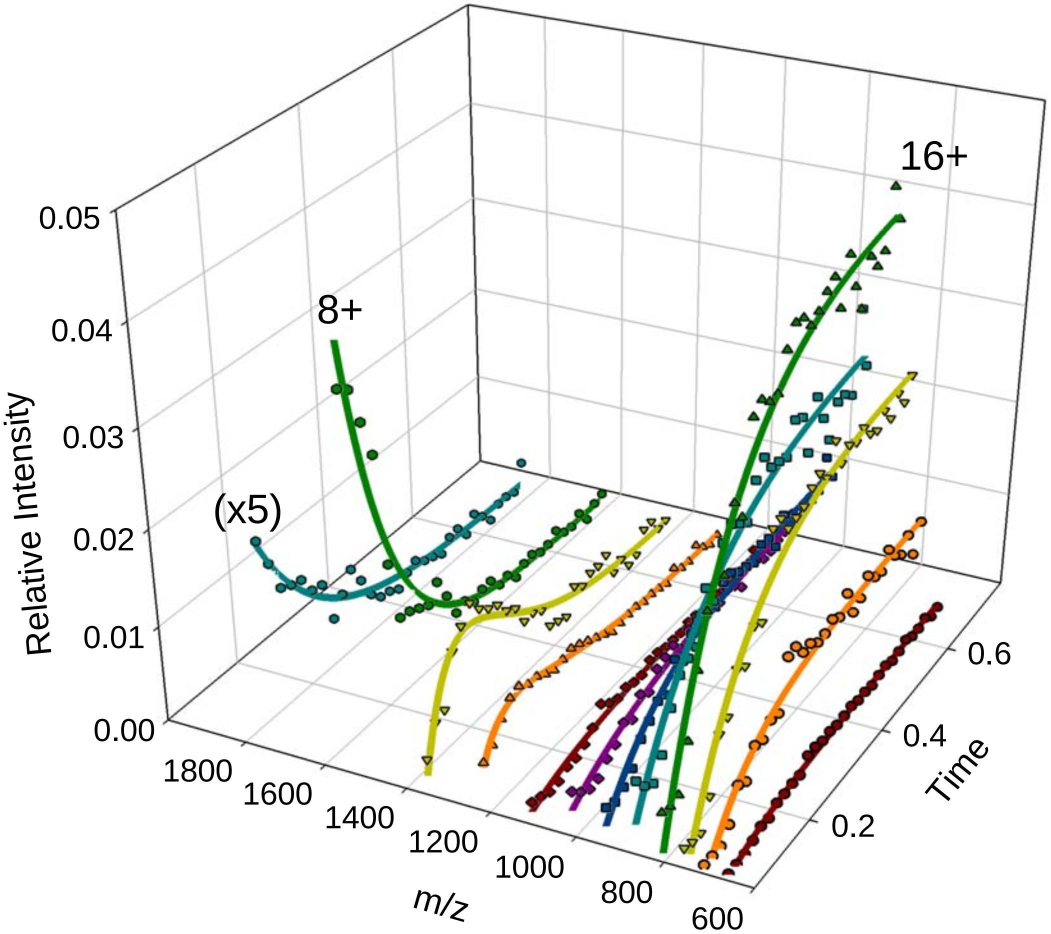

**Figure 2.6**. A global view of cytochrome *c* unfolding kinetics. Charge state 7+ intensities have been multiplied by a factor of 5 to improve visibility. Charge states which do not provide reliable kinetics due to low signal-to-noise are excluded. Solid lines represent fits to the data using expression (2.3). *P*(*a*) was calculated as described in the theory section. In keeping with a global analysis strategy described previously [35], *C*(*a*) was assumed to have the form of a linear combination of exponentials plus an offset. Satisfactory fits to all of the kinetic data were acquired using 2 exponentials with rate constants $k_{1\mathrm{obs}} = 32\ \mathrm{s}^{-1} \pm 5$ and $k_{2\mathrm{obs}} = 7.5 \pm .1\ \mathrm{s}^{-1}$.

While folding intermediates are quite common [32, 52, 64], unfolding intermediates are less commonly detected, particularly in a small proteins [35, 62]. Cytochrome *c* may be an exception due to its covalently bound heme which could act as a structural nucleus during unfolding. Alternatively, the complex unfolding landscapes predicted by some computer models [65] and observed for large proteins [35] may apply equally to small proteins. The microfluidic reactor introduced here can help to shed light on this question by facilitating the detection of transient unfolding intermediates, especially those that cannot be observed by conventional optical methods. However, the current charge state distribution-based analysis provides little information as to the nature of those intermediates. More detailed characterizations will be possible with the inclusion of additional microfluidic modules for H/D exchange pulse labeling and on-chip proteolytic digestion.

## 2.5 CONCLUSIONS

We have introduced an ESI-coupled microfluidic reactor for millisecond time-scale studies by ESI-MS. The device was fabricated using a laser ablation-based approach that is fast, inexpensive and exceedingly straightforward. The reactor compares favorably in terms of performance with a capillary mixing system introduced previously [22] and will allow the incorporation of additional microfluidic modules downstream of the reactor. In a test study, the device provided a ‘global view’ of cytochrome c unfolding that included the detection of a transient unfolding intermediate. The data were fit using an approach that compensates for the effects of laminar flow on the observed kinetics. Rates in excess of 30 $s^{-1}$ were reliably measured.

While the device introduced in the present study is suitable for a broad range of applications, there are a number of improvements that will pursued in future work. One major issue is the significant mixing time, which results primarily from the accommodation of a round capillary into a square channel. We are currently redesigning the device to incorporate square capillaries, which have recently become commercially available. Since the ‘square in a square’ geometry will also improve mixing efficiency, mixing dead-times may be reduced to below the contribution from Taylor cone volume. Additional design changes are underway to reduce Taylor cone volume and increase Taylor cone stability by using thinner substrates and optimizing the tapering method. Design improvements are being undertaken in tandem with the development of multi-module ECMDs. Applications include measuring enzyme kinetics under native salt conditions and detailed characterizations of transient species in protein folding and enzyme reactions.

In summary, the microfluidic reactor introduced here provides the capability for millisecond time-scale studies by ESI-MS on a microfluidic platform. While the device represents a powerful and versatile tool in itself, it can also be incorporated into an integrated microfluidic ‘lab on a chip’.

# REFERENCES

1. Hoffmann, P., et al., *Microfluidic glass chips with an integrated nanospray emitter for coupling to a mass spectrometer.* Angew. Chem.-Int. Edit., 2007. **46**(26): p. 4913-4916.
2. Pinto, D.M., Y.B. Ning, and D. Figeys, *An enhanced microfluidic chip coupled to an electrospray Qstar mass spectrometer for protein identification.* Electrophoresis, 2000. **21**(1): p. 181-190.
3. Zhang, B.L., F. Foret, and B.L. Karger, *High-throughput microfabricated CE/ESI-MS: Automated sampling from a microwell plate.* Anal. Chem., 2001. **73**(11): p. 2675-2681.
4. Srbek, J., et al., *Chip-based nano-LC-MS/MS identification of proteins in complex biological samples using a novel polymer microfluidic device.* J. Sep. Sci., 2007. **30**(13): p. 2046-2052.
5. Kameoka, J., et al., *An electrospray ionization source for integration with microfluidics.* Anal. Chem., 2002. **74**(22): p. 5897-5901.
6. Weibel, D.B. and G.M. Whitesides, *Applications of microfluidics in chemical biology.* Current Opinion in Chemical Biology, 2006. **10**(6): p. 584-591.
7. Lazar, I.M., J. Grym, and F. Foret, *Microfabricated devices: A new sample introduction approach to mass spectrometry.* Mass Spectrometry Reviews, 2006. **25**(4): p. 573-594.
8. Lion, N., et al., *Microfluidic systems in proteomics.* Electrophoresis, 2003. **24**(21): p. 3533-3562.
9. Erickson, D. and D.Q. Li, *Integrated microfluidic devices.* Anal. Chim. Acta, 2004. **507**(1): p. 11-26.
10. Shan, X.N., K.J. Foley, and N.J. Tao, *A label-free optical detection method for biosensors and microfluidics.* Appl. Phys. Lett., 2008. **92**(13).
11. Huang, F.C., C.S. Liao, and G.B. Lee, *An integrated microfluidic chip for DNA/RNA amplification, electrophoresis separation and on-line optical detection.* Electrophoresis, 2006. **27**(16): p. 3297-3305.
12. Mogensen, K.B., H. Klank, and J.P. Kutter, *Recent developments in detection for microfluidic systems.* Electrophoresis, 2004. **25**(21-22): p. 3498-3512.

13. Kjeang, E., et al., *Integrated electrochemical velocimetry for microfluidic devices.* Microfluidics and Nanofluidics, 2007. **3**(4): p. 403-416.

14. Hsieh, Y.C. and J.D. Zahn, *On-chip microdialysis system with flow-through sensing components.* Biosensors & Bioelectronics, 2007. **22**(11): p. 2422-2428.

15. Wu, J. and N. Islam, *Simple method to integrate in situ nano-particle focusing with cantilever detection.* Ieee Sens. J., 2007. **7**(5-6): p. 957-958.

16. Abonnenc, M., et al., *Electrospray micromixer chip for on-line derivatization and kinetic studies.* Anal. Chem., 2008. **80**(9): p. 3372-3378.

17. Koster, S. and E. Verpoorte, *A decade of microfluidic analysis coupled with electrospray mass spectrometry: An overview.* Lab Chip, 2007. **7**(11): p. 1394-1412.

18. Li, X., et al., *At-line coupling of UPLC to chip-electrospray-FTICR-MS.* Anal. Bioanal. Chem., 2007. **389**(5): p. 1439-1446.

19. Wang, Y.X., et al., *Efficient electrospray ionization from polymer microchannels using integrated hydrophobic membranes.* Lab Chip, 2004. **4**(4): p. 363-367.

20. Bedair, M.F. and R.D. Oleschuk, *Fabrication of porous polymer monoliths in polymeric microfluidic chips as an electrospray emitter for direct coupling to mass spectrometry.* Analytical Chemistry, 2006. **78**(4): p. 1130-1138.

21. Brivio, M., et al., *Chip-based on-line nanospray MS method enabling study of the kinetics of isocyanate derivatization reactions.* Anal. Chem., 2005. **77**(21): p. 6852-6856.

22. Wilson, D.J. and L. Konermann, *A Capillary Mixer with Adjustable Reaction Chamber Volume for Millisecond Time-Resolved Studies by Electrospray Mass Spectrometry.* Anal. Chem., 2003. **75**: p. 6408 - 6414.

23. Wilson, D.J. and L. Konermann, *Mechanistic Studies on Enzymatic Reactions by Electrospray Ionization MS Using a Capillary Mixer with Adjustable Reaction Chamber Volume for Time-Resolved Measurements.* Anal. Chem., 2004. **76**: p. 2537-2543.

24. Simmons, D.A., et al., *Subunit Disassembly and Unfolding Kinetics of Hemoglobin Studied by Time-Resolved Electrospray Mass Spectrometry.* Biochemistry, 2004. **43**: p. 14792 - 14801.

25. Konermann, L., B.A. Collings, and D.J. Douglas, *Cytochrome c Folding Kinetics Studied by Time-Resolved Electrospray Ionization Mass Spectrometry.* Biochemistry, 1997. **36**: p. 5554-5559.

26. David L. Zechel, L.K., Stephen G. Withers and D. J. Douglas, *Pre-Steady State Kinetic Analysis of an Enzymatic Reaction Monitored by Time-Resolved Electrospray Ionization Mass Spectrometry.* Biochemistry, 1998. **37**: p. 7664-7669.

27. Simmons, D.A. and L. Konermann, *Characterization of Transient Protein Folding Intermediates during Myoglobin Reconstitution by Time-Resolved Electrospray Mass Spectrometry with On-Line Isotopic Pulse Labeling.* Biochemistry, 2002. **41**: p. 1906-1914.

28. Kolakowski, B.M. and L. Konermann, *From small-molecule reactions to protein folding: Studying biochemical kinetics by stopped-flow electrospray mass spectrometry.* Anal. Biochem., 2001. **292**(1): p. 107-114.

29. Kolakowski, B.M., D.A. Simmons, and L. Konermann, *Stopped-flow electrospray ionization mass spectrometry: a new method for studying chemical reaction kinetics in solution.* Rapid Commun. Mass Sp., 2000. **14**(9): p. 772-776.

30. Wolf-Watz, M., et al., *Linkage Between Dynamics and Catalysis in a Thermophilic-Mesophilic Enzyme Pair.* Nat. Struct. Mol. Biol., 2004. **11**(10): p. 945-949.

31. Krishna, M.M.G., et al., *Order of steps in the cytochrome c folding pathway: Evidence for a sequential stabilization mechanism.* J. Mol. Biol., 2006. **359**(5): p. 1410-1419.

32. Raschke, T.M. and S. Marqusee, *The kinetic folding intermediate of ribonuclease H resembles the acid molted globule and partially unfolded molecules detected under native conditions.* Nat. Struct. Biol., 1997. **4**(6): p. 505-505.

33. Calamai, M., F. Chiti, and C.M. Dobson, *Amyloid fibril formation can proceed from different conformations of a partially unfolded protein.* Biophys. J., 2005. **89**(6): p. 4201-4210.

34. Chiti, F., et al., *Kinetic partitioning of protein folding and aggregation.* Nat. Struct. Biol., 2002. **9**(2): p. 137-143.

35. Wilson, D.J., S.P. Rafferty, and L. Konermann, *Kinetic Unfolding Mechanism of the Inducible Nitric Oxide Synthase Oxygenase Domain Determined by Time-Resolved Electrospray Mass Spectrometry.* Biochemistry, 2005. **44**: p. 2276-2283.

36. Pan, J., D.J. Wilson, and L. Konermann, *Pulsed Hydrogen Exchange and Electrospray Charge-State Distribution as Complementary Probes of Protein Structure in Kinetic Experiments: Implications for Ubiquitin Folding.* Biochemistry, 2005. **44**: p. 8627-8633.

37. Pan, J., et al., *Folding Kinetics of the S100A11 Protein Dimer Studied by Time-Resolved Electrospray Mass Spectrometry and Pulsed Hydrogen-Deuterium Exchange.* Biochemistry, 2006. **45**: p. 3005-3013.

38. Konermann, L., J. Pan, and D.J. Wilson, *Protein Folding Mechanisms Studied by Time-resolved Electrospray Mass Spectrometry.* Biotechniques, 2006. **40**(2): p. 134-136.

39. Ebadian, M.A. and Z.F. Dong, *Forced Convection, Internal Flow in Ducts*, in *Handbook of Heat Transfer, 3rd ed.*, W.M. Rohsenow, J.P. Hartnett, and Y.I. Cho, Editors. 1998, McGraw Hill: New York.

40. Konermann, L., *Monitoring reaction kinetics in solution by continuous-flow methods: The effects of convection and molecular diffusion under laminar flow conditions.* J. Phys. Chem. A, 1999. **103**(36): p. 7210-7216.

41. Wilson, D.J. and L. Konermann, *Ultrarapid Desalting of Protein Solutions for Electrospray Mass Spectrometry in a Microchannel Laminar Flow Device.* Anal. Chem., 2005. **77**: p. 6887-6894.

42. Schultz, G.A., et al., *A fully integrated monolithic microchip electrospray device for mass spectrometry.* Anal. Chem., 2000. **72**(17): p. 4058-4063.

43. Freire, S.L.S., H. Yang, and A.R. Wheeler, *A Practical Interface for Microfluidics and Nanoelectrospray Mass Spectrometry.* Electrophoresis, 2008. **29**(9): p. 1836 - 1843.

44. Mills, C.A., et al., *Production of structures for microfluidics using polymer imprint techniques.* Microelectron. Eng., 2005. **78-79**: p. 695-700.

45. Xia, H.M., et al., *Chaotic micromixers using two-layer crossing channels to exhibit fast mixing at low Reynolds numbers.* Lab Chip, 2005. **5**(7): p. 748-755.

46. Stone, H.A., A.D. Stroock, and A. Ajdari, *Engineering flows in small devices: Microfluidics toward a lab-on-a-chip.* Annual Review of Fluid Mechanics, 2004. **36**: p. 381-411.

47. Ottino, J.M. and S. Wiggins, *Introduction: mixing in microfluidics.* PhilosT R Soc A, 2004. **362**(1818): p. 923-935.

48. Georgievskii, Y., E.S. Medvedev, and A.A. Stuchebrukhov, *Proton transport via the membrane surface.* Biophys. J., 2002. **82**(6): p. 2833-2846.

49. Yamaguchi, Y., et al., *Interface configuration of the two layered laminar flow in a curved microchannel.* Chem. Eng. J., 2004. **101**(1-3): p. 367-372.

50. Xue, Q.F., et al., *Multichannel microchip electrospray mass spectrometry.* Anal. Chem., 1997. **69**(3): p. 426-430.
51. Kebarle, P., *A brief overview of the present status of the mechanisms involved in electrospray mass spectrometry.* J. Mass. Spectrom., 2000. **35**(7): p. 804-817.
52. Bai, Y.W., et al., *Protein-folding intermediates - Native-State Hydrogen-Exchange.* Science, 1995. **269**(5221): p. 192-197.
53. Hoang, L., et al., *Cytochrome c folding pathway: Kinetic native-state hydrogen exchange.* P. Natl. Acad. Sci. USA, 2002. **99**(19): p. 12173-12178.
54. Milne, J.S., et al., *Experimental study of the protein folding landscape: Unfolding reactions in cytochrome c.* J. Mol. Biol., 1999. **290**(3): p. 811-822.
55. Yeh, S.R., S.W. Han, and D.L. Rousseau, *Cytochrome c folding and unfolding: A biphasic mechanism.* Accounts Chem. Res., 1998. **31**(11): p. 727-736.
56. Bhuyan, A.K. and J.B. Udgaonkar, *Multiple kinetic intermediates accumulate during the unfolding of horse cytochrome c in the oxidized state.* Biochemistry, 1998. **37**(25): p. 9147-9155.
57. Winger, B.E., K.J. Lightwahl, and R.D. Smith, *Gas-Phase Proton-Transfer Reactions Involving Multiply Charged Cytochrome c Ions and Water Under Thermal Conditions.* J. Am. Soc. Mass Spectr., 1992. **3**(6): p. 624-630.
58. Konermann, L. and D.J. Douglas, *Acid-Induced Unfolding of Cytochrome c at Different Methanol Concentrations: Electrospray Ionization Mass Spectrometry Specifically Monitors Changes in the Tertiary Structure.* Biochemistry, 1997. **35**: p. 12296-12302.
59. Konermann, L. and D.J. Douglas, *Equilibrium Unfolding of Proteins Monitored by Electrospray Ionization Mass Spectrometry: Distinguishing Two-state from Multi-state Transitions.* Rapid Commun. Mass Sp., 1998. **12**: p. 435-442.
60. Shi, X.G., et al., *Thermal unfolding of proteins probed by laser spray mass spectrometry.* Rapid Commun. Mass Sp., 2008. **22**(9): p. 1430-1436.
61. Winkler, J.R., *Cytochrome c folding dynamics.* Curr. Opin. Struct. Biol., 2004. **8**(2): p. 169-174.
62. Juneja, J. and J.B. Udgaonkar, *Characterization of the unfolding of ribonuclease a by a pulsed hydrogen exchange study: Evidence for competing pathways for unfolding.* Biochemistry, 2002. **41**(8): p. 2641-2654.

63. Ramdas, L. and B.T. Nall, *Folding and Unfolding Kinteics of Mutant Forms of Iso-1-Cytochrome c With Replacement of Proline-71.* Biochemistry, 1986. **25**(22): p. 6959-6964.

64. Englander, S.W., *Protein folding intermediates and pathways studied by hydrogen exchange.* Annu. Rev. Biophys. Biomol. Struct., 2000. **29**: p. 213-238.

65. Lazaridis, T. and M. Karplus, *"New view" of protein folding reconciled with the old through multiple unfolding simulations.* Science, 1997. **278**(5345): p. 1928-1931.

# CHAPTER 3

## Measuring Dynamics in Weakly Structured Regions of Proteins Using Microfluidics-Enabled Sub-second H/D Exchange Mass Spectrometry

***Adapted from*** *Anal. Chem., 84 (8), 3771-3779*

## 3.1 INTRODUCTION

The tools of structural biology (*i.e.*, X-ray crystallography and structural NMR) provide an exquisitely detailed, but largely static view of the physiologically relevant, 'native' structures of proteins [1, 2]. The importance of these structures to understanding how proteins carry out their biological roles cannot be overstated, and yet if proteins were to adopt *only* the structures reported, many would be essentially non-functional [3]. Virtually all aspects of protein activity, from catalysis to ligand binding and allostery depend on the ability to transiently adopt specific higher energy structures [4-8]. These 'excited states' are critical to function, and can in some cases act as a gateway to misfolding and disease [9-12]. Thus, there is substantial motivation to understand not only the 'ensemble averaged' structures revealed by classical structural biology, but also to characterize the transient, weakly populated structures that are adopted via conformational dynamics.

Excited protein states are challenging analytical targets because they are **i)** transient, **ii)** weakly populated at equilibrium and **iii)** spectroscopically similar to the ground-state. In the early 1980's, backbone amide HDX was introduced as a means of measuring the integrity of hydrogen bonding networks in protein secondary structures, first by NMR [13] and later by mass spectrometry [14]. This approach is founded on the premise that solvent accessible backbone amide protons are protected from exchange with solvent if they are hydrogen bonded (as they are in secondary structures). The degree of protection reflects the strength of the hydrogen bond, and, averaging over adjacent amides, the stability of the secondary structure in question [15].

In NMR experiments, HDX is usually measured as a time-dependent decrease in the volume of backbone amide proton HSQC cross-peaks [13]. NMR measurements are always site specific, but transverse relaxation limits conventional solution NMR experiments to proteins < ~50 kDa, and acquisitions are typically on the minutes time scale, which severely limits the ability to monitor more dynamic regions [16]. In MS-based HDX experiments, exchange is monitored *via* the mass increase accompanying deuterium uptake. This approach is more amenable to time-resolved measurements and need not be size limited, but usually provides 'segment averaged' HDX data [17].

MS-based HDX methods can be divided into 'top-down' and 'bottom-up' approaches. Top-down experiments involve fragmentation of deuterium-labeled protein ions in the gas phase (*i.e.* post-ionization) [18]. Top down experiments can yield single-residue resolution, but the electron capture/transfer fragmentation methods that are used (to avoid 'scrambling') [19-21] require more specialized equipment and impose an effective size limit [5] due in part to decreasing fragmentation efficiency with increasing size. The 'bottom-up' approach involves quenching of the HDX reaction by acidification, followed by proteolytic digestion using an acid-resistant protease [14]. In this case, spatial resolution is a function of digestion efficiency and typically ranges from 4 to 10 residues [22]. Thus, bottom-up HDX experiments yield 'segment averaged' data which are semi-quantitative. The advantage of the bottom-up approach is that it is broadly applicable; there is no inherent size limit and it can be carried out using widely available, non-specialized instrumentation.

One of the challenges of implementing bottom-up HDX is the occurrence of back-exchange during the proteolytic and LC steps, which are carried out in $H_2O$. Back-exchange not only dampens the structural information acquired during forward-labeling, it also does so in a site-specific manner that is governed more-or-less exclusively by the primary sequence (in contrast to the forward-exchange step, which is also structure dependent) [23]. Thus, significant back-exchange can lead to an artifactual deuteration 'profile' that is more reflective of the intrinsic back-exchange rates than conformational dynamics. Back-exchange can usually be kept to manageable levels by lowering the solvent pH to ~2.5 and the temperature to 0˚C, but sacrifices to digestion and/or separation efficiency are frequently made to avoid lengthy on-column times [24].

In a typical backbone-amide HDX experiment, exchange is measured over a period of minutes-to-hours [22, 25, 26]. This timescale is appropriate for structured region of the protein because, while dynamics and the accompanying fluctuations between a hydrogen bonded 'closed' state and an unbonded 'open' state may be rapid, the equilibrium $K_{\mathrm{op}}$ will strongly favor the 'closed' state, greatly slowing the observed rate of exchange. In more dynamic regions such as loops and weak secondary structures, however, conventional HDX measurements yield only a ‘burst-phase’ of exchange which, especially in loops, is commonly 100%. This limitation is unfortunate given the critical role that dynamic regions often play in protein function, and the biological importance of ‘intrinsically disordered’ proteins, which are largely dynamic in their native state.

In this work, we introduce a microfluidic device that enables time-resolved (*i.e.*, millisecond time-scale) MS-based HDX measurements, integrating all of the necessary components for a bottom-up workflow with on-line ESI. This approach provides a powerful alternative to quench-flow experiments [27, 28], which are limited by decoupled sample handling and analysis and CLEANEX NMR [29, 30], which shares size and time-scale restrictions with other NMR methods. Residence times in the device are small relative to other techniques, ensuring minimal back-exchange (≤ 5%) without the necessity for cooling. Our present aim is to characterize device performance and to illustrate the utility of time-resolved HDX experiments. Three model systems are investigated including a single time-point structural analysis of ubiquitin, a comparison of loop dynamics in cytochrome c and a localization of conformational flexibility in the substrate-free form of a large tetrameric enzyme, DAHP synthase.

## 3.2 EXPERIMENTAL

**3.2.1 Materials**. Horse heart cytochrome c, ubiquitin, pepsin, deuterium oxide ($D_2O$), ammonium hydroxide, ammonium acetate (99.8%), 2-propanol (70% in water) and high purity acetic acid (≥ 99.7%) were purchased from Sigma (St. Louis, MO). Polyimide coated glass capillaries (O.D. 153 μm, I.D. 75 μm) were supplied by Polymicro Technologies (Pheonix, AZ). Metal capillaries (O.D. 400 μm, I.D. 200 μm and O.D. 318 μm, I.D. 158.75 μm) were purchased from Small Parts, Inc. (Miramar, FL). PTFE tubings (O.D. 1/16″, I.D. 400 μm and O.D. 1/16″, I.D. 205 μm) were supplied by McMaster Plastics (Scarborough, ON). Standard 1/16″ fittings were purchased from Upchurch (Oak Harbor, WA). Ultrapure water was generated in-house on a Millipore Milli-Q Advantage A10 system. The rotary grinder (Craftsman Co. Hoffman Estates, IL) was used to sharpen the metal capillary.

**3.2.2 Microfluidic Device Fabrication**. The multistep microreactor is an integration of a rapid mixing module [31] and a rapid proteolysis module [32] that were developed earlier. The device was fabricated on blank poly(methyl methacrylate) or PMMA substrate which was purchased from Professional Plastics (Fullerton, CA) in rectangular block with dimension of 8.9 cm x 3.8 cm x 0.3 cm. The microfluidic channels and well (32 mm x 5 mm x 0.01 mm) were etched on PMMA using a LASER engraver (Universal Laser, Scottsdale,AZ) following the protocol described by Rob *et al*. [31]. The concentric capillary mixer was incorporated in the central channel of the device using a soldering iron. Two additional metal capillaries were similarly incorporated into adjacent channels to support connections to infusion pumps (Harvard, Holliston, MA) using standard Upchurch fittings. A closed polyimide-coated glass capillary was used as a static mixer to ensure efficient mixing of acid and deuterated protein before the quenched solution was transferred to proteolytic module. Pepsin was covalently attached to the floor and ceiling of the reactor well using protocol described by Brown *et al.* [33] Parafilm® was used as gasket to obtain liquid-tight seal between the two activated PMMA blocks. A custom built clamp was obtained from LAC Machine & Tooling Limited, ON to pressure-seal the microfluidic device [32].

**3.2.3 DAHP synthase (Phe) purification.** *Escherichia coli* Phe-regulated DAHP synthase (aroG) was produced in *E.coli* BL21*(DE3) cells harboring a pET300/*aroG* plasmid which contained *aroG* with an *N*-terminal TEV-protease-cleavable $His_6$-tag. Transformed BL21*(DE3) *E. coli* cells were grown at 37 °C in 1 L of LB broth with 100 μg/mL of ampicillin to $OD_{600}$ = 0.6. DAHP synthase expression was induced with 0.3 mM isopropyl β-D-1-thiogalactopyranoside (IPTG) at 37 °C for 4 h. Cells were harvested by centrifugation at 8000 × g for 20 min, resuspended in 15 mL of buffer A (50 mM Tris-HCl, pH 7.5, 150 mM NaCl, 50 mM imidazole, 1 mM phenylmethylsulfonyl fluoride). All subsequent steps were carried out at 4 °C. Cells were lysed by passage through EmulsiFlex-C5 High Pressure Homogenizer at 10,000 psi. Cell debris was removed by centrifugation for 30 min at 10,000 × g. DAHP synthase was purified by nickel affinity chromatography on a $Ni^{++}$-charged 1 mL HiTrap chelating Sepharose (GE Healthcare) column. DAHP synthase was eluted with buffer B (50 mM Tris-HCl, pH 7.5, 150 mM NaCl, 500 mM imidazole). No other bands were visible by SDS/PAGE electrophoresis. The *N*-terminal $His_6$-tag was removed by treating purified DAHP synthase overnight at 4 °C with $His_6$-tagged TEV protease (plasmid provided by Dr. Murray Junop, McMaster University) in 1:4 (TEV:DAHPS) molar ratio, along with 1 mM EDTA, 1 mM dithiothreitol and 10% (v/v) glycerol. The reaction mixture was buffer exchanged into 20 mM Tris-HCl, pH 7.5 and run through a $Ni^{++}$-charged chelating Sepharose column, as above, to remove the cleaved *N*-terminal tag, uncleaved $Hig_6$-tagged DAHP synthase and $His_6$-tagged TEV protease. Pure DAHP synthase was dialyzed into 10 mM ammonium acetate, pH 7.6.

**3.2.4 H/D Exchange Measurements**. HDX studies were carried out with ubiquitin, cytochrome c and DAHP synthase using the integrated microfluidic chip as a custom electrospray ionization (ESI) source (Figure 3.1). The chip was directly interfaced with a modified QSTAR® Elite hybrid quadrupole time-of-flight (QqTOF) mass spectrometer (Sciex, MDS Analytical Technologies, Concord, ON). 50 μM ubiquitin, 500 μM cytochrome c and 270 μM DAHP synthase were mixed with $D_2O$ (1:3) in the rapid mixing module of the device (pD 7.6). The position of the mixer in the mixing module was adjusted manually to control the labeling time.

Using flow rates of 1μL/min for protein solution and 3 μL/min for $D_2O$ we were able to achieve labeling times from 42 ms to 10 sec. Labeling was rapidly quenched by dropping the solution to pH 2.6 by using a 4% acetic acid solution (pH 2.3) at 9 μL/min (2 x 4.5 μL/min). Digestion and electrospray was therefore ultimately carried out in a 77:23 $H_2O/D_2O$ mixture. Digestion of deuterated proteins and transfer to the ESI emitter was carried out in approximately **7** s to minimize the back-exchange of backbone amides (protons on side chain and termini were assumed to be fully equilibrated with the electrosprayed solution prior to ionization). Peptide exchange levels were modeled using a custom built FORTRAN program, based on an analytical framework described previously [19], with 'offset' adjustments for backbone amide back-exchange determined using the neuropeptide bradykinin as an internal standard, always ≤ 5%) and equilibrated exchange at side-chains and termini.

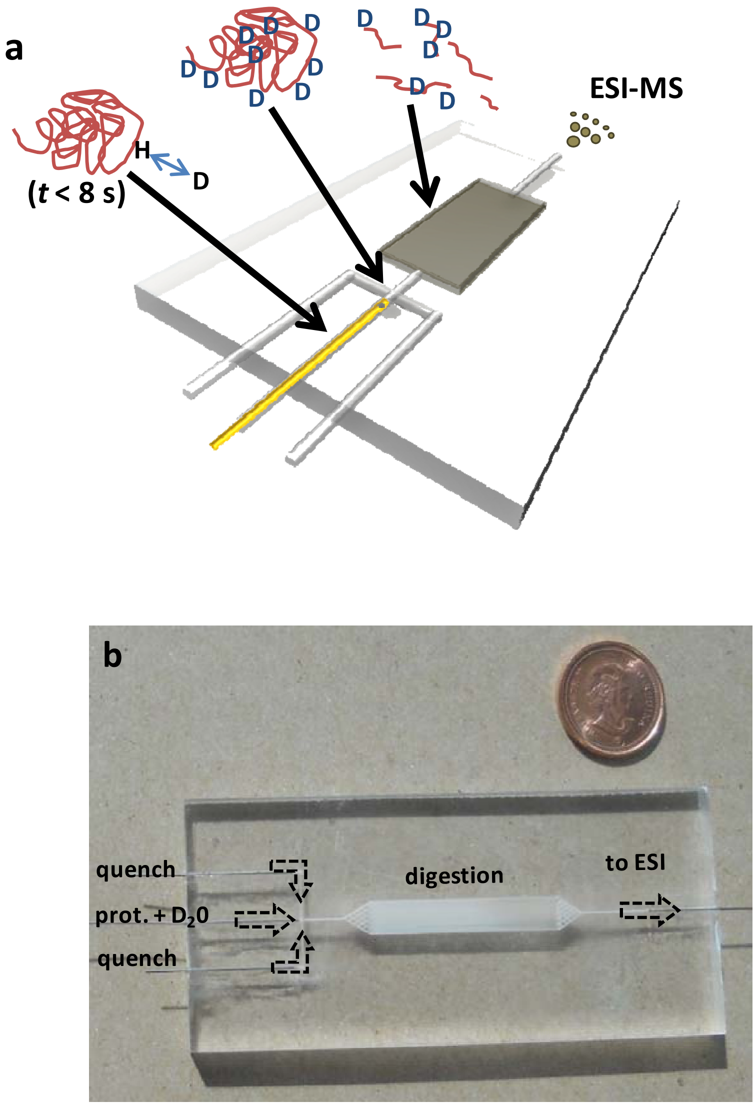

**Figure 3.1**. The microfluidic device. (a) A schematic depiction. Solutions are injected at the ‘near’ side of the device and ESI is carried out at the ‘far’ end. HDX is conducted under ‘native’ conditions (pD 7.6) in the first phase with adjustable labeling times from ~ 40 ms to 8 s. This is followed by HDX quenching, which is achieved by dropping the pH to 2.5. The labeled protein is then injected into the proteolytic reactor, generating labeled peptides which can be located on the native structure. (b) A photograph of the device, with coin for scale.

**3.2.5 Data Analysis Method**. Under native conditions, the hydrogen bonding and/or solvent accessibility characteristics of most backbone amides are such that the 'closing' rate for a given amide $k_{\mathrm{cl}}$ is usually much greater than the intrinsic rate at which HDX would occur with a completely 'open' configuration $k_{\mathrm{int}}$. In this regime, called the EX2 limit, the observed rate of exchange $k_{\mathrm{ex}}$ $k_{\mathrm{ex}}$ is a function of the 'opening' rate $k_{\mathrm{op}}$, $k_{\mathrm{int}}$ and $k_{\mathrm{cl}}$ in the following relationship.

$$k_{ex} = \frac{k_{op}}{k_{cl}} k_{int} = K_{op} k_{int} \tag{3.1}$$

The intrinsic rate is dependent on primary sequence and, thanks to a substantial effort by Bai and co-workers [34], intrinsic rates for any sequence can be calculated to within a good approximation based on experimental parameters [35]. Thus, for any particular backbone-amide, it is possible to determine the 'open'/'closed' equilibrium represented by $K_{\mathrm{op}}$ simply by dividing out $k_{\mathrm{int}}$. This value ($k_{\mathrm{ex}}/k_{\mathrm{int}}$) can be interpreted as a quantitative measure of the local thermodynamic stability of secondary structural elements [36], but is more often inverted and described in more qualitative terms as a protection factor (PF) [37].

While it is relatively easy to interpret the physical meaning of a single backbone amide proton's PF value, the acquisition of 'segment averaged' HDX data presents a problem in that the observed increase in deuteration per unit time D($t$) is a function of multiple $k_{\mathrm{ex}}$

$$D(t) = \sum_{i=2}^{m} \left(1 - e^{-\left(K_{op}^{(i)} \times k_{int}^{(i)}\right)t}\right) \tag{3.2}$$

where $m$ is the number of backbone amides in the segment, $K_{op}^{(i)}$ is the 'open'/'closed' equilibrium constant at residue $i$ and $k_{int}^{(i)}$ is the intrinsic rate constant for residue $i$. The bracketed terms in the exponent could be combined into $k_{ex}$, but here they are kept separate for discussion below. In conventional experiments where there is a lengthy LC step, the index would start at $i = 3$ due to rapid back-exchange at the $i = 2$ position and 'instantaneous' equilibration of exchange at the $i = 1$ position during enzymatic hydrolysis of the peptide bond. In our setup, however, post-quench residence times are sufficiently small that back-exchange at the $i = 2$ amide is predicted to $\leq 10\%$ in all cases. We therefore start our index at $i = 2$.

The challenge in analyzing 'segment averaged' data is that, since $K_{op}$ may be different for each amide, the system is underdetermined and cannot be analyzed quantitatively. However, a semi-quantitative approach can provide reliable 'average' protection factors in many cases. There is some debate about the best expression to use when fitting 'segment averaged' D($t$) profiles. The 'ideal' multiexponential with $m$-1 terms shown in Equation 3.2 would have too many variable parameters to provide meaningful individual rates for segments with more than two 'exchange active' amides. Thus, 'segment averaged' data are usually fitted using an unmodified single or double-exponential expression [22]. In the event that the $k_{ex}$ within the peptide are not widely dispersed, a single exponential fit will provide a good approximation of the average $k_{ex}$. If there are two distinct populations of $k_{ex}$ values within the peptide (*e.g.*, if the peptide includes both a structured region and a loop), and the values within each population are not widely dispersed, then a double exponential fit will provide a good estimate of the average $k_{ex}$ within each population.

Since our measurements are conducted after only a maximum of a few seconds of $D_2O$ exposure, the observed HDX kinetics are dominated by backbone amides with $K_{op}$ in the range of approximately 0.01 to 1, which occurs in weakly structured regions. In structured regions, $K_{op}$ values typically range from $1 \times 10^{-3}$ to $1 \times 10^{-5}$. Exchange at these slow exchanging amides is in a pre-equilibrium steady-state on the time-scale of our measurements, thus their (usually very minor) contribution to the observed kinetics can be approximated as linear. We therefore use the following expression to fit our D($t$) profiles

$$D(t) = N_{fast}(1 - e^{-k_{ex}t}) + N_{slow}k_{slow}t \qquad (3.3)$$

where $N_{fast}$ is the number of amides that undergo significant exchange on the time-scale of our experiments, $k_{ex}$ is the average observed exchange rate for the 'fast' exchangers, $N_{slow}$ is the number of amides involved in the slow exchange process and $k_{slow}$ is the average HDX rate for 'slow' exchangers. Note that, although $N_{slow}$ and $k_{slow}$ are separable (by subtracting $N_{fast}$ from the total number of amides in the peptide), we cannot obtain good estimates of $k_{slow}$ from data taken on this timescale. We include the term only to achieve a more accurate determination of $k_{ex}$.

In order to simplify comparisons for the reader, we report D($t$) in units of '% exchanged' which normalizes the data to the number of exchangeable backbone amides ($m$ - 1) and accounts for the labeling offsets caused by the labeling solution (in our experiments, exchange was conducted in 80% $D_2O$) , back-exchange and equilibrated exchange at side-chains and termini (our electrosprayed solution contains 23% $D_2O$, thus exchangeable side-chains and termini will be 23% labeled from $t = 0$). We were able to achieve good fits to all of our data using Equation 3.3, in spite of the fact that it assumes a wide separation between $k_{ex}$ and $k_{slow}$ which may not occur in all peptides. Most importantly, fits to Equation 3.3 should provide the most accurate estimate of $k_{ex}$ (the term corresponding to conformational flexibility in dynamic regions) from our short labeling-time HDX measurements.

With amides in secondary structures not contributing significantly to the observed exchange, it is often possible to attribute $D(t)$ specifically to loop amides by comparing $N_{\mathrm{fast}}$ to the predicted number of loop amides $N_{\mathrm{loop}}$ from an X-ray or NMR structure. For example, if a peptide is 70% helix and 30% loop in the appropriate structure, then $N_{\mathrm{fast}}$ should be roughly 30%. This is a rough estimate because it is often difficult to define precisely the starting point of a secondary structure in terms of hydrogen bonding, for example at the N-termini of $\alpha$-helices (where the 'initial' 4 amides may or may not be hydrogen bonded). Another assumption is that the available X-ray or NMR structure reflects exactly what is present in solution, which is not always the case. With cytochrome c, for example, we found generally good agreement between $N_{\mathrm{fast}}$ and $N_{\mathrm{loop}}$, with a few exceptions (corresponding to 'rigid' loops) where $N_{\mathrm{fast}}$ was significantly lower. In the case of DAHP, however, the available structure corresponds to the substrate-bound form of the enzyme while we were monitoring the free protein. As it turns out, these structures are substantially different, resulting in essentially no correlation between $N_{\mathrm{fast}}$ and $N_{\mathrm{loop}}$ predicted from the available structure (with a few important exceptions at the tetramer interface, see discussion).

Where there is good agreement between $N_{\mathrm{fast}}$ and $N_{\mathrm{loop}}$, we can construct a 'loop amide only' intrinsic rate multiexponential, $D(t)_{\mathrm{int}}$, which we use to generate 'segment averaged' PFs specifically reflecting loop dynamics. In the event that $N_{\mathrm{fast}}$ is substantially smaller than the expected number of loop amides, we can provide a PF estimate based on the average intrinsic rate for *all* loop amides (even though only a subset are undergoing exchange on our time-scale) and a lower and upper bound, determined by taking the average of the $N_{\mathrm{fast}}$ number of lowest and highest intrinsic rates, respectively. Values of $N_{\mathrm{fast}}$ that are substantially higher than $N_{\mathrm{loop}}$ suggest that the X-ray or NMR structure being used to define the loop does not reflect the sample in solution. In this case, we can make no assumptions about which amides are contributing to the observed exchange, and the PF is calculated using the average of all intrinsic rates from the segment.

Therefore our time-resolved HDX data differ from those collected in conventional experiments in that the time-scale is sufficiently short that we expect essentially no contribution from amides in secondary structures. In cases where we can define the position of loop amides based on a reported X-ray or NMR structure, we compare the amplitude of the observed exchange $N_{\text{fast}}$ to the number of loop backbone amides $N_{\text{loop}}$. If $N_{\text{fast}}$ and $N_{\text{loop}}$ are in reasonable agreement in a given segment, then it is likely that the reported structure reflects the solution conformation under our conditions, and we attribute the observed exchange specifically to loop amides. The condition $N_{\text{fast}} << N_{\text{loop}}$ suggests that the loop reported in the structure is extensively hydrogen bonded and may include unreported secondary structure. Conversely, when $N_{\text{fast}} >> N_{\text{loop}}$, this would indicate that a reported secondary structure element is weakly populated (or possibly not even present) under our conditions. The observed HDX kinetics profiles are fit to a modified single exponential expression as described earlier. From this fit, we extract the segment averaged rate of exchange $k_{\text{ex}}$. Protection factors (PFs) are defined as $k_{\text{int}}/k_{\text{ex}}$ where $k_{\text{int}}$ is the average intrinsic rate of exchange for the segment. If $N_{\text{fast}} \approx N_{\text{loop}}$, the average intrinsic rate $k_{\text{int}}$ is calculated specifically from loop amides.

## 3.3 RESULTS AND DISCUSSIONS

**3.3.1 Microfluidics.** The integrated microfluidic device for time-resolved HDX experiments is shown in Figure 3.1. PMMA was selected as the substrate to allow straightforward fabrication *via* laser ablation [31], however, this introduced a risk of sample contamination due to dissolution of PMMA, particularly in the acid quench solution channel. Fortunately, blank control experiments showed no signs of PMMA degradation, which we have observed previously as the appearance of a polydisperse PMMA polymer signal in the range of 300- 1500 *m/z* . In earlier iterations of our proteolytic reactor, we used pepsin-agarose beads which were attached to the floor of the reactor well *via* adhesion [32, 38]. The activity of these reactors was sufficient, but the continuous-use lifetime was limited to *ca*. 8 h. In this study, we used a covalent attachment protocol developed by Brown and co-workers [33, 39] which decreased digestion efficiency slightly, but improved the continuous-use lifetime to more than 56 h.

To facilitate HDX experiments, our primary design objective was to maintain efficient protein digestion while minimizing back exchange which, in practice, meant optimizing the geometry of the proteolytic reactor well. We found ultimately that a well with dimensions length = 32 mm, width = 5 mm and depth = 10 μm (vol. = 1.6 μL) provided sufficient digestion while keeping back-exchange sufficiently low as to have a negligible impact on the data [40]. While always below 5%, back exchange was highly variable run-to-run, suggesting that it may have been arisen from ESI source conditions (back-exchange was monitored using a peptide with known exchange characteristics, bradykinin, as an internal standard) [40]. At the flow rates used, the reactor well and transfer volumes corresponds to a total post-quench residence time of approximately 8 s prior to ESI. An analysis of the dependence of sequence coverage and peptide length on geometry is provided in Table 3.1. Using the geometry given above, and activating both on the 'floor' and the 'ceiling' of the reactor, sequence coverage was 85% for ubiquitin, 60% for cytochrome c and 60% for DAHP synthase with an average peptide length of 5 a.a. (ubiquitin), 9 a.a. (cytochrome c) and 6 a.a. (DAHP synthase). These statistics translate into sufficient spatial resolution to provide meaningful measurements of local conformational dynamics, but as always in bottom up experiments, enhancement of digestion efficiency (without increasing residence times) is an avenue for further development.

**Table 3.1: Effect of well design on sequence coverage and average peptide length in cytochrome c.**

| Well geometry | Well dimension ( mm x mm x mm) | Well volume (μL) | Sequence coverage (%) | Average Peptide length |
|---|---|---|---|---|
| Square | 2 x 2 x 0.01 | 0.04 | 50 | 25 |
| Square | 3 x 3 x 0.01 | 0.09 | 53 | 23 |
| Square | 4 x 4 x 0.01 | 0.16 | 55 | 20 |
| Rectangle | 8 x 2 x 0.01 | 0.16 | 55 | 18 |
| Rectangle | 16 x 5 x 0.01 | 0.8 | 60 | 16 |
| Rectangle | 32 x 5 x 0.01 | 1.6 | 60 | 14 |
| Rectangle | 32 x 20 x 0.01 | 6.4 | 62 | 12* |
| Rectangle | 32 x 5 x 0.01** | 1.6 | 60 | 9 |

* This geometry provided the best sequence coverage, but the additional dead-time resulted in substantially more back exchange (approximately 20%)

** This well design, which was ultimately selected, was activated both on the 'floor' and 'ceiling'.

The adjustable capillary mixing component, which is adapted from a mixer introduced by Wilson and Konermann [41] allowed HDX labeling times between roughly 40 ms and 8 s. We used the mixer in static mode, meaning that the mixer is held at a fixed position to allow for indefinite time acquisitions at a single reaction time-point. This was mainly to allow for complete flushing of old material from the proteolytic reactor prior to the initiation of measurements at a new time increment. We found that flushing for 5 minutes after adjusting the capillary position to the new time-point was sufficient to prevent carryover of old material, based on stabilization of the exchange level for all peptides.

**3.3.2 Single Time-point Structural Measurements**. One of the most straightforward applications of spatially resolved HDX measurements is a crude (but high throughput) structural analysis based on a single time-point measurement [5, 42]. These experiments rely on the substantial difference between $K_{\mathrm{op}}$ in structured and unstructured regions to determine the locations of secondary structures. The approach is feasible because $k_{\mathrm{int}}$ is distributed over a much narrower range (around 2 orders of magnitude) than $K_{\mathrm{op}}$; thus amides with high intrinsic rates in structured regions will still exchange much more slowly than amides with low intrinsic rates in unstructured regions. A single time-point spatially-resolved HDX profile should therefore reflect the locations of secondary structure elements (and to a lesser extent, solvent accessibility) [22]. As labeling time increases, however, amides with progressively lower $K_{\mathrm{op}}$ begin to acquire a significant amount of label and the 'secondary structure map' begins to blur. Thus, the optimal labeling time is one that is sufficiently long to minimize contributions from the segment averaged $k_{\mathrm{int}}$ and sufficiently short to maximize the contrast between structured and unstructured regions. At physiological pH, this would correspond to a sub-second labeling time on the order of 100 ms.

To demonstrate the acquisition of a secondary structure map using our apparatus, we have acquired a single time-point (100 ms) HDX profile for ubiquitin (Figure 3.2). In general, the profile agrees with the known structure of ubiquitin, with $\alpha$-helices and $\beta$-strands exhibiting a substantially lower deuterium uptake than loops. One interesting feature is that even the most highly labeled loops underwent only 50% of their potential deuterium uptake, whereas, based on $k_{\text{int}}$ alone, most should be essentially 100% labeled. This would suggest that amides located in loops still have substantial attenuation of $k_{\text{int}}$ by $K_{\text{op}}$, a finding that is corroborated by NMR CLEANEX measurements which typically show loop $K_{\text{op}}$ values between 1 and 0.1 [30]. There was also low-level labeling (up to 20%) in regions of secondary structure. This can be attributed somewhat to averaging of exchange levels in overlapping segments, but mostly it results from the fact that not all amides in secondary structure elements are hydrogen bonded (*e.g.* the N-termini of α-helices and the outward-facing side of edge *β*-strands).

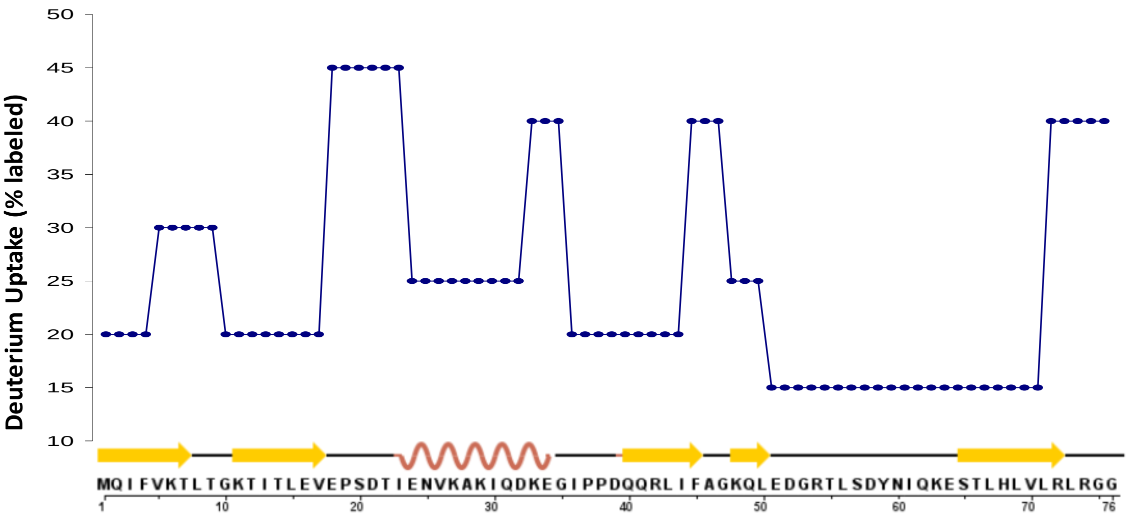

**Figure 3.2**. A crude secondary structure analysis of Ubiquitin using a single, sub-second HDX time-point (100 ms). The y-axis corresponds to deuterium uptake in '% deuterated' while the x-axis represents the primary sequence from the N-terminus on the left. Exchange levels of overlapping peptides are averaged, and the small 'uncovered' regions are assumed to be an average of the two flanking exchange levels.

There are some regions where the profile is not as expected, most notably the large loop preceding the C-terminal β-strand (the β4 - β5 loop) where low HDX uptake suggests substantially more protection than would be expected in a loop. In fact, this observation is supported by NMR-based measurements including extended timescale order parameters which indicate a relatively low degree of conformational flexibility in this loop on the μs timescale [43]. NMR HDX measurements also show an intermediate degree of protection (*i.e.* substantially more than a typical loop, but less than a secondary structure) in this region [44]. The X-ray structure (PDB code 1UBQ) [45] suggests that this increased protection may stem from extensive hydrogen bonding of β4 - β5 loop amides with residues in the N-terminus of α1-helix and the β5-strand.

Taken together, our ubiquitin data illustrate both the advantages and disadvantages of using ms timescale deuterium pulses for secondary structure profiles. The contrast between secondary structures and loops (where they are detected) is very high, but the short labeling time results in an over-sensitivity to intermediate degrees of protection (*e.g.*, in the β4 - β5 loop) which can lead to 'false positives' for secondary structure. On the other hand, these single time-point 'false positives' hint at the primary advantage of short labeling time HDX kinetics, namely the ability to distinguish very low protection from low - moderate protection in weakly structured regions.

**3.3.3 Characterizing Conformational Dynamics in Weakly Structured Regions**. We used loop dynamics in native cytochrome c to illustrate the ability to characterize dynamics in weakly structured regions at physiological pH. Cytochrome c is not an ideal candidate for our approach in that it is a poor substrate for pepsin [46], however, its native state conformational dynamics have been extensively characterized, providing the best option for a methodological comparison [47, 48]. Sequence coverage was 60% overall, with 100% coverage in the C-terminal half of the protein but no peptides detected from the N-terminal region. Some of this lack of coverage at the N-terminus may stem from the presence of covalently bound heme (Cys 14 and Cys 17), which would likely have had a deleterious effect on pepsin activity.

To accurately characterize conformational dynamics, it is necessary to monitor deuterium uptake as a function of time, *i.e.*, HDX kinetics. Typical raw data that contribute to the kinetic profiles for 3 peptides are shown in Figure 3.3 .The '% exchanged' value for each time-point is determined by fitting the observed isotopic distribution to a theoretical one generated using a custom FORTRAN program (black circles) with adjustment to account for various labeling offsets caused by the composition of the exchange solution and equilibrated HDX on side-chains and termini (see data analysis section). We observe a continuous mass increase as a function of time indicating that exchange is in the EX2 regime, which is typical under native conditions.

To analyze the HDX kinetics, we plot '% exchanged' *vs*. time (Figure 3.4), which corresponds to $D(t)$ as discussed in the data analysis section. HDX kinetics plots for 9 representative cytochrome c peptides together with the 'loop localized' intrinsic rate profiles $D(t)_{\text{int}}$. The observed profiles are colored by PF from blue (high protection) to red (very low protection). A graphical summary of the cytochrome c results (Figure 3.5) shows the observed peptides mapped onto the solution structure of horse heart cytochrome c (PDB code 1AKK) [49] and colored according to the PF from blue (high protection) to red (very low protection). These

PFs are derived exclusively from short labeling pulse HDX measurements, corresponding to exchange processes that are essentially complete after 4.5 s.

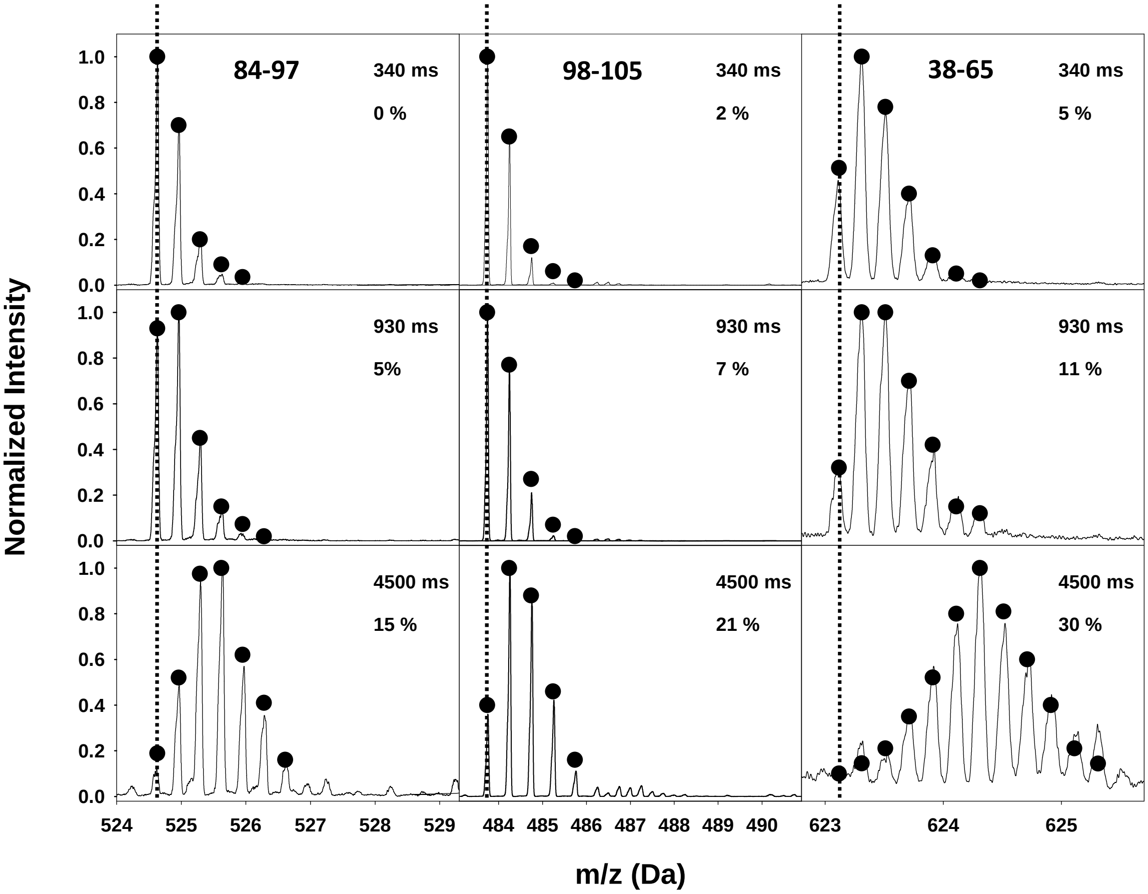

**Figure 3.3**. Raw data for HDX kinetics in three representative cytochrome c peptides. The '% exchanged' values were determined by fitting the observed isotopic distribution to a theoretical one (black circles) generated from a FORTRAN program developed in-house. Adjustments were made to account for equilibrated exchange on side chains and termini due to the composition of the final electrosprayed solution.

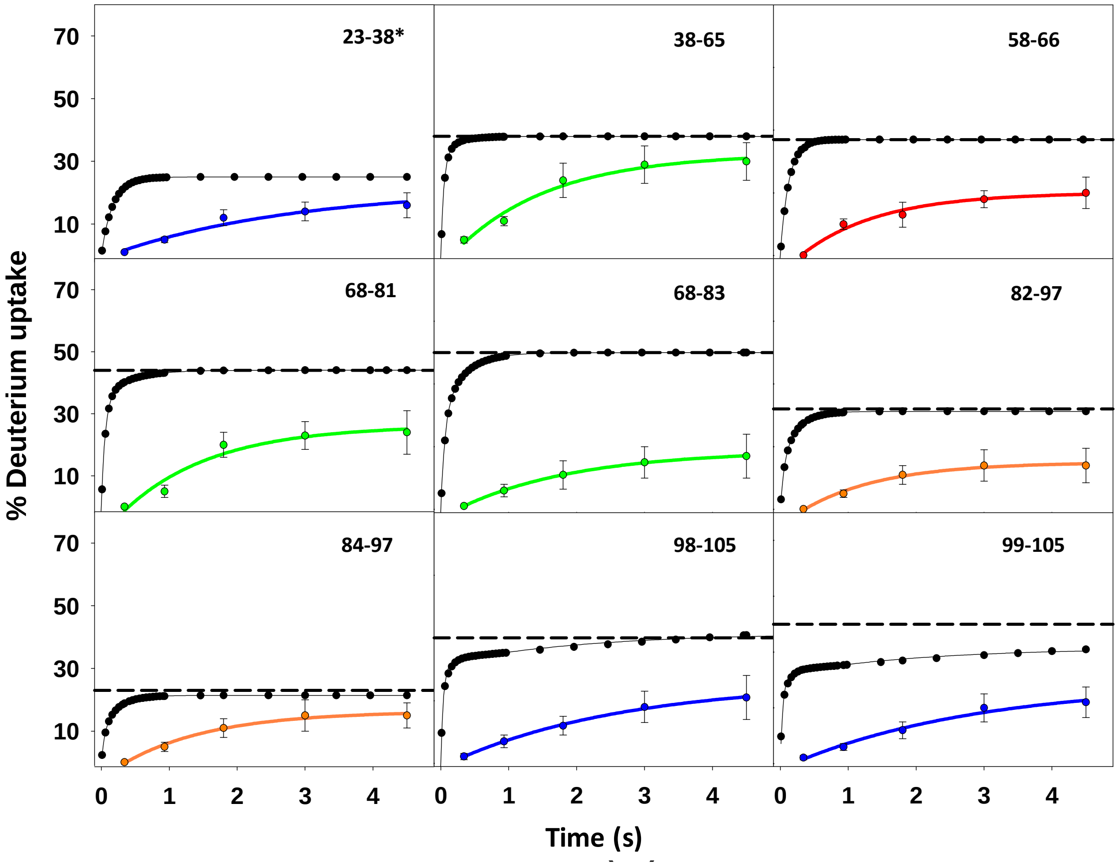

**Figure 3.4.** Representative kinetic plots of '% exchanged' *vs.* time for 9 peptides from cytochrome c. The 'loop amide only' profiles based on the intrinsic rates $D(t)_{int}$ are shown in black. The dashed line represents 100% exchange of loop amides (*i.e.* $N_{loop}$). The measured profiles are colored by PF; blue (strong protection), green (moderate protection), orange (weak protection), red (very low protection). For segment 23 - 38, marked with ($^*$), $N_{fast}$ (27% ± 5) is not comparable to $N_{loop}$ (100%). The intrinsic profile for that segment was therefore constructed from the lowest 5 (i.e. 30% of 15 amides) intrinsic rates, which gives the 'lower bound' PF of 16. Error bars are from two or three replicates depending on the number of experiments in which the peptide was detected.

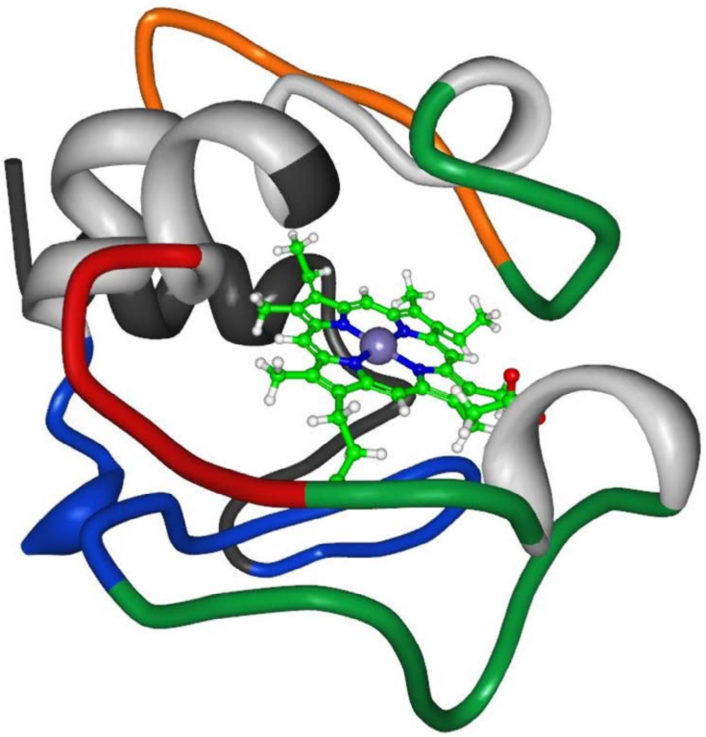

**Figure 3.5**. A graphical representation of cytochrome c loop dynamics based on time-resolved HDX data. Differing levels of protection in loops are mapped onto the solution structure for oxidized horse heart cytochrome c (1AKK) [49] by PF: blue (strong protection), green (moderate protection), orange (weak protection), red (very low protection). Structured regions covered by observed peptides are shown in light grey. Regions for which no peptides were observed are colored dark grey. Image generated using Protein Workshop [50].

On this timescale, there should be virtually no contribution from regions with secondary structure, an assumption that can be tested by comparing the amplitude of the observed exchange to the amount of secondary structure in the peptide. For example, the peptide corresponding to residues 84 - 95 is 30% loop in the native structure. The amplitude for the 'fast' exchange component $N_{\text{fast}}$ is 32 ± 8%, which is agrees very closely with the expected contribution from loop amides. We observe a similar correlation for almost all peptides, which indicates a good agreement between the NMR structure and the actual structure of the protein in solution and supports the assumption that the observed exchange is attributable specifically to loop amides.

Coloring is therefore restricted to loops (Figure 3.5) and average $k_{\text{int}}$ values for PF calculations are derived from loop amides only. In the instance where $N_{\text{fast}}$ is substantially lower than the number of loop amides (*i.e.* segment 22 - 37), the whole peptide is shown colored and the PF was estimated using the average $k_{\text{int}}$ for the whole segment. $N_{\text{loop}}$ and $N_{\text{fast}}$ values for each peptide are provided in Table 3.2, together with 'loop localized, segment averaged' PFs.

**Table 3.2: Time-resolved HDX parameters for peptides from cytochrome c.**

| Segment | $N_{\text{loop}}$ (% of peptide) | $N_{\text{fast}}$ ( % of peptide)[‡] | PF |
|---|---|---|---|
| 23-38 | 100 | 27 ± 5 | 57 ± 12[*] |
| 38-65 | 38 | 41 ± 6 | 12 ± 3 |
| 58-66 | 37 | 31 ± 4 | 5 ± 1 |
| 68-81 | 44 | 40 ± 6 | 10 ± 3 |
| 82-97 | 33 | 25 ± 6 | 6 ± 3 |
| 84-97 | 23 | 26 ± 7 | 8 ± 4 |
| 84-95 | 30 | 32 ± 8 | 12 ± 5 |
| 96-105 | 33 | 27 ± 6 | 22 ± 6 |
| 98-105 | 40 | 32 ± 4 | 25 ± 5 |
| 99-105 | 47 | 36 ± 8 | 27 ± 8 |

[‡] Error measurements are based on two or three replicates depending on the number of experiments in which the peptide was detected.

[*] Since $N_{\text{fast}} << N_{\text{loop}}$ for this peptide, we can provide only an estimate of the PF based on the average intrinsic rate for the whole peptide. We can also determine upper and lower bounds by assuming that the amides contributing to the observed exchange are those with the lowest and highest intrinsic rates, respectively.

From the HDX kinetics measurements overall, it is clear that the loops in cytochrome c have substantially different dynamic properties, with 'segment averaged' PFs ranging from 5 ± 1 ($\alpha 2$ - $\alpha 3$ loop) to 57 ± 12 (the $\alpha 1$ - $\alpha 2$ loop). While there are to the best of our knowledge no directly comparable measurements of native cytochrome c loop dynamics under native conditions, our profile is generally in good agreement with 'native state HDX' thermodynamic stability measurements by Englander and co-workers [47, 48] and can be rationalized by focusing on the influence of the heme prosthetic group. For instance, the least dynamic loop segment (22 - 37) is from the same loop as the heme covalent attachment site (Cys 14 and Cys 17) and is likely rigidly held in place by interactions between heme and its binding pocket. This loop is identified in native HDX experiments as being particularly resistant to denaturation [47, 51] . In fact, many backbone amides in the 22 - 37 segment are so strongly hydrogen bonded that exchange is only at 40% after 48 h of incubation in $D_2O$ (data not shown). Since on our rapid time-scale measurements detected exchange in only 5 of the amides from this 15 residue peptide ($N_{\text{fast}}$ = 27 ± 5%, $N_{\text{loop}}$ = 100%), the upper and lower bounds on the PF are widely separated. Taking the slowest 5 intrinsic rates, the PF would be 16, corresponding to the second-highest protection factor bin (green). If we assume that amides contributing to the observed exchange are those with the 5 fastest $k_{\text{int}}$, the PF is 102, corresponding to the highest protection factor bin (blue). In either case, in appears all amides in the $\alpha 1$ - $\alpha 2$ loop are substantially protected.

The most rapid exchange was measured in the $\alpha 2$ - $\alpha 3$ loop (PF = 5 ± 1) which has only one significant contact with heme (a hydrogen bond between a heme carboxylate and the Trp59 $\varepsilon^1$N proton). The $\alpha 4$ - $\alpha 5$ loop showed a dual dynamic character, with significant protection near the $\alpha 4$ helix where there are substantial contacts with heme (including Met80 which is an axial ligand for the heme iron), and lower protection as the loop moves away from the heme binding pocket approaching the α5 helix. At pD 7.6, all of the exchange processes that allow us to compare loop dynamics are complete within a few seconds of initiating exchange. The time-resolution afforded by our apparatus is therefore crucial to the acquisition of loop dynamics profiles of this type.

**3.3.4 Localizing Dynamics in a Large Tetrameric Enzyme**. The primary advantage of bottom-up HDX is that it is a *general* method. It is applicable to virtually any protein and is not size-limited. Here we demonstrate a time-resolved, bottom-up HDX analysis on the enzyme DAHP synthase, a 154 kDa homotetramer. Our interest in DAHP synthase stems from 'global' HDX measurements (*i.e.*, no digestion prior to analysis) in which it was observed that, in the absence of substrate, the protein underwent a very large (~65%) burst-phase of backbone amide exchange within 20 s of $D_2O$ exposure, suggesting an unusually high degree of conformational flexibility in the unbound tetramer. The substrate-bound protein, on the other hand, showed a more typical ~25% burst-phase (data not shown). This was consistent with efforts to crystallize the protein, which were successful only in the presence of substrates (or competitive inhibitors).[52] In this section, we use our microfluidic device to localize and characterize this burst-phase exchange.

Typical kinetic profiles from three DAHP peptides (Figure 3.6) illustrate the major difference between DAHP exchange kinetics and those from cytochrome c, which was that the majority of DAHP peptides showed no correlation between $N_{\text{fast}}$ and $N_{\text{loop}}$ values. $N_{\text{loop}}$ was determined from the available substrate-bound structure (PDB code 1KFL) [52]. For example, the peptide 118 - 124 is 100% α-helix in the 1KFL structure and yet we still detect a large number of backbone amides undergoing exchange ($N_{\text{fast}}$ = 77 ± 15%) with low protection. This would suggest that the 118 - 124 α-helix is at most weakly structured in the absence of substrate. The general lack of correlation between $N_{\text{fast}}$ and $N_{\text{loop}}$ in our DAHP data indicates substantial structural and/or dynamic differences between the substrate-bound and unbound forms of the protein (which is expected based on the 'global' HDX results). Nonetheless, electrospray mass spectra of DAHP strongly suggested that the protein was able to retain its native tetrameric configuration in the absence of substrate (data not shown). In fact, the HDX data are consistent with this observation in that those peptides that *do* show a good correlation between $N_{\text{fast}}$ and $N_{\text{loop}}$ are concentrated at the tetramer interface (Figure 3.6). Thus, we can infer that the tetramer interface structure reported in 1KFL is largely intact in the unbound protein.

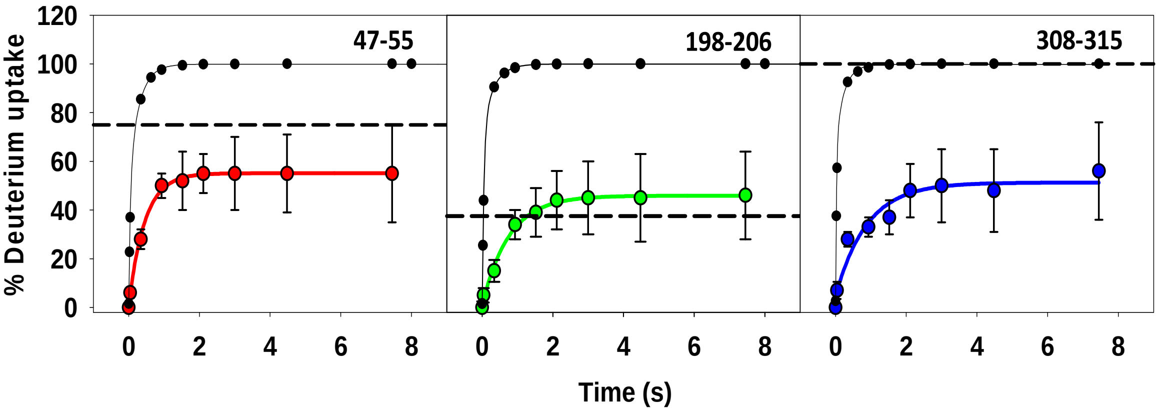

**Figure 3.6**. HDX kinetics for representative peptides from DAHP synthase. Intrinsic rate profiles $D(t)_{\text{int}}$ for each segment are shown in black. The measured profiles are represented by filled circles colored according to the extracted PF: blue (strong protection), green (moderate protection), red (low protection). For most peptides, there is little correlation between $N_{\text{fast}}$ and the number of loop amides in the substrate-bound structure.

A second general difference from the cytochrome c data is that the overall level of exchange is much higher, averaging 73% (average exchange level for cytochrome c = 30%). This is consistent with a weak hydrogen bonding network undergoing 'molten globule-like' dynamics over a significant fraction of the protein [53]. Characterizing this weak network is important, since it may represent a template for the rapid development of structure upon substrate binding. 'Segment averaged' PFs, $N_{\text{fast}}$ amplitudes and $N_{\text{loop}}$ for each DAHP peptide are provided in Table 3.3.

**Table 3.3: Time-resolved HDX statistics for peptides from DAHP synthase.**

| Segment | $N_{\text{loop}}$ (% of peptide) | $N_{\text{fast}}$ (% of peptide)$^{‡}$ | PF |
|---|---|---|---|
| 3-9 | 100 | 57 ± 10 | 16 ± 6 |
| 18-23 | 50 | 59 ± 12$^{*}$ | 5 ± 4 |
| 24-36 | 17 | 100 ± 5 | 27 ± 6 |
| 47-55 | 75 | 55 ± 10 | 6 ± 3 |
| 69-72 | 0 | 48 ± 11 | 5 ± 3 |
| 83-88 | 100 | 97 ± 9$^{*}$ | 2 ± 1 |
| 88-91 | 0 | 69 ± 12 | 2 ± 1 |
| 96-108 | 77 | 100 ± 11 | 11 ± 3 |
| 97-102 | 80 | 100 ± 17 | 10 ± 4 |
| 105-113 | 25 | 61 ± 8 | 6 ± 2 |
| 108-114 | 50 | 92 ± 10 | 5 ± 3 |
| 108-117 | 67 | 74 ± 12$^{*}$ | 15 ± 5 |
| 118-123 | 0 | 73 ± 10 | 9 ± 3 |
| 118-124 | 0 | 77 ± 15 | 8 ± 4 |
| 134-140 | 33 | 98 ± 19 | 23 ± 9 |
| 158-165 | 57 | 73 ± 11 | 15 ± 5 |
| 186-191 | 100 | 68 ± 14 | 24 ± 8 |
| 196-203 | 0 | 76 ± 16 | 11 ± 6 |
| 198-206 | 38 | 45 ± 9$^{*}$ | 12 ± 3 |
| 205-216 | 55 | 64 ± 10$^{*}$ | 14 ± 4 |
| 216-220 | 50 | 54 ± 7$^{*}$ | 24 ± 5 |
| 222-226 | 50 | 50 ± 6$^{*}$ | 32 ± 5 |
| 232-235 | 33 | 98 ± 16 | 4 ± 1 |
| 250-253 | 0 | 75 ± 18 | 7 ± 3 |
| 254-257 | 33 | 73 ± 16 | 9 ± 4 |
| 258-262 | 75 | 73 ± 12$^{*}$ | 5 ± 2 |
| 262-267 | 40 | 55 ± 10 | 3 ± 1 |
| 262-268 | 50 | 68 ± 10 | 5 ± 2 |
| 276-281 | 0 | 18 ± 5 | 25 ± 11 |
| 282-293 | 18 | 74 ± 13 | 20 ± 6 |

| | | | |
|---|---|---|---|
| 284-293 | 22 | 62 ± 9 | 12 ± 3 |
| 289-294 | 60 | 59 ± 8[*] | 12 ± 2 |
| 290-296 | 83 | 87 ± 17[*] | 16 ± 4 |
| 292-296 | 100 | 72 ± 15 | 11 ± 3 |
| 300-305 | 100 | 74 ± 11 | 8 ± 2 |
| 308-315 | 100 | 47 ± 18 | 23 ± 11 |
| 309-313 | 100 | 60 ± 15 | 32 ± 8 |
| 343-346 | 0 | 50 ± 12 | 19 ± 9 |

[‡] Error measurements are based on two or three replicates depending on the number of experiments in which the peptide was detected.

[*] Indicates peptides where there is a reasonable correlation (≤ 10% difference) between $N_{\mathrm{loop}}$ and $N_{\mathrm{fast}}$. PFs for these peptides were generated using 'loop localized' intrinsic rate profiles. The positions of these peptides in the substrate-bound structure (1KFL) are shown in Figure 3.7a.

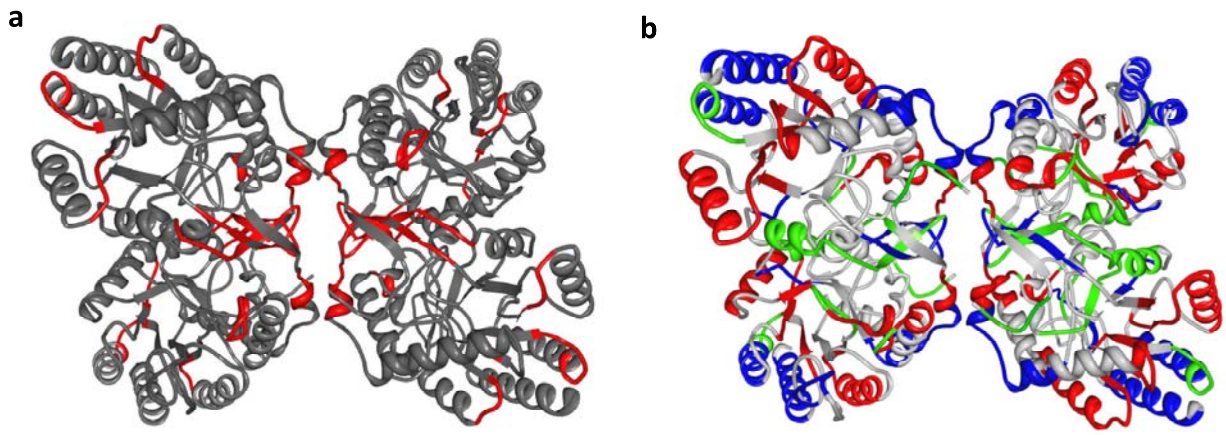

**Figure 3.7**. DAHP exchange profiles mapped on to the substrate-bound 1KFL structure. (a) Highlighted regions correspond to peptides in which $N_{\mathrm{fast}}$ is in reasonable agreement with $N_{\mathrm{loop}}$, suggesting similarity between the apo-protein structure and the PEP-bound structure (1KFL).[52] Many of the peptides with this property are located at the tetramer interface. (b) Observed peptides are mapped onto the PEP-bound DAHP structure (1KFL), colored by PF: blue (strong protection), green (moderate protection), red (low protection). Note that on our relative scale even 'strong protection' corresponds to loop-like exchange (PF ≤ 32), thus many regions that are structured in the substrate-bound state ($N_{\mathrm{loop}} = 0$) are clearly much less so in the apo-protein ($N_{\mathrm{fast}} >> N_{\mathrm{loop}}$). Images were created using Protein Workshop [50].

The DAHP synthase dynamics profile is mapped onto the substrate-bound structure 1KFL (Figure 3.7b) with observed peptides colored by PF from blue (high protection) to red (very low protection). Based on the profile, it is evident that the large burst-phase of exchange is localized to an area surrounding the active site, where all peptides underwent substantial exchange independent of their structural content in 1KFL. All of these segments are well positioned to be strongly influenced by the presence of substrate in the active site. Least protected was the region corresponding to the α3-helix (PF = 7 ± 3). Two helices located at the center of the group of α-helices surrounding the active site (α11 and α10) had a significant level of protection (PF 27 ± 8 and 20 ± 6) in the unbound protein, suggesting the presence of 'residual' structure. These regions and others with significant 'residual' structure in the unbound-protein (blue color, Figure 3.7b) may represent nuclei for the rapid development of structure upon substrate binding.

## 3.4 CONCLUSIONS

We have demonstrated a new, broadly applicable approach for measuring dynamics in weakly structured regions of proteins. The method represents a powerful tool for characterizing dynamics in loops, molten-globules and other weakly structured elements that are inaccessible in conventional experiments at physiological pH. By incorporating the entire HDX experimental workflow onto a single microfluidic chip, and using short (ms to s) labeling times, we were able to: (**i**) produce high contrast secondary structure predictions using single time-point measurements, (**ii**) differentiate the dynamic properties of loops and (**iii**) characterize weak hydrogen bonding networks in ‘molten globule-like’ protein segments. These experiments are straightforward, inexpensive and have a wide range of applications in ligand binding, protein aggregation/amyloidosis. The method provides a versatile platform to enhance our understanding of dynamics in weakly structured regions and may offer much-needed insights into the structural properties of ‘intrinsically disordered’ proteins.

# REFERENCES

1. Kresten Lindorff-Larsen, R.B.B., Mark A. DePristo, Christopher M. Dobson and Michele Vendruscolo, *Simultaneous Determination of Protein Structure and Dynamics.* Nature, 2005. **433**(13): p. 128-132.
2. Frauenfelder, H., S.G. Sligar, and P.G. Wolynes, *The Energy Landscapes and Motions of Proteins.* Science, 1991. **254**(5038): p. 1598-1603.
3. Sterner, R. and W. Liebl, *Thermophilic adaptation of proteins.* Crit. Rev. Biochem. Mol. Biol., 2001. **36**(1): p. 39-106.
4. Benkovic, S.J. and S. Hammes-Schiffer, *A perspective on enzyme catalysis.* Science, 2003. **301**(5637): p. 1196-1202.
5. Pan, J.X., et al., *Hydrogen/Deuterium Exchange Mass Spectrometry with Top-Down Electron Capture Dissociation for Characterizing Structural Transitions of a 17 kDa Protein.* J. Am. Chem. Soc., 2009. **131**(35): p. 12801-12808.
6. Mulder, F.A.A., et al., *Studying Excited States of Proteins by NMR Spectroscopy.* Nat. Struct. Mol. Biol, 2001. **8**(11): p. 932-935.
7. Elan Z. Eisenmesser, O.M., Wladimir Labeikovsky, Dmitry M. Korzhnev, Magnus Wolf-Watz1, Daryl A. Bosco1, Jack J. Skalicky, Lewis E. Kay and Dorothee Kern, *Intrinsic Dynamics of an Enzyme Underlies Catalysis.* Nature, 2005. **438**: p. 117-121.
8. Zuiderwegy, D.K.a.E.R., *The Role of Dynamics in Allosteric Regulation.* Curr. Opin. Struct. Biol., 2003. **13**: p. 748-757.
9. Hartl, F.U. and M. Hayer-Hartl, *Converging concepts of protein folding in vitro and in vivo.* Nat. Struct. Mol. Biol., 2009. **16**(6): p. 574-581.
10. Bemporad, F., et al., *Sequence and structural determinants of amyloid fibril formation.* Accounts Chem. Res., 2006. **39**(9): p. 620-627.
11. Bucciantini, M., et al., *Inherent toxicity of aggregates implies a common mechanism for protein misfolding diseases.* Nature, 2002. **416**(6880): p. 507-511.
12. Sanchez-Ruiz, J.M., *Protein kinetic stability.* Biophys. Chem., 2010. **148**(1-3): p. 1-15.

13. Wagner, G. and K. Wuthrich, *Amide proton-exchange and surface conformation of the basic pancreatic trypsin inhibitor in solution - studies with two dimensional nuclear magnetic resonance.* J. Mol. Biol., 1982. **160**(2): p. 343-361.

14. Zhang, Z.Q. and D.L. Smith, *Determination of Amide Hydrogen-Exchnage by Mass Spectrometry - A New Tool for Protein Structure Elucidation.* Protein Sci, 1993. **2**(4): p. 522-531.

15. Englander, S.W., et al., *Mechanisms and uses of hydrogen exchange.* Current Opinion in Structural Biology, 1996. **6**(1): p. 18-23.

16. Mori, S., et al., *Improved Sensitivity of HSQC Spectra of Exchanging Protons at Short Interscan Delays Using a New Fast HSQC (FHSQC) Detection Scheme That Avoids Water Saturation.* J. Magn. Reson. B, 1995. **108**(1): p. 94-98.

17. Keppel, T.R., B.A. Howard, and D.D. Weis, *Mapping Unstructured Regions and Synergistic Folding in Intrinsically Disordered Proteins with Amide H/D Exchange Mass Spectrometry.* Biochemistry, 2011. **50**(40): p. 8722-8732.

18. Wales, T.E. and J.R. Engen, *Hydrogen exchange mass spectrometry for the analysis of protein dynamics.* Mass Spectrometry Reviews, 2006. **25**(1): p. 158-170.

19. Peter L. Ferguson, J.P., Derek J. Wilson, Brian Dempsey, Gilles Lajoie, Brian Shilton and Lars Konermann, *Hydrogen/Deuterium Scrambling During Quadrupole Time-of-Flight MS/MS Analysis of a Zinc-Binding Protein Domain.* Anal. Chem., 2007. **79**: p. 153-160.

20. Jorgensen, T.J.D., et al., *Intramolecular migration of amide hydrogens in protonated peptides upon collisional activation.* J. Am. Chem. Soc., 2005. **127**(8): p. 2785-2793.

21. Hoerner, J.K., et al., *Is there hydrogen scrambling in the gas phase? Energetic and structural determinants of proton mobility within protein ions.* J. Am. Chem. Soc., 2004. **126**(24): p. 7709-7717.

22. Konermann, L., J. Pan, and Y.-H. Liu, *Hydrogen exchange mass spectrometry for studying protein structure and dynamics.* Chemical Society Reviews, 2011. **40**(3): p. 1224-1234.

23. Rand, K.D., et al., *Investigation of amide hydrogen back-exchange in Asp and His repeats measured by hydrogen ((1)H/(2)H) exchange mass spectrometry.* International Journal of Mass Spectrometry, 2011. **302**(1-3): p. 110-115.

24. Zhang, H.M., et al., *Fast Reversed-Phase Liquid Chromatography to Reduce Back Exchange and Increase Throughput in H/D Exchange Monitored by FT-ICR Mass Spectrometry.* J. Am. Soc. Mass Spectrom., 2009. **20**(3): p. 520-524.

25. Dempsey, C.E., *Hydrogen exchange in peptides and proteins using NMR-spectroscopy.* Prog. Nucl. Mag. Res. Sp., 2001. **39**(2): p. 135-170.

26. Marcsisin, S.R. and J.R. Engen, *Hydrogen exchange mass spectrometry: what is it and what can it tell us?* Analytical and Bioanalytical Chemistry, 2010. **397**(3): p. 967-972.

27. Raschke, T.M. and S. Marqusee, *The kinetic folding intermediate of ribonuclease H resembles the acid molted globule and partially unfolded molecules detected under native conditions.* Nat. Struct. Biol., 1997. **4**(6): p. 505-505.

28. Chamberlain, A.K., T.M. Handel, and S. Marqusee, *Detection of rare partially folded molecules in equilibrium with the native conformation of RNaseH.* Nat. Struct. Biol., 1996. **3**(9): p. 782-787.

29. Hwang, T.L., P.C.M. van Zijl, and S. Mori, *Accurate quantitation of water-amide proton exchange rates using the Phase-Modulated CLEAN chemical EXchange (CLEANEX-PM) approach with a Fast-HSQC (FHSQC) detection scheme.* J. Biomol. NMR, 1998. **11**(2): p. 221-226.

30. Mori, S., et al., *NMR study of rapidly exchanging backbone amide protons in staphylococcal nuclease and the correlation with structural and dynamic properties.* J. Am. Chem. Soc., 1997. **119**(29): p. 6844-6852.

31. Rob, T. and D.J. Wilson, *A Versatile Microfluidic Chip for Millisecond Time-scale Kinetic Studies by Electrospray Mass Spectrometry.* J. Am. Soc. Mass Spectr., 2009. **20**(1): p. 124 - 130.

32. Liuni, P., T. Rob, and D.J. Wilson, *A microfluidic reactor for rapid, low-pressure proteolysis with on-chip electrospray ionization.* Rapid Commun. Mass Spectrom., 2010. **24**(3): p. 315-320.

33. Brown, L., et al., *Fabrication and characterization of poly(methylmethacrylate) microfluidic devices bonded using surface modifications and solvents.* Lab on a Chip, 2006. **6**(1): p. 66-73.

34. Bai, Y.W., et al., *Primary Structure Effects on Peptide Group Hydrogen-exchange.* Proteins, 1993. **17**(1): p. 75-86.

35. Zhang, Y.-Z., *Sphere: Protein and peptide structure and interactions studied by hydrogen exchange and NMR.* PhD Thesis, 2001.

36. Hollien, J. and S. Marqusee, *Structural distribution of stability in a thermophilic enzyme.* P. Natl. Acad. Sci. USA, 1999. **96**(24): p. 13674-13678.

37. Best, R.B. and M. Vendruscolo, *Structural interpretation of hydrogen exchange protection factors in proteins: Characterization of the native state fluctuations of C12.* Structure, 2006. **14**(1): p. 97-106.

38. Landreh, M., et al., *New developments in protein structure-function analysis by MS and use of hydrogen-deuterium exchange microfluidics.* Febs J., 2011. **278**(20): p. 3815-3821.

39. Wang, B., et al., *Chemical force titrations of antigen- and antibody-modified poly(methylmethacrylate).* Colloids and Surfaces B-Biointerfaces, 2007. **55**(1): p. 107-114.

40. Pan, J.X., et al., *Characterizing Short-Lived Protein Folding Intermediates by Top-Down Hydrogen Exchange Mass Spectrometry.* Anal. Chem., 2010. **82**(20): p. 8591-8597.

41. Wilson, D.J. and L. Konermann, *A Capillary Mixer with Adjustable Reaction Chamber Volume for Millisecond Time-Resolved Studies by Electrospray Mass Spectrometry.* Anal. Chem., 2003. **75**: p. 6408 - 6414.

42. Hamuro, Y., et al., *Rapid analysis of protein structure and dynamics by hydrogen/deuterium exchange mass spectrometry.* J. Biol. Tech., 2003. **14**(3): p. 171-82.

43. Lange, O.F., et al., *Recognition Dynamics Up to Microseconds Revealed from an RDC-Derived Ubiquitin Ensemble in Solution.* Science, 2008. **320**(5882): p. 1471-1475.

44. Bougault, C., et al., *Quantitation of rapid proton-deuteron amide exchange using hadamard spectroscopy.* J. Biomol. NMR, 2004. **28**(4): p. 385-390.

45. Vijay-Kumar, S., C.E. Bugg, and W.J. Cook, *Structure of ubiquitin refined at 1.8A resolution.* J. Mol. Biol., 1987. **194**(3): p. 531-544.

46. Wang, L.T., H. Pan, and D.L. Smith, *Hydrogen exchange-mass spectrometry - Optimization of digestion conditions.* Molecular & Cellular Proteomics, 2002. **1**(2): p. 132-138.

47. Bai, Y.W., et al., *Protein-folding intermediates - Native-State Hydrogen-Exchange.* Science, 1995. **269**(5221): p. 192-197.

48. Hoang, L., et al., *Cytochrome c folding pathway: Kinetic native-state hydrogen exchange.* P. Natl. Acad. Sci. USA, 2002. **99**(19): p. 12173-12178.

49. Banci, L., et al., *Solution Structure of Oxidized Horse Heart Cytochrome c.* Biochemistry, 1997. **36**(32): p. 9867-9877.

50. Moreland, J.L., et al., *The Molecular Biology Toolkit (MBT): A Modular Platform for Developing Molecular Visualization Applications.* BMC Bioinformatics, 2005. **6**(21).

51. Milne, J.S., et al., *Experimental study of the protein folding landscape: Unfolding reactions in cytochrome c.* J. Mol. Biol., 1999. **290**(3): p. 811-822.

52. Shumilin, I.A., et al., *Allosteric Inhibition of 3-Deoxy-d-arabino-heptulosonate-7-phosphate Synthase Alters the Coordination of Both Substrates.* J. Mol. Biol., 2002. **320**(5): p. 1147-1156.

53. Nabuurs, S.M. and C.P.M. van Mierlo, *Interrupted Hydrogen/Deuterium Exchange Reveals the Stable Core of the Remarkably Helical Molten Globule of α-β Parallel Protein Flavodoxin.* J. Biol. Chem., 2010. **285**(6): p. 4165-4172.

# CHAPTER 4

## The Effect of Ligand Binding on Conformational Dynamics of DAHP Synthase using Microfluidics Enabled Hydrogen/ Deuterium Exchange

### 4.1 INTRODUCTION

The enzyme 3-deoxy-D-arabinoheptulosonate 7-phosphate (DAHP synthase) is the first enzyme of the shikimate pathway, associated with the biosynthesis of the aromatic amino acids in microorganisms and plants [1]. Shikimate pathway involves a sequence of seven metabolic steps where in the first step DAHP synthase catalyzes the stereospecific aldol condensation of phosphoenolpyruvate (PEP) and D-erythrose 4-phosphate (E4P) to DAHP and inorganic phosphate (Figure 4.1).

Phosphoenolpyruvate (PEP) + D-erythrose 4-phosphate (E4P) + $H_2O \rightleftharpoons$ 3-deoxy-D-arabino-hept-2-ulosonate 7-phosphate (DAHP) + phosphate (Pi)

In following sequential steps, DAHP undergoes several other transformations before it is converted into chorismate, the precursor of the aromatic amino acids phenylalanine (Phe), tyrosine (Tyr), and tryptophan (Trp) and many aromatic secondary metabolites [2-4]. Furthermore, DAHP synthase regulates the amount of carbon entering the shikimate pathway which involves the enzyme inhibition by the three major end products of the biosynthetic pathway i.e. Phe, Tyr, Trp. The concentrations of each of the three aromatic amino acids are continuously monitored in the cell. When there is too much of any one of them, that one will allosterically control the DAHP synthase by "turning it off". This regulation can be accomplished primarily through two different mechanisms: Feedback inhibition and transcriptional control. The most comprehensively investigated DAHP synthase has been the *Escherichia coli* enzyme system. In *E. coli*, DAHP synthase is found as three isoenzymes where the organism encodes each of them by the structural genes: *aro F* (Tyr-sensitive DAHP synthase), *aro G* (Phe-sensitive DAHP synthase), *aro H* (Trp-sensitive DAHP synthase) [5, 6] . In the current work, we focused on studying conformational dynamics of Phe-sensitive DAHP synthase upon ligand binding.

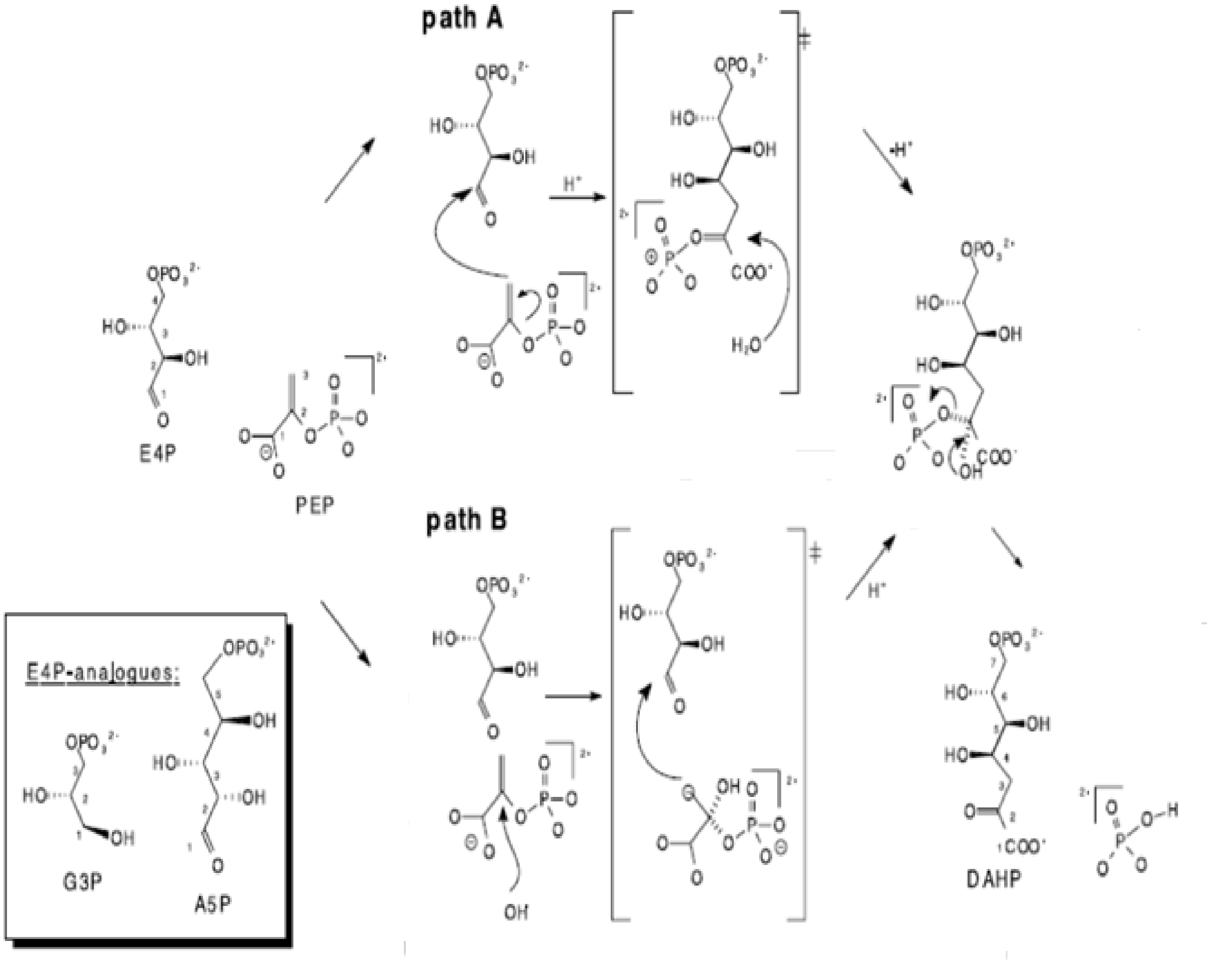

**Figure 4.1.** Simplified description of two possible pathways for biosynthesis of DAHP in DAHP synthase [7].

The biosynthetic pathway of aromatic amino acids is absent in animals, hence the products of this pathway represent essential amino acids that must be obtained for the animal's diet. Therefore it is important to understand the enzyme mechanism in order to design synthesis of aromatic amino acids that underlies critical in the diets of mammals. Additionally, DAHP synthase responses to a broad range of developmental cues and environmental stimuli mechanisms which controls carbon flow into the shikimate pathway [7, 8]. This alters the demand for aromatic amino acid-derived metabolites in plants during plant development and/or during periods of environmental stress such as wounding or pathogen attack. Under stress conditions, plants produce high amount of lignin which is directly mediated by aromatic compound synthesis [9]. In many farming industries, controlling the bacterial growth is extremely challenging. An accepted inhibitor for DAHP synthase would inhibit pathogen attack while leaving the host organism unaffected which can address this issue [10, 11]. Though this phenomenon is not directly related to *E. coli* Phe sensitive DAHP synthase, understanding the response of *E. coli* DAHP to ligands will provide insight of its allosteric interactions that can be associated with inhibitor designing for its other isoforms [12-14]. Therefore, the DAHP synthase represents an attractive molecular target for antibiotic design [15, 16]. The mechanism of DAHP enzyme has been extensively investigated in past years, however its conformational dynamics are under investigated due to lack of appropriate analytical approaches.

The Phe sensitive DAHP synthase from *E. coli* is a metalloenzyme that may bind to a variety of metal ions at its active site and at a different stoichiometry, depending on the physiological conditions under which the bacteria are grown. However, the preferred metal co-factors appear to be divalent, mainly $Fe^{2+}$ and perhaps $Zn^{2+}$ though $Co^{2+}$, $Mn^{2+}$, $Cu^{2+}$ are also common cofactors in *E. coli* DAHP synthase [17]. The metal ion plays a crucial but indirect role in catalysis, stabilization the conformation of the enzyme. Recent studies suggest that the metal ion along with the first substrate PEP, orders the secondary structure of the enzyme to assists binding of the second substrate E4P [18, 19]. Bonding of metal ions and/or ligands positions the amino acids and 7 water molecules around the active site of the enzyme with the appropriate geometry required to coordinate and activate the water molecule that is the third reactant of the condensation reaction [18, 20]. This conformational ordering is likely linked to the problem faced by the crystallographers in crystallizing apo-DAHP synthase [21, 22]. In fact, only metal binding or substrate binding can allow crystallization of DAHP under atmospheric pressure and low temperature. The crystallographic data demonstrate that the quaternary structure of the substrate or metal bound DAHP synthase consists of two tightly bound dimers suggesting that it exists as a tetramer (154 kDa) which is not as rigid as the bound form [8]. Our observation from the work described in Chapter 3 agrees with a weakly-structured, tetrameric apoprotein while the apo-DAHP is neither amenable to X-ray or NMR studies. HDX/TRESI-MS may represent a suitable approach to probe the structural changes that occur upon binding.

This work represents an application of the continuous labelling HDX device that has been introduced in Chapter 3, specifically, the investigation of the structural consequences of ligand binding. The device was applied to measure differential conformational response of Phe regulated DAHP synthase towards different ligands. Since the enzyme was grown in absence of metal cofactors, the observed ordering of structure reflects the conformation change caused only by the ligands which hasn’t been studied earlier. Using this device we have characterized dynamic behaviour surrounding active sites of DAHP synthase in presence and absence of substrate (PEP) and three inhibitors.

## 4.2 EXPERIMENTAL

**4.2.1 Materials**. Pepsin agarose beads, high purity acetic acid (≥ 99.7%), deuterium oxide ($D_2O$) and all other chemicals were obtained from Sigma (St. Louis, MO). All metal capillaries and PTFE tubings were purchased from McMaster-Carr (Aurora, OH). Standard 1/16″ fittings were purchased from IDEX Health & Science (Oak Harbor, WA). Precut rectangular blocks (8.9 cm x 3.8 cm x 0.3) cm of blank poly(methyl methacrylate) or PMMA substrate was purchased from Professional Plastics (Orchard Park, NY) which was used as platform for etching micro channels and well (32 mm × 5 mm × 0.01 mm) using a LASER engraver (Universal Laser, Scottsdale, AZ).

**4.2.2 H/D Exchange Measurements**. In this work, 200 μM DAHP synthase at pH 7.6 was mixed with its substrate phosphoenol pyruvic acid (PEP) manually and incubated for 30 min prior to HDX experiments. The holo protein was mixed with $D_2O$ (1:3) in the rapid mixing module of the device and the position of the mixer was adjusted manually to change the mixing time. Rest of the experimental parameters was identical to that of free DAHP synthase that has been described earlier in experimental section of Chapter 3. Labeling times were varied from 193 ms to 10 sec using flow rates of 1μL/min for protein solution and 3 μL/min for $D_2O$. Labeling was rapidly quenched to pH 2.5 using acetic acid solution (pH 2.3) at 9 μL/min prior to rapid proteolysis. Individual experiments were carried out in same manner using three different inhibitors oxime, imidazole and glycerol-3-phosohate (G3P) which is an analogue of E4P [7, 8]. The data analysis approach is described in details in data analysis section of Chapter 3). The observed HDX data were analyzed the using home built HDX software and the observed profiles were mapped onto its available PEP bound crystal structure (pdb 1KFL).

## 4.3 RESULTS AND DISCUSSIONS

**4.3.1. Comparison between apo- and PEP- bound structure.** Conformational changes in DAHP synthase upon binding to its substrate and different inhibitors were probed *via* continuous labeling HDX experiments. Our observation from Chapter 3 suggested that the apo DAHP synthase is “molten globule”-like and would need to undergo strong conformational ordering upon binding as there were substantial differences between the structural properties of the apoprotein and the ligand-bound crystal structure. In apoprotein, peptides surrounding active site underwent substantial exchange irrespective of the secondary structure (according to X-ray structure) suggesting the absence of strong hydrogen bonding that makes this regions accessible to deuterium. The observation from current work shows very low D uptake in those peptides and in good agreement with the hypothesis that we made in Chapter 3. This work proves experimentally the presence of a floppy secondary structural template around active sites in absence of any substrate in DAHP synthase. The HDX kinetics in three representative DAHP synthase peptides are compared between apo and PEP bound forms (Figure 4.2). In general there was no correlation between observed D uptake amplitude ($N_{fast}$) with number of loop residues ($N_{loop}$) while a better correlation was observed in the substrate bound form. The regions that show differences in the D uptakes are mapped on to crystal structure 1BTL (Figure 4.3) and colored according to the observed amplitude: navy blue (30-60), deep blue (16-30), blue (10-15), light blue (0-10).

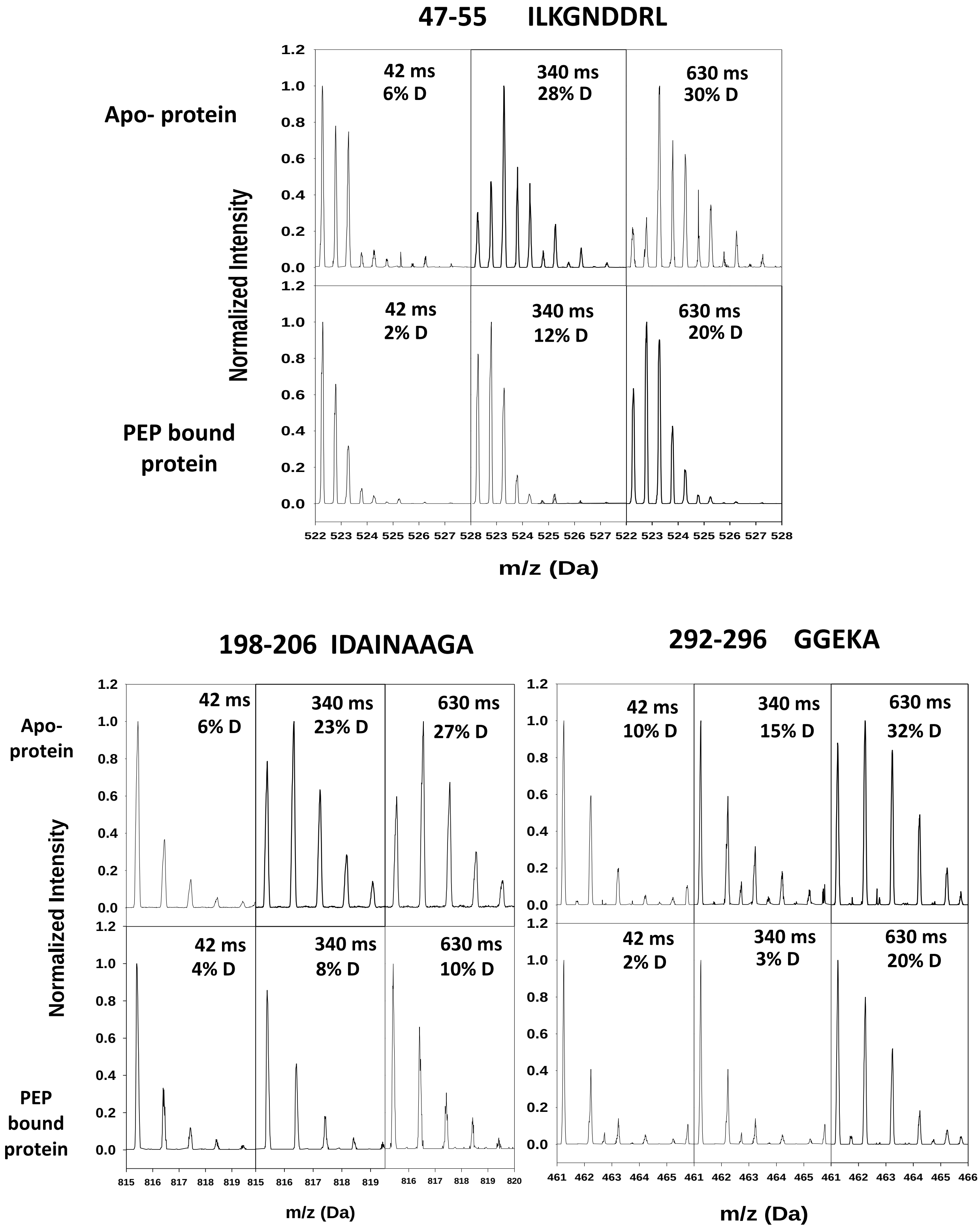

**Figure 4.2**. Raw data for HDX kinetics in three representative DAHP synthase peptides. The '% exchanged' values were generated from a FORTRAN program developed in-house.

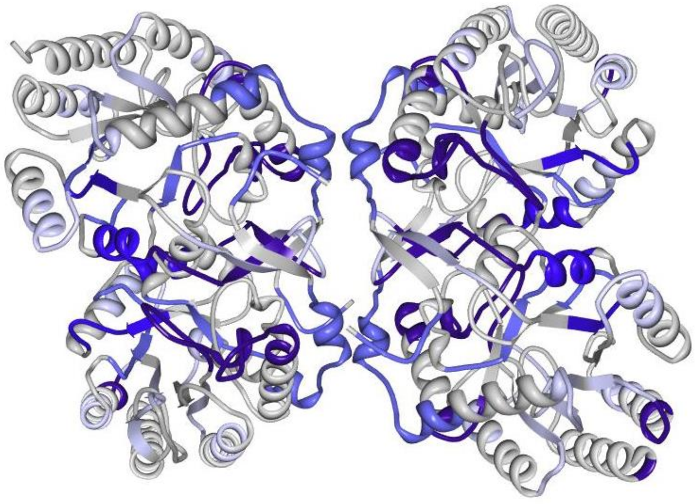

**Figure 4.3.** Differences in deuterium exchange profiles between free and PEP bound DAHP is mapped onto the PEP-bound 1KFL structure. The structure is colored by differences in observed amplitude: navy blue (30-60), deep blue (16-30), blue (10-15), light blue (0-10)

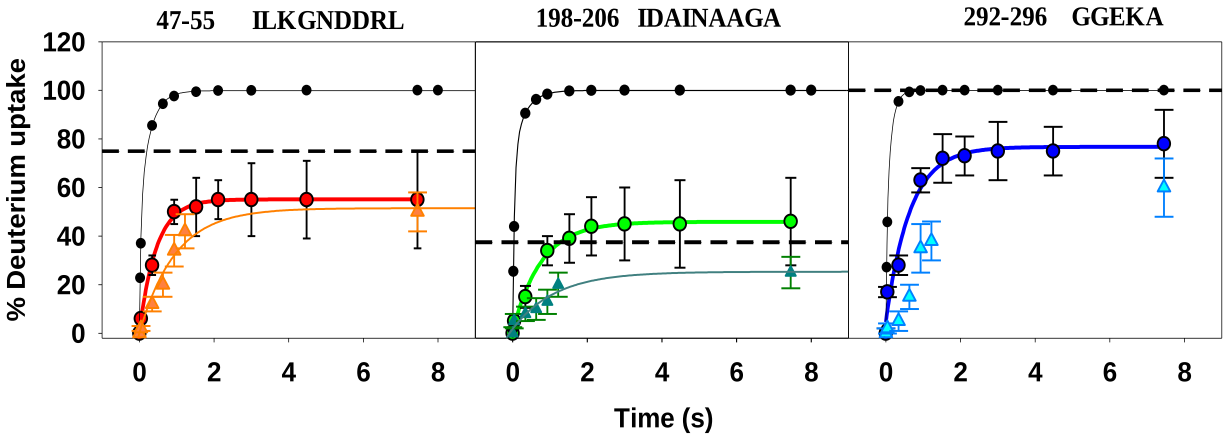

**Figure 4.4.** HDX kinetics for representative peptides from apo and PEP bound DAHP synthase. Intrinsic rate profiles $D(t)_{\mathrm{int}}$ for each segment are shown in black. The measured profiles of apo and PEP bound DAHP synthase are represented by filled circles and triangle respectively and colored according to the extracted PF: blue (strong protection), green (moderate protection), red (low protection). Error measurements are based on two or three replicates depending on the number of experiments in which the peptide was detected.

The observed kinetics on three representative peptides is shown on Figure 4.4. Additionally, the observed peptides are mapped onto the available ligand-bound crystal structure 1BTL (Figure 4.5) showing a significant difference between these two forms. This demonstrates that the device is capable of detecting structural differences and truly reflects the conformational information under any solution conditions.

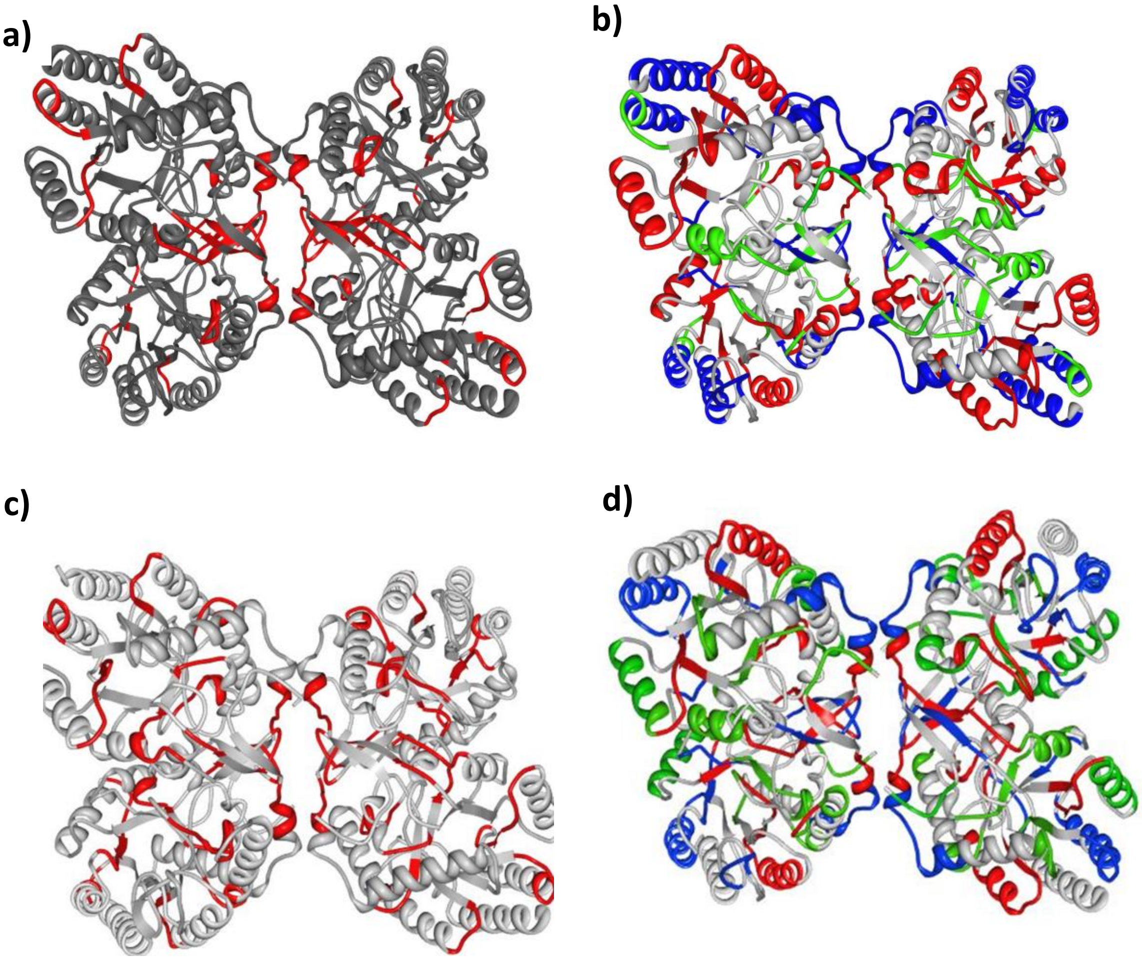

**Figure 4.5**. DAHP exchange profiles are mapped onto the substrate-bound 1KFL structure. (a) and (c) Highlighted regions correspond to peptides in which $N_{\text{fast}}$ is in reasonable agreement with $N_{\text{loop}}$, suggesting similarity between the apo-protein structure and the PEP-bound crystal structure (1KFL). Many of the peptides with this property are located at the tetramer interface. (b) and (d) Observed peptides are mapped onto the PEP-bound DAHP structure (1KFL), colored by PF: blue (strong protection), green (moderate protection), red (low protection).

**4.3.2. Conformational Analysis of Different Ligand Bound Structures.** With extensive data analysis we were able to characterize substantial differences in dynamics near the active sites of the enzymes among the apo and different ligand-bound enzymes. The different structures are compared in terms of the D uptake amplitudes ($N_{\text{fast}}$) and protection factors (PF) exhibited by the peptides that are common in all five systems. The $N_{\text{fast}}$ values are compared with $N_{\text{loop}}$ of the PEP-bound form, using this structure as a baseline for comparing the conformational effects of different substrates and inhibitors. The observed peptides are highlighted on to the substrate-bound 1KFL structure where the regions that are in reasonable agreement (≤ 20% difference) with $N_{\text{loop}}$ ($N_{\text{loop}}$ was calculated based on the PEP- bound form) and colored blue if $N_{\text{fast}} \leq N_{\text{loop}}$ or red if $N_{\text{fast}} \geq N_{\text{loop}}$ (Figure 4.6). However, the peptides on the PEP-bound form are colored blue as $N_{\text{fast}} \approx N_{\text{loop}}$. In general the both inhibitor (oxime and imidazole) bound systems exhibits similar HDX profiles, taking up a relatively higher amount of D around the tetramer interface compared to the PEP-bound form. This observation is also in good agreement with the previous crystallographic and molecular simulation studies where C61 was associated with the catalytic activity. Most likely enhanced flexibility in this region is linked to inhibition.

Conformational flexibilities of different *holo* systems are also compared by calculating PF values where the PF of PEP bound system is considered as a base line and peptides observed in G3P, oxime and imidazole bound systems are mapped on to the PEP-bound 1KFL structure as shown in Figure 4.7. The differences in calculated protection factors are colored by: cyan (stronger protection than PEP), yellow-green (where PF values are within 5% agreement with PF

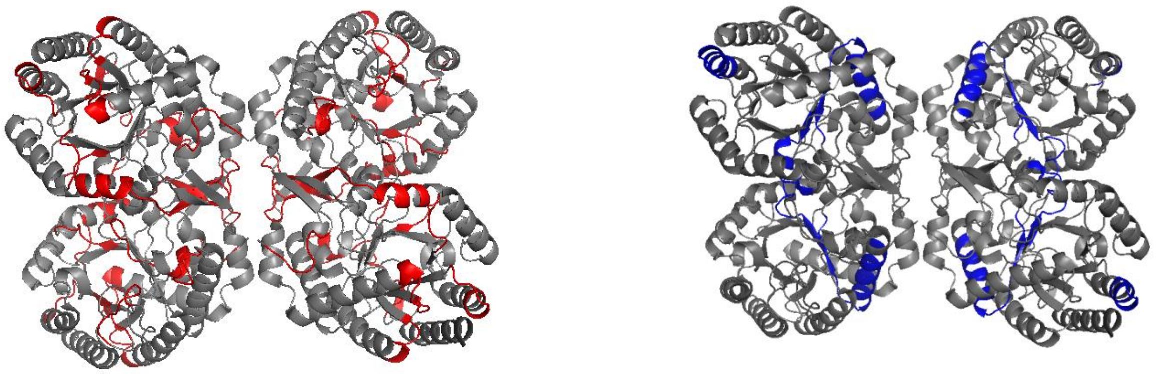

Free DAHP Synthase

PEP bound DAHP Synthase

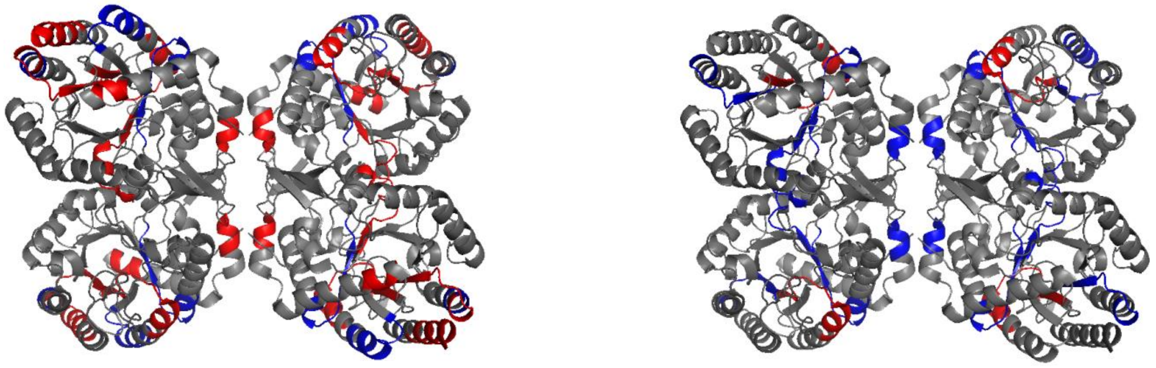

Oxime bound DAHP Synthase

G3P bound DAHP Synthase

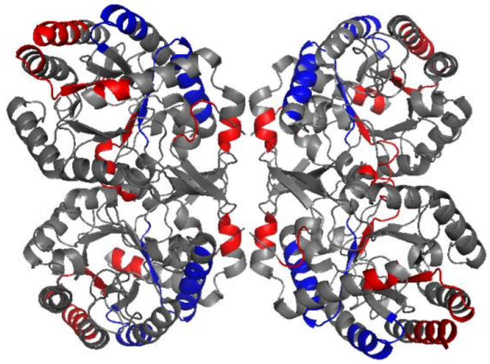

Imidazole bound DAHP Synthase

**Figure 4.6.** DAHP exchange profiles mapped on to the substrate-bound 1KFL structure. Highlighted regions correspond to peptides in which $N_{\mathrm{fast}}$ is in reasonable agreement ($\leq$ 20% difference) with $N_{\mathrm{loop}}$ ($N_{\mathrm{loop}}$ was calculated based on the PEP- bound form) colored blue if $N_{\mathrm{fast}} \leq N_{\mathrm{loop}}$ and red if $N_{\mathrm{fast}} \geq N_{\mathrm{loop}}$ . Figures are generated by Pymol Program,version 1.5.

values of PEP), red (low protection compared to PEP). Our data also suggests that the PEP-bound form has high conformational flexibility near Phenylalanine binding site of the protein compare to the unbound protein, while binding of the inhibitor G3P induces rigidity in the same region. The acidic amino acids in that region probably bind strongly with the basic inhibitors and the smallest inhibitor imidazole causes highest structural perturbation upon binding.

The free enzyme experiences loss of its flexibility around its active site upon binding to PEP which is anticipated but the response of active site towards different inhibitors is more complex. Other inhibitors including histidine and a structurally-related oxime apparently bind to the active site, but fail to induce the development of structure in the enzyme as a whole, as occurs with PEP and G3P. We have observed opposite dynamics around two different PEP binding sites upon G3P binding irrespective of its structural similarities to PEP. The basic inhibitors imidazole and oxime show similar reduced dynamics around these two sites even though in general these two inhibitors retain conformational flexibility upon binding compared to PEP and G3P.

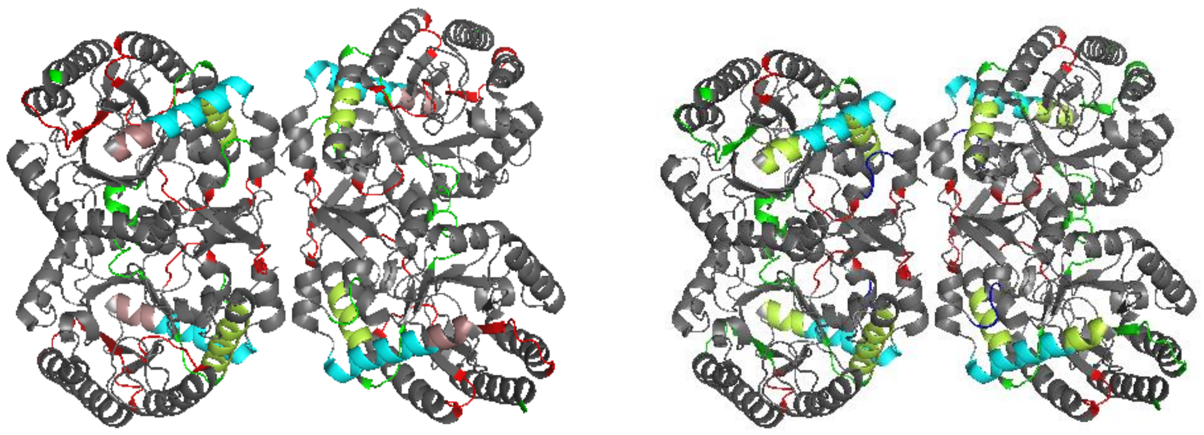

G3P bound DAHP Synthase

Imidazole bound DAHP Synthase

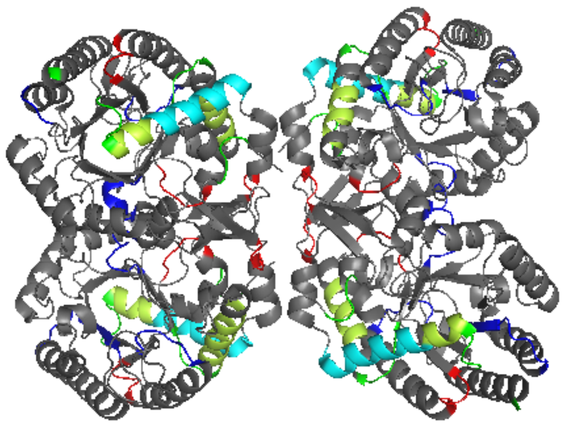

Oxime bound DAHP Synthase

**Figure 4.7**. The differences in calculated protection factors are mapped on to the PEP-bound 1KFL structure where the PF of PEP bound system is considered as a base line. The structure is colored by: cyan (stronger protection than PEP), yellow-green (where PF values are within 5% agreement with PF values of PEP), red (low protection compared to PEP).

## 4.4 CONCLUSIONS

This work successfully demonstrates the application of continuous labeling TRESI/HDX device as a suitable approach for studying conformational changes in enzymes that occur upon ligand binding. The device enabled us to compare structural ordering of DAHP synthases around its active sites and tetramer interfaces caused by ligand (substrate and different inhibitors) by comparing $N_{\mathrm{loop}}$ with $N_{\mathrm{fast}}$ and protection factors (PF) values of apo and different holo enzymes. However, we were unable to probe the asymmetric binding of the ligands on different subunits of the tetramer, which has been proposed as an explanation for cooperative behavior observed during catalysis (unpublished). Therefore, we aim to measure global HDX profile of tetramer with response to all of these small molecules (substrates/ inhibitor) followed by rapid degradation (initiated by a pH jump from 7.0-2.5) into individual monomers prior to ionization. This proposed experiment can provide us information about the asymmetric binding of the subunits and eventually will be beneficial in finding differential dynamic behavior of individual monomers. This study constitutes the dynamic analysis of substrate binding on DAHP synthase and provides insight into questions that may offer valuable input for the design of novel enzyme inhibitors.

# REFERENCES

1. Bentley, R. and E. Haslam, *The Shikimate Pathway â€" A Metabolic Tree with Many Branche.* Critical Reviews in Biochemistry and Molecular Biology, 1990. **25**(5): p. 307-384.

2. Herrmann, K.M., *The shikimate pathway as an entry to aromatic secondary metabolism.* Plant Physiol, 1995. **107**(1): p. 7-12.

3. Herrmann, K.M., *The Shikimate Pathway: Early Steps in the Biosynthesis of Aromatic Compounds.* Plant Cell, 1995. **7**(7): p. 907-919.

4. Herrmann, K.M. and L.M. Weaver, *THE SHIKIMATE PATHWAY.* Annu Rev Plant Physiol Plant Mol Biol, 1999. **50**: p. 473-503.

5. Herrmann, K. and R. Entus, *Shikimate Pathway: Aromatic Amino Acids and Beyond*, in *eLS*. 2001, John Wiley & Sons, Ltd.

6. Halsall, D.M. and C.H. Doy, *Studies concerning the biochemical genetics and physiology of activity and allosteric inhibition mutants of Neurospora crassa 3-deoxy-d-arabino-heptulosonate 7-phosphate synthase.* Biochimica et Biophysica Acta (BBA) - Enzymology, 1969. **185**(2): p. 432-446.

7. Furdui, C., et al., *Insights into the mechanism of 3-deoxy-D-arabino-heptulosonate 7-phosphate synthase (Phe) from Escherichia coli using a transient kinetic analysis.* J Biol Chem, 2004. **279**(44): p. 45618-25.

8. Konig, V., et al., *Substrate and metal complexes of 3-deoxy-D-arabino-heptulosonate-7-phosphate synthase from Saccharomyces cerevisiae provide new insights into the catalytic mechanism.* J Mol Biol, 2004. **337**(3): p. 675-90.

9. Muday, G.K. and K.M. Herrmann, *Wounding Induces One of Two Isoenzymes of 3-Deoxy-d-arabino-Heptulosonate 7-Phosphate Synthase in Solanum tuberosum L.* Plant Physiol, 1992. **98**(2): p. 496-500.

10. Dyer, W.E., et al., *Wounding induces the first enzyme of the shikimate pathway in Solanaceae.* Proc Natl Acad Sci U S A, 1989. **86**(19): p. 7370-3.

11. Helmstaedt, K., et al., *Evolution of 3-deoxy-D-arabino-heptulosonate-7-phosphate synthase-encoding genes in the yeast Saccharomyces cerevisiae.* Proc Natl Acad Sci U S A, 2005. **102**(28): p. 9784-9.

12. Schoner, R. and K.M. Herrmann, *3-Deoxy-D-arabino-heptulosonate 7-phosphate synthase. Purification, properties, and kinetics of the tyrosine-sensitive isoenzyme from Escherichia coli.* J Biol Chem, 1976. **251**(18): p. 5440-7.

13. Jensen, R.A. and S. Ahmad, *Evolution and phylogenetic distribution of the specialized isozymes of 3-deoxy-D-arabino-heptulosonate 7-phosphate synthase in superfamily-B prokaryotes.* Microbiol Sci, 1988. **5**(10): p. 316-9.

14. Berry, A., J.L. Johnson, and R.A. Jensen, *Phenylalanine hydroxylase and isozymes of 3-deoxy-D-arabino-heptulosonate 7-phosphate synthase in relationship to the phylogenetic position of Pseudomonas acidovorans (Ps. sp. ATCC 11299a).* Arch Microbiol, 1985. **141**(1): p. 32-9.

15. Jiao, W., et al., *Dynamic cross-talk among remote binding sites: the molecular basis for unusual synergistic allostery.* J Mol Biol, 2012. **415**(4): p. 716-26.

16. Xu, X., et al., *Structure-based design of novel inhibitors of 3-deoxy-D-manno-octulosonate 8-phosphate synthase.* Drug Des Discov, 2003. **18**(2-3): p. 91-9.

17. Stephens, C.M. and R. Bauerle, *Analysis of the metal requirement of 3-deoxy-D-arabino-heptulosonate-7-phosphate synthase from Escherichia coli.* J Biol Chem, 1991. **266**(31): p. 20810-7.

18. Shumilin, I.A., et al., *Crystal Structure of the Reaction Complex of 3-Deoxy-d-arabino-heptulosonate-7-phosphate Synthase from Thermotoga maritima Refines the Catalytic Mechanism and Indicates a New Mechanism of Allosteric Regulation.* Journal of Molecular Biology, 2004. **341**(2): p. 455-466.

19. Shumilin, I.A., et al., *Allosteric Inhibition of 3-Deoxy-d-arabino-heptulosonate-7-phosphate Synthase Alters the Coordination of Both Substrates.* J. Mol. Biol., 2002. **320**(5): p. 1147-1156.

20. Muday, G.K., *The role of DAHP synthase isozymes in control of carbon flow into the shikimate pathway in bacteria and plants*, in *ProQuest Dissertations and Theses*1989, Purdue University: United States -- Indiana. p. 120-120 p.

21. Schneider, T.R., M. Hartmann, and G.H. Braus, *Crystallization and preliminary X-ray analysis of 3-deoxy-D-arabino-heptulosonate-7-phosphate synthase (tyrosine inhibitable) from Saccharomyces cerevisiae.* Acta Crystallogr D Biol Crystallogr, 1999. **55**(Pt 9): p. 1586-8.

22. Webby, C.J., et al., *Crystallization and preliminary X-ray crystallographic analysis of 3-deoxy-D-arabino-heptulosonate-7-phosphate synthase from Mycobacterium tuberculosis.* Acta Crystallogr Sect F Struct Biol Cryst Commun, 2005. **61**(Pt 4): p. 403-6.

# CHAPTER 5

## An Electrospray MS-coupled Microfluidic Device for Sub-second Hydrogen/Deuterium Exchange Pulse-labelling Reveals Allosteric Effects in Enzyme Inhibition

***Adapted from*** *Lab on a Chip. 2013, special issue (10.1039/C3LC00007A)*

## 5.1 INTRODUCTION

With the emergence of 'soft' ionization techniques for mass spectrometry in the late 1980's microfluidics was quickly recognized as a means to link rapid, precise sample handling with the analytical power of mass spectrometry [1-5]. Electrospray is the soft ionization method most-often coupled to microfluidics owing mainly to the direct transfer from solution to the gas phase. Numerous Electrospray Coupled Microfluidic Devices (ECMDs) have been introduced using a range of substrates including polymer, silicon and glass, with the most common application being proteomics [6-11]. The intense academic interest in ECMDs has translated now to industry, and there are a growing number of commercial devices on the market for use in proteomics [12]. However, ECMDs remain underdeveloped for other applications to which they are ideally suited. Experiments to monitor protein structure, dynamics and function, for example, which are increasingly needed to support the shift to 'biologics' in the pharmaceutical industry, benefit greatly from implementation on an ECMD platform, but only a handful of such devices have been devised [13, 14].

In HDX experiments, analytes with solvent-exchangeable protons are exposed to $D_2O$ resulting in the incorporation of deuterium into the molecule. This process can be monitored by NMR or mass spectrometry, with mass spectrometry being the more versatile (though at times less informative) approach [15]. In the context of proteins, HDX is a measure of solvent accessibility and strength of hydrogen bonding (hydrogen bonds must break in order for exchange to occur) for 'backbone' amide protons [16]. Since secondary structure is maintained by a network of backbone hydrogen bonds, the occurrence of HDX (or rather the lack of it) can be used to identify regions of rigid secondary structure [17]. Additionally, the rate of exchange can be used as a quantitative or semi-quantitative measure of structural stability, more commonly understood as protein dynamics [18].

In an intact protein, HDX is observed by mass spectrometry as a shift to higher mass that occurs at a certain rate. This 'global' measurement is a facile way to predict overall protein structural stability and is particularly useful for characterizing the structural consequences of ligand binding [19]. However, in order to determine which *regions* of the protein are dynamic, it is necessary to fragment the labelled protein into peptides whose individual deuterium uptake levels can be linked back to their positions within the native structure. This fragmentation can be achieved after ionization using 'non-ergodic' techniques like electron capture dissociation ('top-down'), or before ionization by quenching the exchange process and digesting with an acid-resistant protease ('bottom-up') [17, 20]. Of these approaches, 'bottom-up' provides somewhat less spatial resolution, but is applicable to a much broader range of proteins and does not require expensive, specialized equipment. HDX experiments can be conducted in a continuous or pulse labelling regime. In the continuous regime, the protein is exposed to $D_2O$ for a variable length of time, allowing the rate of deuterium uptake to be measured. In pulse labelling experiments, a reaction involving the protein is initiated and allowed to progress for a variable time before exposure to a fixed-length $D_2O$ labelling pulse. This approach is suitable for following structural changes that occur during a reaction, most commonly protein folding [21-23]. Alternatively, pulse labelling might be used to reveal the structural changes associated with slow allosteric effects after ligand or inhibitor binding.

In this study, we introduce a microfluidic device that enables the complete workflow for bottom-up HDX pulse labelling experiments. The device incorporates a variable-position micromixer for adjustable reaction-time mixing, a static micromixer and delay volume generating a fixed 46 ms $D_2O$ labelling pulse, a subsequent mixer for HDX quenching and a pepsin-functionalized microreactor for efficient protein digestion prior to on-chip ESI. We use this device to investigate the structural changes that occur upon acylation of the beta lactamase enzyme TEM-1 by a covalent inhibitor. Our results reveal several rapid structural changes near the active site and more subtle changes that occur over several seconds in active-site remote regions.

## 5.2 EXPERIMENTAL

**5.2.1 Materials.** Pepsin agarose beads, high purity acetic acid ($\geq$ 99.7%), deuterium oxide ($D_2O$), ammonium bicarbonate (99.8%) and potassium clavulanate were purchased from Sigma (St. Louis, MO). Ultrapure water was generated in-house on a Millipore Milli-Q Advantage A10 system. Polyimide coated glass capillaries (O.D. 153 μm, I.D. 75 μm) were purchased from

Polymicro Technologies (Pheonix, AZ). Metal capillaries (O.D. 400 µm, I.D. 200 µm and O.D. 318 µm, I.D. 177.8 µm) and PTFE tubing (O.D. 1/16″, I.D. 400 µm and O.D. 1/16″, I.D. 205 µm) were supplied by McMaster-Carr (Aurora, OH). Standard 1/16″ Upchurch fittings were purchased from Scientific Products & Equipment (North York, ON). Blank poly(methyl methacrylate) or PMMA substrate was purchased from Professional Plastics (Orchard Park, NY) in rectangular block with dimension 8.9 cm x 3.8 cm x 0.3 cm. A dremel (Craftsman Co. Hoffman Estates, IL) was used to sharpen the metal capillary for ESI.

**5.2.2 Device Fabrication.** The microfluidic chip was fabricated from polymethyl methacrylate (PMMA) as described previously in details in chapter 2. Briefly, the microfluidic channels were etched on PMMA using a VersaLaser™ engraver (Universal Laser, Scottsdale, AZ) with a slightly defocussed laser to generate square channels that is described in details in Chapter 2. A proteolytic reactor surface was generated by etching closely spaced 30 µm deep channels in a hashed pattern within a rectangular area (25 mm x 5 mm). These micro channels generated a fine mesh of lines for the reactor bed where pepsin beads (average diameter 20 µm) were physically trapped in the grooves. Another blank PMMA block was used as a celling, forcing liquid entering the reactor through the pepsin-filled grooves [24]. Parafilm® was used as gasket to obtain liquid-tight seal between the two PMMA blocks. A custom built clamp was obtained from LAC Machine & Tooling Limited, ON to pressure-seal the microfluidic device. Connections to the outside world were made by melting metal capillaries into channels running off the side of the chip [25].

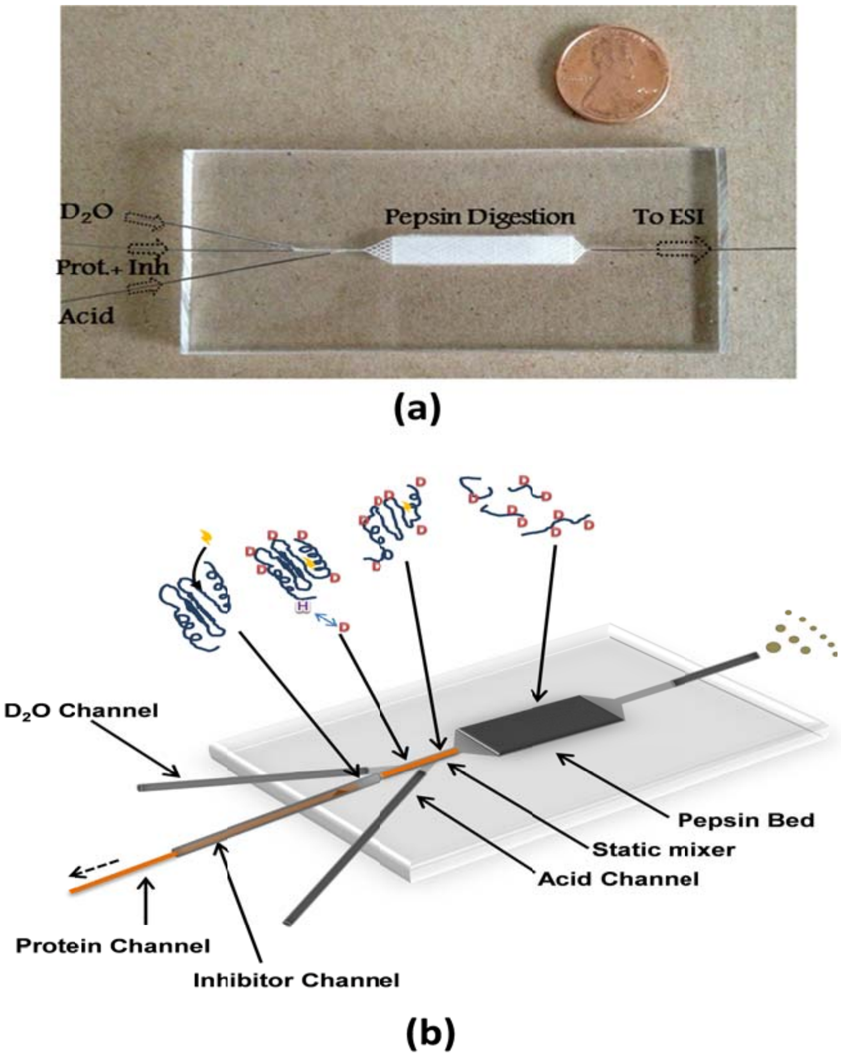

**Figure 5.1** The microfluidic device. (a) Annotated photograph with Canadian penny for size orientation. Arrows indicate direction of flow. (b) A schematic depiction of the device. Top cartoons show the chemical steps at each stage. From left to right: Inhibitor binding, HDX pulse label, HDX quenching, proteolysis and ESI. The centre channel incorporates a capillary mixer that allows a variable delay after mixing of protein and inhibitor via 'pullback' of the inner capillary (dotted arrow). The static mixer provides efficient mixing for the HDX pulse and acid quenching.

The device is shown in Figure 5.1. It consists of three inlet channels, the center one incorporating an adjustable position capillary mixer for variable-time incubation of TEM-1 with clavulanate from 128 ms to 9 s. $D_2O$ and acetic acid were mixed in using a 4 mm long sealed polyimide-coated glass capillary which acted to force reactant solutions together through the narrow regions between the capillary and the channel walls (maximum 7 μm). All fluids were infused into the microfluidic device using infusion pumps (Harvard, Holliston, MA) with standard Upchurch fittings.

**5.2.3 TEM-1 Purification.** TEM-1 purification has been described previously [26]. Briefly, *E. coli* BL21(DE3) carrying the plasmid pET24 a+ were grown overnight in Luria Bertani medium supplemented with 30 μg/ml kanamycin. Grown cultures were diluted 100-fold in Terrific Broth medium, containing 30 μg/ml kanamycin, 0.4 M D-Sorbitol and 2.5 mM betaine. Cells were grown by shaking at 37 ºC until Optical Density (at 600 nm) of 0.6 was reached. At this point TEM-1 over-expression was induced by adding isopropyl β-D-thiogalactopyranoside (IPTG) for a final concentration of 0.4 mM. Cells were made to over-express the protein overnight at 25 ºC. After pelleting the cells by centrifugation, the supernatant was collected. TEM-1 was purified by cation exchange as described previously [26].

**5.2.4 HDX Measurements.** HDX pulse labelling was carried out on TEM-1 using the microfluidic chip as a custom electrospray ionization (ESI) source. The chip was directly interfaced with a modified QSTAR® Elite hybrid quadrupole time-of-flight (QqTOF) mass spectrometer (Sciex, MDS Analytical Technologies, Concord, ON). 20 μM TEM-1 was mixed with potassium clavulanate (1:1) in the rapid mixing module of the device (pH 7.84). The position of the mixer in the mixing module was adjusted manually to control the incubation time. Using flow rates of 3μL/min for protein solution and 3 μL/min for potassium clavulanate, we were able to achieve mixing times from 128 ms to 9 s. A flow rate of 3μL/min for $D_2O$ facilitated a 46 ms $D_2O$ labelling pulse prior to a rapid HDX quenching by dropping the pH to 2.6 using a 4% acetic acid solution (pH 2.3) at 10 μL/min. Subsequent digestion of the labelled protein and transfer to ESI was achieved in approximately 6 s using the microfluidic reactor, resulting in undetectable back exchange of backbone protons (exchangeable protons on side chains and peptide N-termini undergo rapid back-exchange and are assumed to be 16% labelled, having equilibrated with the final solution $H_2O/D_2O$ ratio prior to electrospray).

**5.2.5 Mass Spectrometry.** ESI-MS experiments were carried out on a QStar Elite quadrupole time-of-flight (Q-TOF) instrument (MDS Analytical Technologies, Concord, ON, Canada) with a custom-built source assembly. A switch was used to simulate the presence of the commercial source. Optimal running conditions of +5000 V to +4800 V source, 60 V declustering potential, and focusing potential of 250 V were achieved through the positioning of the electrospray tip on a vertically adjustable stage. All analyses were carried out in positive ion mode and at acquisition rates of $1s^{-1}$. The samples were scanned over the 250–1500 *m/z* range.

**5.2.6. Data Analysis.** Data were analysed using an in-house built program introduced previously in Chapter 3 [13]. Briefly, HDX incorporation levels for each peptide were determined by fitting the observed isotopic distribution to a theoretical one generated by convolution of the natural isotope distribution with the deuterium label distribution associated with a particular level of exchange. A least-squares approach was used to determine which level of exchange (expressed as % label) agreed best with the observed isotopic distribution. Adjustments are made for the rapid equilibration of exchangeable protons on side-chains and the N-terminus with the final electrosprayed solution (which was 16% $D_2O$). Given the short length of the labelling pulse, HDX is expected to occur to a significant degree only in unstructured regions of the protein. We can therefore define an expected level of exchange $N_{\mathrm{loop}}$ for each peptide based on the number amides that are in a loop configuration in the crystal structure. Significant deviations from $N_{\mathrm{loop}}$ in the % label value suggest changes in structure and/or dynamics compared to the crystal structure (in this case in response to acylation).

## 5.3 RESULTS AND DISCUSSIONS

**5.3.1 Device Performance.** In bottom-up HDX pulse labeling experiments, there are a number of important metrics for performance. From the perspective of microfluidics, the first of these is mixing efficiency and control. The capillary mixer used to initiate the acylation of TEM-1 has been extensively tested in earlier work [25, 27, 28] and is known to provide complete mixing within 5 ms. The static mixer used in the next two mixing steps ($D_2O$ and 4% acetic acid) is less well characterized, but based on the predicted time for a mean displacement of 7 μm for protons ($D \cong 5 \times 10^{-9}\ m^2s^{-1}$ after a crude adjustment for the presence of 16% $D_2O$), complete mixing of should occur within 17 ms, which is well within the residence time of the mixer (approx. 25 ms). In practice, no experimental artifacts that might be attributed to inefficient or poorly controlled mixing were observed. Poor mixing of $D_2O$, for example, would have resulted in lower than expected deuteration levels on all peptides while poor mixing of acid would have resulted in rapid back exchange and inactivation of pepsin in the reactor well.

The second critical performance factor is spatial resolution, which in bottom-up experiments is effectively a measure of digestion efficiency. In general, the more peptides generated in the digestion step, the more specific the analysis in terms of where on the protein deuterium uptake is occurring. Our device provides relatively low digestion efficiency compared to conventional LC-based techniques, but operates at a much faster rate (≤ 6 s) which greatly reduces back-exchange. Ultimately the analysis was conducted with 28 peptides corresponding to 65% sequence coverage and an average spatial resolution of 8.5 residues. While there is room for improvement of these numbers, this level of spatial resolution was more than sufficient to provide some interesting insights into the changes in TEM-1 dynamics that occur as a consequence of inhibitory acylation. A complete list of peptides is provided in table 5.1.

**5.3.2 Changes in TEM-1 Dynamics on Acylation.** The TEM-1/clavulanate system was selected to demonstrate our apparatus in part because of the putative critical role of dynamics in the inhibitory mechanism [26]. In our pulse labeling experiments, the raw data are in the form of isotopic distributions associated with each peptide (Figure 5.2). Changes in these distributions are linked to the amount of deuterium acquired by the peptide, which we express as '% labeled' in order to normalize for the number of available sites on peptides of different length. Figure 5.2 shows time-dependent profiles for four peptides, each representing one of the behaviors observed in the broader data set.

**Table 5.1: All observed peptides with HDX levels, pre-mixing and two time-points post-mixing with clavulanate.**

| Sequence | position | Free enzyme 128 ms (% labeled) | Acyl-enzyme 128 ms (% labeled) | Acyl-enzyme 9.0 s (% labeled) |
|---|---|---|---|---|
| HPETL | 001-005 | 15 | 15 | 15 |
| HPETLVKVKDAEDQLGARVGY | 001-021 | 3 | 6 | 22 |
| VKVKDAEDQLGARVGY | 006-021 | 5 | 19 | 19 |
| VKVKDAEDQLGARVGY | 006-021 | 4.5 | 19 | 19 |
| AEDQLGARVGYI | 011-022 | 2 | 6 | 27 |
| IELDLNSGKILESF | 022-035 | 14 | 12 | 6 |
| LDLN | 024-027 | 10 | 14 | 31 |
| NSGKILESFRPEE | 027-039 | 6 | 4 | 4 |
| SRVDAGQEQLGRRIHYSQNDL | 057-077 | 15 | 11 | 11 |
| GRRIHYSQNDL | 067-077 | 14 | 20 | 20 |
| SDNTAANL | 105-112 | 4 | 7 | 7 |
| SDNTAANLLLTTI | 105-117 | 9 | 8 | 5.5 |
| TTIGGPKELTAF | 115-126 | 7 | 3 | 3 |
| FLHNMGDHVTRL | 126-137 | 16 | 10 | 10 |
| FLHNMGDHVTRL | 126-137 | 12 | 8 | 8 |
| HNMG | 128-131 | 10 | 7 | 7 |
| DRWEPEL | 138-144 | 6 | 6 | 6 |
| RKLLTGEL | 166-173 | 11 | 11 | 20 |
| IDWMEA | 183-188 | 2 | 7 | 7 |
| DKVAGPLL | 189-196 | 0 | 1 | 7 |
| PAGWFIA | 201-207 | 2 | 4 | 4 |
| GWFIADKSG | 203-211 | 18 | 18 | 18 |
| GWFIADKSGAGERGSRGIIAALGPDGKPSRIVV | 203-235 | 6 | 12 | 12 |
| FIADKSGAGERGSRGIIAA | 205-223 | 5 | 10 | 10 |
| YTTG | 237-240 | 6 | 6 | 6 |
| DERNRQIAE | 246-254 | 8 | 5 | 5 |

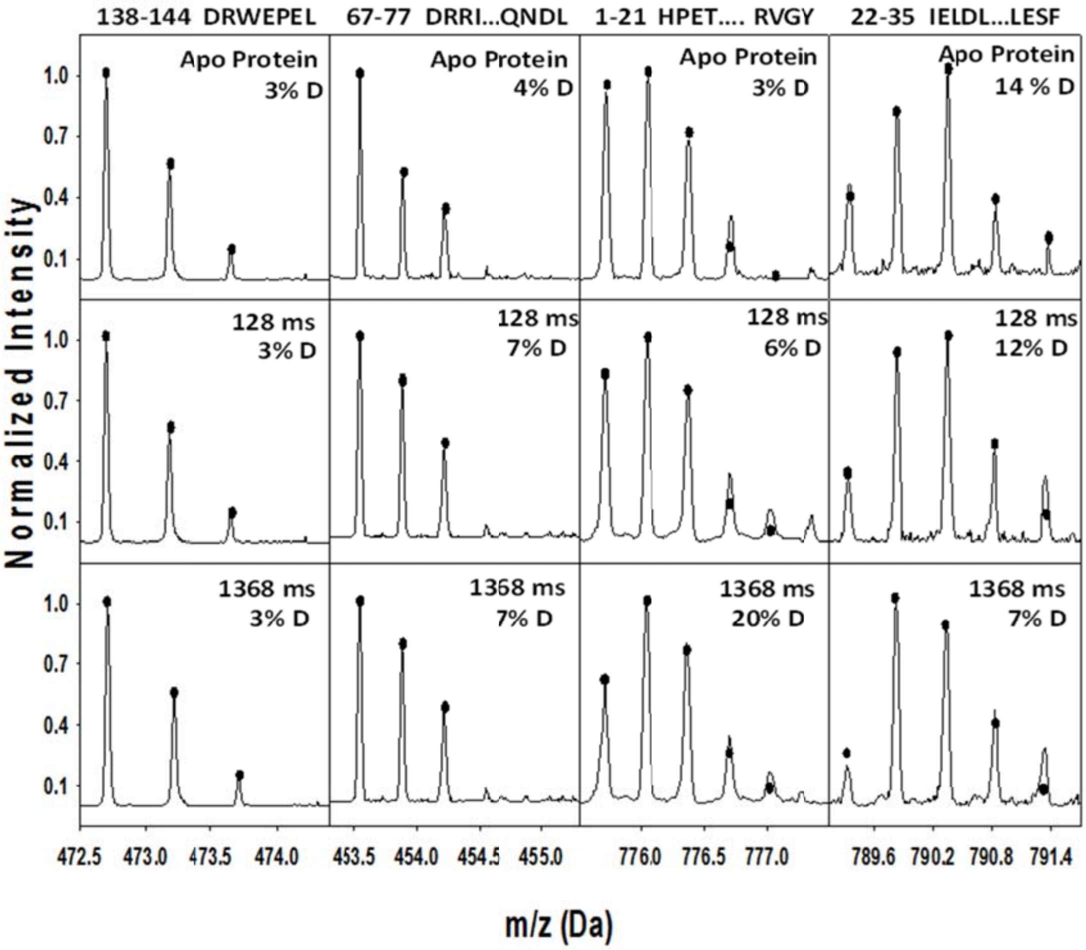

**Figure 5.2.** Typical time-dependent changes in isotopic distribution for four TEM-1 peptides after acylation by clavulanate. Dots represent the best fit theoretical distributions from which the '% labeled' (%D) values were extracted. These peptides exhibit each of the 4 behaviors observed for all peptides. From left to right: No change, rapid increase upon acylation, slow increase after acylation and slow decrease after acylation.

A number of peptides did not exhibit any change in deuterium uptake immediately following acylation nor up to 9 s after acylation. These peptides denote regions of TEM-1 that do not undergo a significant change in dynamics or solvent accessibility upon acylation of the protein by clavulanate. The majority of peptides were observed to undergo a significant, rapid change in deuterium uptake upon acylation, with increases and decreases in roughly equal proportion. A rapid increase in deuterium uptake would imply that acylation makes the region in question more dynamic, while a decrease in uptake indicates a 'tightening up' of the structure or a decrease in solvent accessibility due to the presence of inhibitor. Most interesting, however, are the peptides that undergo slow changes in deuterium uptake after acylation. These peptides may correspond to regions of the protein that undergo functionally relevant allosteric transitions upon inhibition.

These behaviors can be analyzed kinetically to determine the rate at which the changes in dynamics occur after acylation. Kinetic plots for three peptides are shown in Figure 5.3. The dotted line shows the expected level of exchange based on the crystal structure, $N_{\mathrm{loop}}$. Error bars are based on up to four transients, depending on the number of data sets in which the peptide was observed. Rates extracted from single exponential fits to the data are identical, indicating that the allosteric changes in dynamics occur at more-or-less the same rate after acylation.

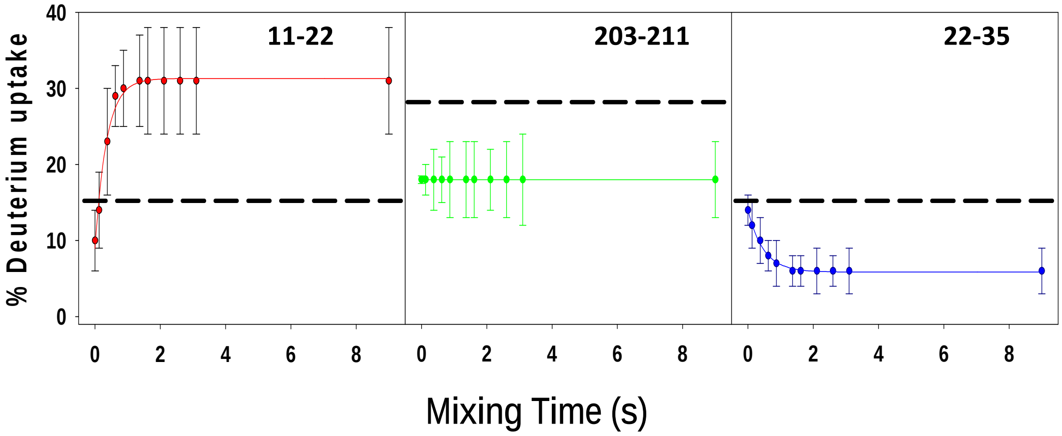

**Figure 5.3.** A kinetic analysis of the changes in dynamics associated with acylation. The dotted line represents the expected level of exchange based on the crystal structure. Error bars are based on up to 4 transients, depending on the number of data sets and time-point in which the peptide was observed.

Ultimately, the pulse labeling data can be mapped onto the crystal structure to rationalize the observed structural and dynamic changes. Figure 5.4 (a) shows the changes that take place immediately on binding. Red indicates an increase in HDX upon acylation, blue a decrease and green denotes no change. One general observation of note is that the majority of peptides that exhibit exclusively rapid changes are in structured regions of the protein core, particularly the beta sheet that lies at the 'top' of the active site in Figure 5.4.

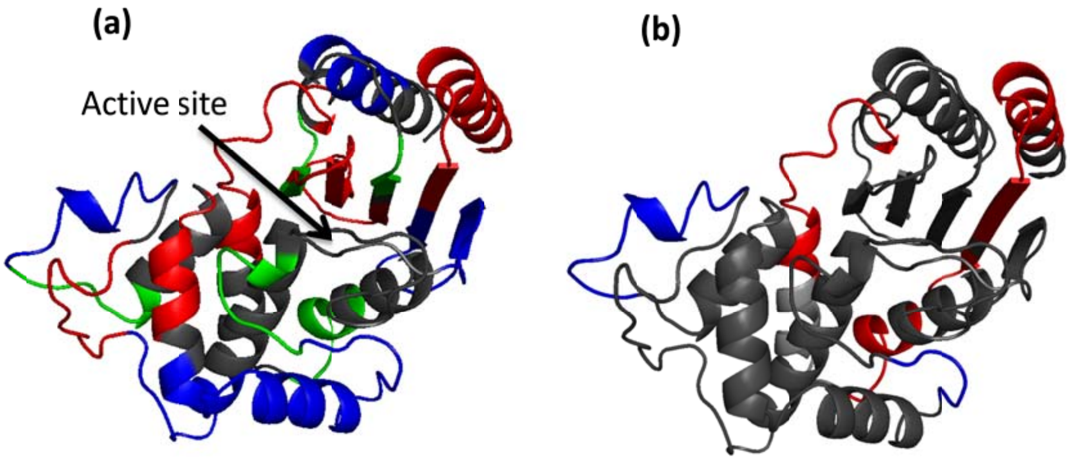

**Figure 5.4.** Changes in TEM-1 conformational dynamics upon acylation as indicated by changes in deuterium uptake. (a) Immediately upon acylation. (b) Over time after acylation. Red indicates an increase in deuterium uptake, blue indicates a decrease and green indicates no change. In (a), grey regions indicate regions where no peptides were detected. In (b) all regions that do not exhibit a slow change in deuterium uptake are grey.

Interestingly, one of the beta sheet regions showing a substantial increase in dynamics on clavulanate binding includes Arg244, which is directly involved in the inhibitory mechanism [29]. At the same time, the region that houses Asn276, a residue that acts to correctly position Arg244 by hydrogen bonding to its side-chain becomes more structured. These results suggest that repositioning of Arg244 for inhibition is achieved both by 'loosening' the adjacent beta strand and by locking Asn276 in place [30].

More distant from the active site, there are a number of peptides that show an early increase in deuterium uptake, but many of these peptides also exhibit a slow phase in which deuterium uptake rises over several seconds. These peptides are highlighted in Figure 5.4(b). A significant proportion of these peptides are located at the periphery of the protein, away from the active site. This suggests that the changes observed may be related to allosteric effects associated with acylation by clavulanate. Support for this rationalization is provided by high frequency random mutagenesis studies, in which a number of peripheral mutations have been shown to strongly influence enzyme activity [31, 32]. This includes mutations at positions 42, 104 and 164, all of which are identified in our data as being in or close to regions that undergo 'allosteric' changes in dynamics due to acylation.

## 5.4 CONCLUSIONS

In summary, we have introduced an integrated microfluidic device that houses the complete workflow for 'bottom-up' HDX pulse labelling experiments. This device is complementary to a continuous labelling HDX chip introduced earlier [13] and is uniquely well suited to probe allosteric changes occurring as a consequence of covalent modification (*e.g.* phosphorylation, covalent inhibition *etc*.) or ligand binding. To demonstrate the utility of the approach, we applied our device to covalent inhibition of the beta-lactamase enzyme TEM-1 by clavulanate. Even in the straightforward and inexhaustive experiments conducted, we were able to measure changes in structure and dynamics directly linked to inhibition and to identify peripheral regions of the protein where allosteric effects occur, many of which contain residues known to influence catalytic efficiency. To our knowledge, these data represent the first experimental analysis of TEM-1 acyl-enzyme dynamics and provide an entirely new way to predict allosteric modulation of catalytic activity. Ultimately, we expect this approach will prove a facile and powerful tool for understanding the structural and dynamic changes that accompany functional processes in proteins.

# REFERENCES

1. Xue, Q.F., et al., *Multichannel microchip electrospray mass spectrometry.* Anal. Chem., 1997. **69**(3): p. 426-430.
2. Figeys, D. and R. Aebersold, *Nanoflow solvent gradient delivery from a microfabricated device for protein identifications by electrospray ionization mass spectrometry.* Anal. Chem., 1998. **70**(18): p. 3721-3727.
3. Yamashita, M. and J.B. Fenn, *Electrospray ion-source - Another Variation on the Free-Jet Theme.* J. Phys. Chem., 1984. **88**(20): p. 4451-4459.
4. Koichi, T., et al., *Protein and polymer analyses up to m/z 100 000 by laser ionization time-of-flight mass spectrometry.* Rapid Commun. Mass Sp., 1988. **2**(8): p. 151-153.
5. Karas, M. and F. Hillenkamp, *Laser desorption ionization of proteins with molecular masses exceeding 10000 daltons.* Anal. Chem., 1988. **60**(20): p. 2299-2301.
6. Figeys, D., *Adapting arrays and lab-on-a-chip technology for proteomics.* Proteomics, 2002. **2**(4): p. 373-382.
7. Jeonghoon, L., A.S. Steven, and K.M. Kermit, *Microfluidic chips for mass spectrometry-based proteomics.* J. Mass. Spectrom., 2009. **44**(5): p. 579-593.
8. Freire, S.L.S. and A.R. Wheeler, *Proteome-on-a-chip: Mirage, or on the horizon?* Lab Chip, 2006. **6**(11): p. 1415-1423.
9. Blankenstein, G. and U.D. Larsen, *Modular concept of a laboratory on a chip for chemical and biochemical analysis.* Biosens. Bioelectron., 1998. **13**(3-4): p. 427-438.
10. Bedair, M.F. and R.D. Oleschuk, *Fabrication of porous polymer monoliths in polymeric microfluidic chips as an electrospray emitter for direct coupling to mass spectrometry.* Analytical Chemistry, 2006. **78**(4): p. 1130-1138.
11. Pinto, D.M., Y.B. Ning, and D. Figeys, *An enhanced microfluidic chip coupled to an electrospray Qstar mass spectrometer for protein identification.* Electrophoresis, 2000. **21**(1): p. 181-190.
12. Yin, H.F. and K. Killeen, *The fundamental aspects and applications of Agilent HPLC-Chip.* J. Sep. Sci., 2007. **30**(10): p. 1427-1434.

13. Rob, T., et al., *Measuring Dynamics in Weakly Structured Regions of Proteins Using Microfluidics-Enabled Subsecond H/D Exchange Mass Spectrometry.* Anal. Chem., 2012. **84**(8): p. 3771-3779.

14. Landreh, M., et al., *New developments in protein structure-function analysis by MS and use of hydrogen-deuterium exchange microfluidics.* Febs J., 2011. **278**(20): p. 3815-3821.

15. Englander, S.W., *Protein folding intermediates and pathways studied by hydrogen exchange.* Annu. Rev. Biophys. Biomol. Struct., 2000. **29**: p. 213-238.

16. Konermann, L., J. Pan, and Y.-H. Liu, *Hydrogen exchange mass spectrometry for studying protein structure and dynamics.* Chemical Society Reviews, 2011. **40**(3): p. 1224-1234.

17. Zhang, Z.Q. and D.L. Smith, *Determination of Amide Hydrogen Exchange by Mass Spectrometry - A New Tool for Protein Structure Elucidation.* Protein Sci., 1993. **2**(4): p. 522-531.

18. Hollien, J. and S. Marqusee, *Structural distribution of stability in a thermophilic enzyme.* P. Natl. Acad. Sci. USA, 1999. **96**(24): p. 13674-13678.

19. Chalmers, M.J., et al., *Probing protein ligand interactions by automated hydrogen/deuterium exchange mass spectrometry.* Anal. Chem., 2006. **78**(4): p. 1005-1014.

20. Pan, J., et al., *Electron capture dissociation of electrosprayed protein ions for spatially resolved hydrogen exchange measurements.* J. Am. Chem. Soc., 2008. **130**(35): p. 11574-11575.

21. Pan, J.X., et al., *Characterizing Short-Lived Protein Folding Intermediates by Top-Down Hydrogen Exchange Mass Spectrometry.* Anal. Chem., 2010. **82**(20): p. 8591-8597.

22. Konermann, L. and D.A. Simmons, *Protein-folding kinetics and mechanisms studied by pulse-labeling and mass spectrometry.* Mass Spectrom. Rev., 2003. **22**(1): p. 1-26.

23. Simmons, D.A. and L. Konermann, *Characterization of Transient Protein Folding Intermediates during Myoglobin Reconstitution by Time-Resolved Electrospray Mass Spectrometry with On-Line Isotopic Pulse Labeling.* Biochemistry, 2002. **41**: p. 1906-1914.

24. Liuni, P., T. Rob, and D.J. Wilson, *A microfluidic reactor for rapid, low-pressure proteolysis with on-chip electrospray ionization.* Rapid Commun. Mass Spectrom., 2010. **24**(3): p. 315-320.

25. Rob, T. and D.J. Wilson, *A Versatile Microfluidic Chip for Millisecond Time-scale Kinetic Studies by Electrospray Mass Spectrometry.* J. Am. Soc. Mass Spectr., 2009. **20**(1): p. 124 - 130.

26. Meroueh, S.O., et al., *Molecular dynamics at the root of expansion of function in the M69L inhibitor-resistant TEM beta-lactamase from Escherichia coli.* J. Am. Chem. Soc., 2002. **124**(32): p. 9422-9430.

27. Liuni, P., A. Jeganathan, and D.J. Wilson, *Conformer Selection and Intensified Dynamics During Catalytic Turnover in Chymotrypsin.* Angew. Chem. Int. Ed., 2012. **51**(38): p. 9666-9669.

28. Wilson, D.J. and L. Konermann, *A Capillary Mixer with Adjustable Reaction Chamber Volume for Millisecond Time-Resolved Studies by Electrospray Mass Spectrometry.* Anal. Chem., 2003. **75**: p. 6408 - 6414.

29. Delaire, M., et al., *Site-directed mutagenesis at the active-site of escherichia-coli TEM-1 beta-lactamase - suicide inhibitor - resistant mustant reveals the role of arginine-244 and methionine-69 in catalysis.* J. Biol. Chem., 1992. **267**(29): p. 20600-20606.

30. Swaren, P., et al., *X-ray structure of the Asn276Asp variant of the Escherichia coli TEM-1 beta-lactamase: Direct observation of electrostatic modulation in resistance to inactivation by clavulanic acid.* Biochemistry, 1999. **38**(30): p. 9570-9576.

31. Zaccolo, M. and E. Gherardi, *The effect of high-frequency random mutagenesis on in vitro protein evolution: A study on TEM-1 beta-lactamase.* J. Mol. Biol., 1999. **285**(2): p. 775-783.

32. Orencia, M.C., et al., *Predicting the emergence of antibiotic resistance by directed evolution and structural analysis.* Nat. Struct. Biol., 2001. **8**(3): p. 238-242.

# CHAPTER 6

# Application of Microfluidics to the Prediction of Allosteric Sites in TEM-1 Beta-lactamase

## 6.1 INTRODUCTION

Antibiotic resistance is currently a major health concern in treating infectious diseases. The production of Beta-lactamase enzymes (β-lactamases) is the main cause of this resistance which act by destroying the beta-lactam structure of antibiotics before they reach the bacterial target [1, 2]. Clinical usages of antibiotics are continuously challenged with the emergences of new beta lactamases, sometimes as soon as the new antibiotics are introduced. To address this issue, enormous efforts scientists have been made to investigate β-lactamase structure and mechanisms for the development of uncleavable drugs and/or inhibitors. β-lactam antibiotics contain a beta lactam ring which is the preferred target of beta lactamases, rendering the drugs inert upon hydrolysis (Figure 6.1) [3, 4]. β-lactam antibiotics can be classified into two major categories: first generation and second generation antibiotics (also known as extended structure antibiotics) that contain a five member ring and six member ring along a beta lactam core. First generation antibiotics are extremely susceptible targets of most of the naturally evolved β-lactamases while the extended structures exhibit better effectiveness against same β-lactamases. For a better clinical performance of these antibiotics, they are usually combined with a β-lactamases inhibitor [5, 6]. However, inhibitor usage has also been challenge due to the emergence of inhibitor resistance.

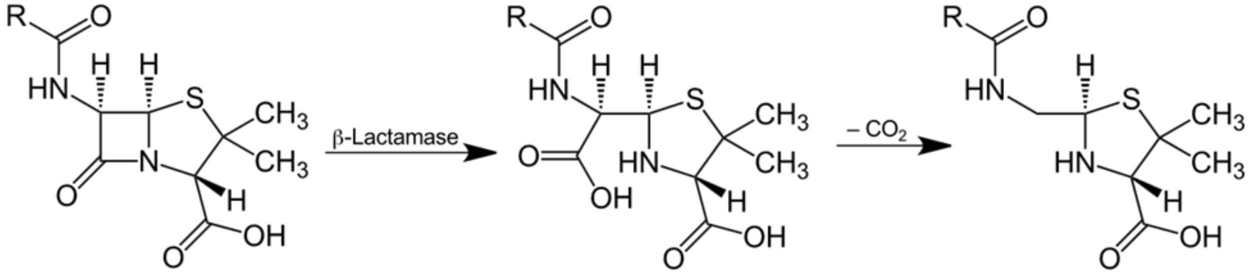

**Figure 6.1.** Inactivation mechanism of β-lactam ring by β-lactamases *via* acylation and deacy lation.

The β-lactamases are traditionally classified based on either functional characteristics or their amino acid sequence, the latter of which is known as molecular classification. Based on conserved and distinguishing amino acid motifs, β-lactamases are classified into four molecular classes, A, B, C, and D. Enzymes which utilize an serine residue for hydrolysing β-lactam ring whereas class B are metalloenzymes which require at least one active-site divalent zinc ions to facilitate β-lactam hydrolysis [3, 7]. In 1995 Bush *et al*. proposed another functional classification scheme that takes into account substrate and inhibitor profiles in an attempt to group the enzymes in ways that can be correlated with their phenotype in clinical isolates [8]. TEM-1 is one of the most commonly encountered antibiotic resistant species causeing up to 90% of ampicillin resistance in *E. coli*. TEM-1 is classified as class A broad-spectrum β-lactamases according to Molecular classification, while it belongs to functional subgroup 2b. It readily hydrolyzes penicillins and early cephalosporins, such as cephaloridine and cephalothin to inactivate them while the resistance can be strongly inhibited by clavulanic acid and tazobactam.

Although TEM-1 beta-lactamase is one of the most studied enzymes, its catalytic mechanism still remains controversial [9]. Numerous independent approaches have been taken to resolve this issue, for instance by ultrahigh resolution X-ray crystallography or molecular dynamics simulations. Some of these studies afforded a detailed view of the structure, dynamics and hydrogen bonding networks of TEM-1 which provided details about the acylation mechanism. The acylation of TEM-1 by β-lactam compound is modelled as a two-step mechanism where the first step involves activation of catalytic serine residue (Ser70) to cleave the lactam ring [1, 10-12] . A 70 SXXK motif is identified as the essential component in most of the β-lactamases, demonstrating that the close proximity of the Ser (S) and Lys (K) are crucial for acylation [13]. A dynamic loop has also been identified where the Glu166 positions an active site water molecule which forms bond with Ser70 [14, 15]. This water molecule does not exchange with bulk solvent, emphasizing its structural and catalytic relevance. In the presence of the substrate Ser130, Ser235, and Arg244 directly interact with the beta-lactam carboxylate *via* H-bonds, whereas the Lys234 ammonium group and Ser238 hydroxyl group have only an electrostatic influence [16]. However, these interactions together with other specific contacts result in a very short distance (approximately 3 $^{o}$A) between the attacking hydroxyl group of Ser70 and the β-lactam ring carbonyl group, which is a favourable orientation for nucleophilic attack [14, 17-19].

TEM-1 has shown a perplexing functional flexibility *via* 'natural' evolution in response to the introduction of novel drugs derived from these antibiotics. Since its discovery in the 1960s, over 170 variants of TEM-1 with different amino acid sequences and often resistance phenotypes that include extended structure β-lactamases (ESBL) as well - have been isolated in hospitals and clinics worldwide [20-22] However, most commonly encountered single amino acid substitutions are observed at positions 104, 164, 237- 240 both as individual and as combinatorial substitutions (associated with the ESBL phenotype) [23-25]. In bacteria and viruses where the spontaneous mutation rate is often high and the generation time is short, the rapid emergence of drug –resistant organisms has created a problem for the use and development of antibiotics. In response to the selective pressure of drug exposure amino acid substitutions that alter the specificity of the drug target accumulate and confer a selective advantage when the antibiotic is encountered [21, 26]. A puzzling phenomenon has been the accumulation of additional mutations that do not appear to confer a selective advantage by altering substrate specificity. A plausible hypothesis is that these secondary mutations compensate for the defects in catalytic activity or enzyme stability arising from specificity altering primary mutations.

This work demonstrates an application of the HDX pulse labelling microfluidic device that was introduced earlier in chapter 5. Following a parallel experimental approach, we use this device to compare the structural changes and time dependent allostery that occur on the beta lactamase enzyme TEM-1 upon binding to its covalent inhibitor, a good substrate and a poor substrate. Our results show that TEM-1 responds differently towards its different substrates or inhibitor which is expected but their highly dynamic regions carries the residues that are either important sites for its biological function or where the mutation occurs naturally. This remarkable correlation demonstrates the potential of the device in predicting possible sites of functionally relevant mutations.

## 6.2 EXPERIMENTAL

**6.2.1 Materials**. Ampicillin, cephalexin, potassium clavulanate, pepsin agarose beads, high purity acetic acid (≥ 99.7%), deuterium oxide ($D_2O$), ammonium bicarbonate (99.8%) and all other chemicals were obtained from Sigma (St. Louis, MO). Polyimide coated glass capillaries (O.D. 153 μm, I.D. 75 μm) were purchased from Polymicro Technologies (Pheonix, AZ). All metal capillaries and PTFE tubings were purchased from McMaster-Carr (Aurora, OH). Standard 1/16″ fittings were purchased from IDEX Health & Science (Oak Harbor, WA). Precut rectangular blocks (8.9 cm x 3.8 cm x 0.3) cm of blank poly(methyl methacrylate) or PMMA substrate was purchased from Professional Plastics (Orchard Park, NY).

**6.2.2 Microfluidic Device Fabrication**. Device fabrication has been discussed in details in chapter 5. Briefly, we followed the exact fabrication protocol but instead of a 4mm long closed polyimide-coated glass capillary, we have used a 4 mm long closed metal capillary (O.D. 153 μm) as a static mixer to ensure efficient mixing of holo protein and $D_2O$ within a small volume of ˜7 nL. Another metal capillary was added 6 mm downstream of the $D_2O$ channel to introduce acid for quenching the HDX reaction before transferring the solution to proteolytic module.

**6.2.3 TEM-1 purification.** TEM-1 protein was purified following the same purification protocol that has been described in Chapter 5.

**6.2.4 H/D Exchange Measurements**. HDX studies were carried out with TEM-1 using the pulse labelling microfluidic chip as custom electrospray ionization (ESI) source keeping identical front end mass spectrometer condition that had been described in Chapter 5. 100 μM

TEM-1 (pH 7.92) was mixed with one of its good substrate ampicillin (1:1) in the variable position mixing module of the device. Flow rates of 3μL/min for protein solution and 3 μL/min for Ampicillin enabled us to modulate mixing times from 128 ms to 10 sec. In separate experiments, cephalexin or potassium clavulanate was used instead of ampicillin. All other experimental parameters were identical to the parameters used in experimental section of chapter 5 and same approach was applied in data analysis as well.

## 6.3 RESULTS AND DISCUSSIONS.

In Chapter 5, we have demonstrated the potential of the pulse labeling device in monitoring allosteric changes that enabled us to detect time dependent change in dynamics of TEM-1/clavulanate system. We have now extended that work to measure differential allosteric behavior of TEM-1 in response to three different ligands: ampicillin (a good substrate), cephalexin (poor substrate) and K-clavulanate (inhibitor) [20, 23]. Ampicillin is a very good substrate of TEM-1 that readily undergoes hydrolysis with an extremely fast turnover rate (~$10^8$) whereas hydrolysis of cephalexin is relatively slower suggesting that there might be significant differences in their dynamics in the pre-acylation step [14, 27]. Since clavulanate does not undergo hydrolysis but shows allostery, the observed dynamics of TEM-1/cephalexin and TEM-1/ampicillin systems were compared with a refined data set of TEM-1/clavulanate system. The observed isotopic distributions were analyzed following the same protocol that has been discussed in details in results and discussion section of Chapter 5. We have adopted same coloring scheme to map the dynamic changes on to the crystal structure but instead of 1BTL (ligand free) we have used 1FQG crystal structure which is a substrate bound structure of TEM-1.

As expected, TEM-1 demonstrates very different conformational behavior towards its substrates and inhibitor. In some cases, the changes in deuterium distributions by observed peptides in three different systems are somewhat similar. However, there are some key regions that show opposite behaviors (in terms of ‘tightening’ or ‘loosening’ of structure) in deuterium uptake either after immediate binding (acylation) or 10 s after acylation. Interestingly, most of these regions correspond to the functional regions of the enzyme that are relevant to its catalytic activity. The structural changes that occur in three different systems of TEM-1 are compared by analyzing the kinetics of changes in dynamics, i.e. how fast the dynamics are changing in response to ligand binding. Kinetic plots of peptides under the three different system conditions are compared to determine the rate at which they respond towards the ligands. Kinetic plots for three important peptides are shown in Figure 6.2, 6.3 and 6.4. Additionally, the observed deuterium uptakes are listed on table 6.1, 6.2 and 6.3.

The most interesting behavior was exhibited by the peptide ‘DRWEPEL’ which is considered as a dynamic active loop and situated around the active site periphery (Figure 6.2 a). This peptide contains the active residue Glu164 that is involved in acylation mechanism [20, 23]. The peptide does not experience any structural change upon binding to inhibitor, but undergoes rapid fluctuation after binding as well show allosteric interactions to ampicillin or cephalexin. Surprisingly, in case of the poor substrate cephalexin, the observed deuterium level is 33% (maximum D uptake observed in this experiment) but with a slower rate while it takes only 12% deuterium with an abrupt rate for the good substrate ampicillin.

**Table 6.1: All observed peptides with HDX levels, pre-mixing and two time-points post-mixing with ampicillin.**

| Sequence | position | Free enzyme 128 ms (% labeled) | Acyl-enzyme 128 ms (% labeled) | Acyl-enzyme 10.0 s (% labeled) |
|---|---|---|---|---|
| HPETL | 026-030 | 10 | 15 | 33 |
| HPETLVKVKDAEDQLGARVG Y | 026-046 | 1 | 15 | 33 |
| SFRPEE | 059-064 | 0 | 8 | 8 |
| VLLCGAVLSRVDA | 074-086 | 0.05 | 16 | 32 |
| SRVDAGQEQLGRRIHYSQNDL | 082-102 | 10 | 2.5 | 2 |
| SDNTANLLLTTI | 130-142 | 0 | 0 | 0 |
| ANLLLTTI TTIGGPKEL | 135-148 | 0 | 2 | 6 |
| DRWEPEL | 161-167 | 0 | 12 | 12 |
| LRKLLTGELLTLASRQQLIDWE | 188-210 | 12 | 0 | 0 |
| ATTLRKLLTG | 185-194 | 0 | 5 | 28 |
| RKLLTGEL | 191-198 | 5 | 15 | 33 |
| RKLLTGELL | 191-199 | 5 | 12 | 33 |
| IDWMEA DKVAGPLLRSALPAGW | 208-229 | 2 | 16 | 16 |
| DKVAGPLL | 214-221 | 2 | 9 | 24 |
| GWFIADKSGAGERGSRGIIA ALGPDGKPSRIVV | 228-260 | 6 | 12 | 12 |
| FIADKSGAGERGSRGIIAALG | 230-248 | 0 | 8 | 33 |
| IAEIGAS | 275-281 | 0 | 16 | 18 |
| IGASL | 280-284 | 0 | 6 | 33 |

**Table 6.2: All observed peptides with HDX levels, pre-mixing and two time-points post-mixing with cephalexin.**

| Sequence | position | Free enzyme 128 ms (% labeled) | Acyl-enzyme 128 ms (% labeled) | Acyl-enzyme 10.0 s (% labeled) |
|---|---|---|---|---|
| HPETL | 026-030 | 10 | 10 | 30 |
| HPETLVKVKDAEDQLGARVG Y | 026-046 | 1 | 3 | 10 |
| SFRPEE | 059-064 | 0 | 0 | 30 |
| VLLCGAVLSRVDA | 074-086 | 0.05 | 1 | 32 |
| SRVDAGQEQLGRRIHYSQNDL | 082-102 | 10 | 8 | 2 |
| SDNTANLLLTTI | 130-142 | 0 | 0 | 0 |
| ANLLLTTI TTIGGPKEL | 135-148 | 0 | 0 | 18 |
| DRWEPEL | 161-167 | 0 | 0 | 33 |
| LRKLLTGELLTLASRQQLIDWE | 188-210 | 12 | 10 | 2 |
| ATTLRKLLTG | 185-194 | 0 | 10 | 10 |
| RKLLTGEL | 191-198 | 5 | 5 | 33 |
| RKLLTGELL | 191-199 | 5 | 5 | 33 |
| IDWMEA DKVAGPLLRSALPAGW | 208-229 | 2 | 7 | 7 |
| DKVAGPLL | 214-221 | 2 | 8 | 20 |
| GWFIADKSGAGERGSRGIIA ALGPDGKPSRIVV | 228-260 | 6 | 12 | 12 |
| FIADKSGAGERGSRGIIAALG | 230-248 | 0 | 0 | 7 |
| IAEIGAS | 275-281 | 0 | 0 | 0 |
| IGASL | 280-284 | 0 | 0 | 33 |

**Table 6.3: All observed peptides with HDX levels, pre-mixing and two time-points post-mixing with clavulanate.**

| Sequence | position | Free enzyme 128 ms (% labeled) | Acyl-enzyme 128 ms (% labeled) | Acyl-enzyme 10.0 s (% labeled) |
|---|---|---|---|---|
| HPETL | 026-030 | 10 | 10 | 30 |
| HPETLVKVKDAEDQLGARVG Y | 026-046 | 1 | 3 | 22 |
| SFRPEE | 059-064 | 0 | 0 | 0 |
| VLLCGAVLSRVDA | 074-086 | 0.05 | 0 | 0 |
| SRVDAGQEQLGRRIHYSQNDL | 082-102 | 10 | 2 | 2 |
| SDNTANLLLTTI | 130-142 | 0 | 0 | 0 |
| ANLLLTTI TTIGGPKEL | 135-148 | 0 | 0 | 0 |
| DRWEPEL | 161-167 | 0 | 0 | 33 |
| LRKLLTGELLTLASRQQLIDWE | 188-210 | 12 | 12 | 12 |
| ATTLRKLLTG | 185-194 | 0 | 0 | 23 |
| RKLLTGEL | 191-198 | 5 | 5 | 10 |
| RKLLTGELL | 191-199 | 5 | 5 | 10 |
| IDWMEA DKVAGPLLRSALPAGW | 208-229 | 2 | 7 | 7 |
| DKVAGPLL | 214-221 | 2 | 8 | 20 |
| GWFIADKSGAGERGSRGIIA ALGPDGKPSRIVV | 228-260 | 6 | 12 | 12 |
| FIADKSGAGERGSRGIIAALG | 230-248 | 0 | 0 | 0 |
| IAEIGAS | 275-281 | 0 | 0 | 0 |
| IGASL | 280-284 | 0 | 0 | 0 |

**161 – 167 DRWEPEL**

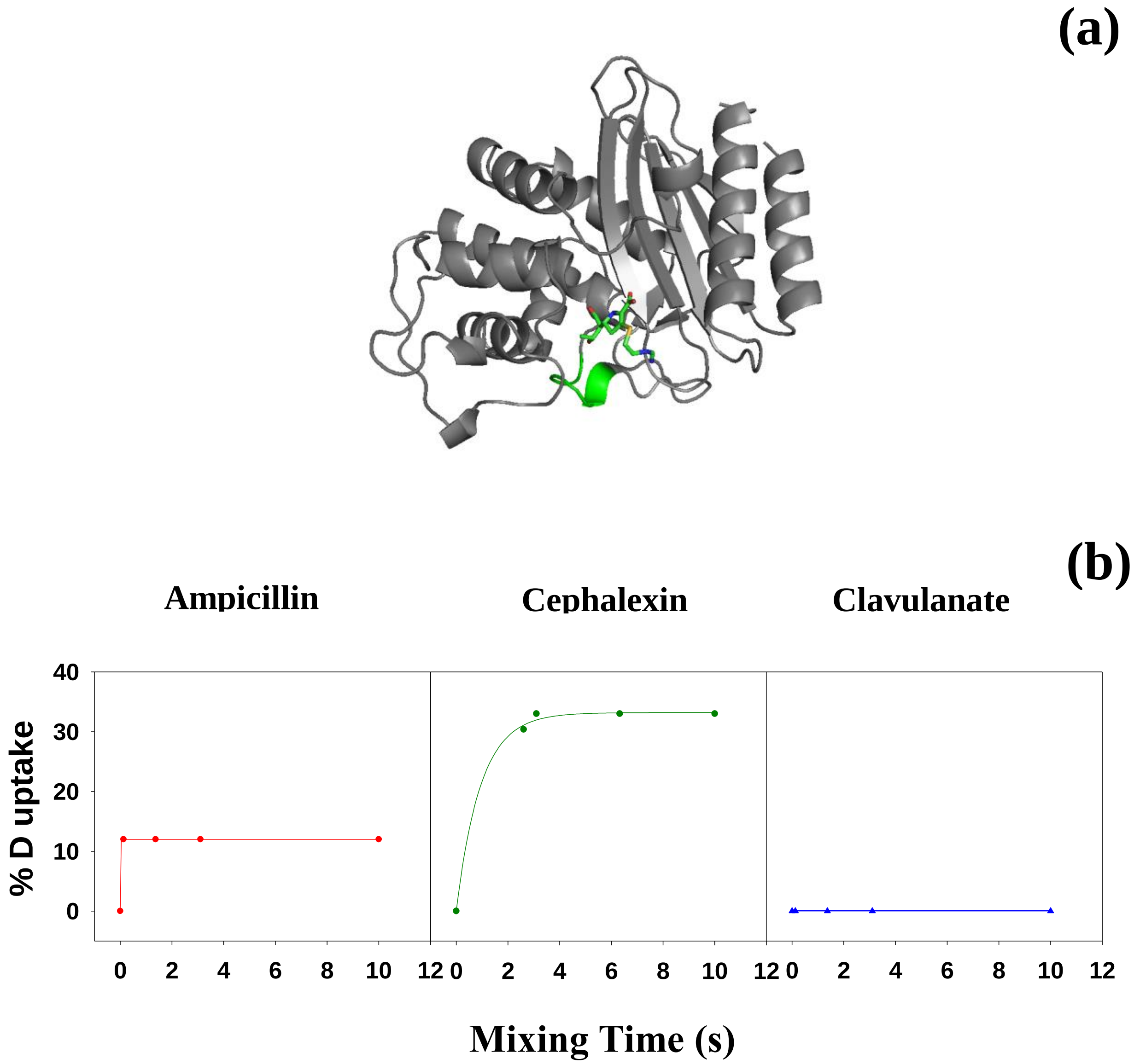

**Figure 6.2.** A comparison observed changes in dynamics associated with acylation caused by ampicillin, cephalexin and clavulanate on peptide DRWEPEL. (a) The peptide (161-167) is mapped on the 1FQG crystal structure of TEM-1. (b) HDX profile of the peptide.

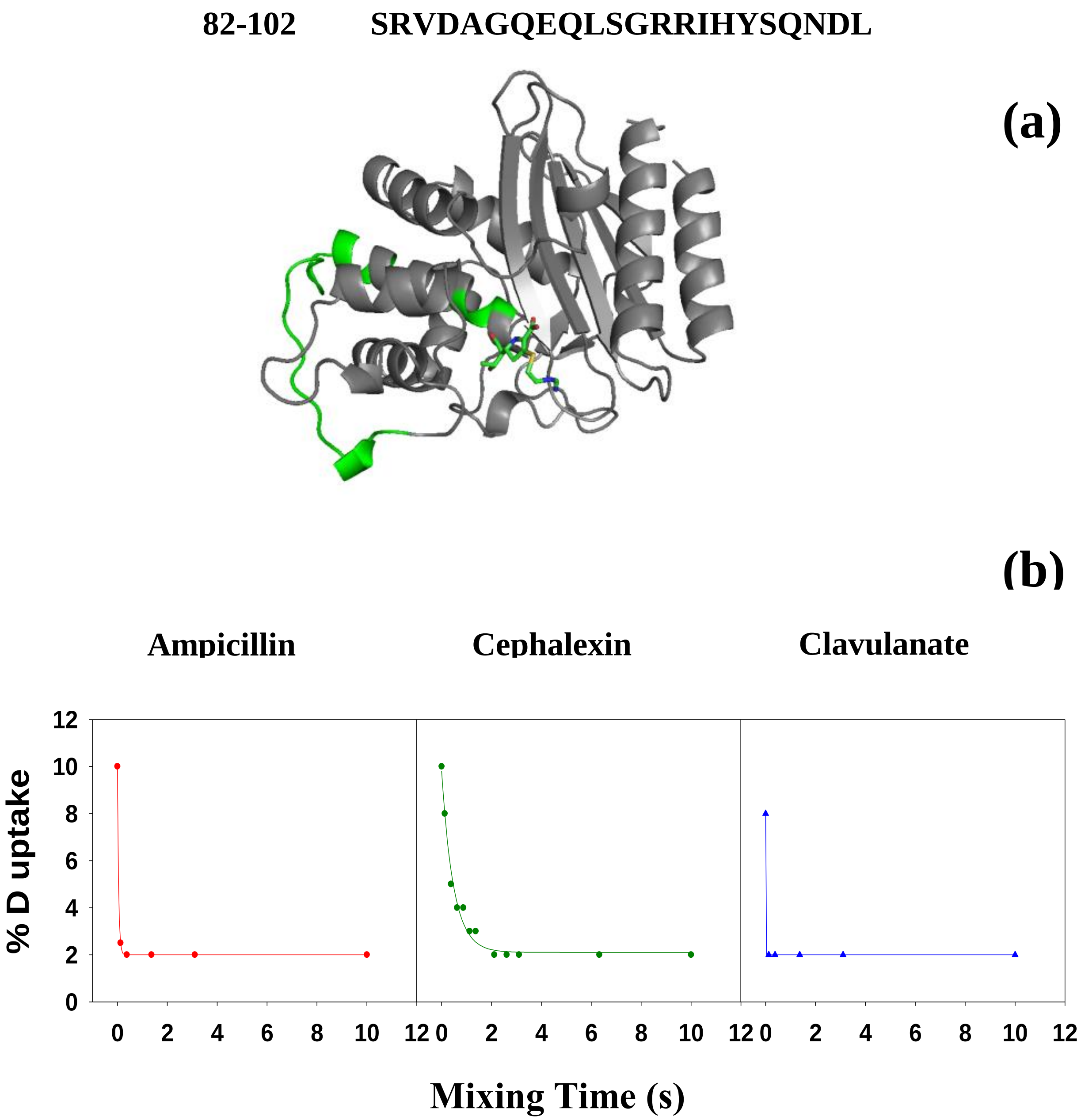

**Figure 6.3.** A comparison observed changes in dynamics associated with acylation caused by ampicillin, cephalexin and clavulanate on peptide SRVDAGQEQLSGRRIHYSQNDL. (a) The peptide (82-102) is mapped on the 1FQG crystal structure of TEM-1. (b) HDX profile of the peptide.

**105-117 SDNTAANLLLTTI**

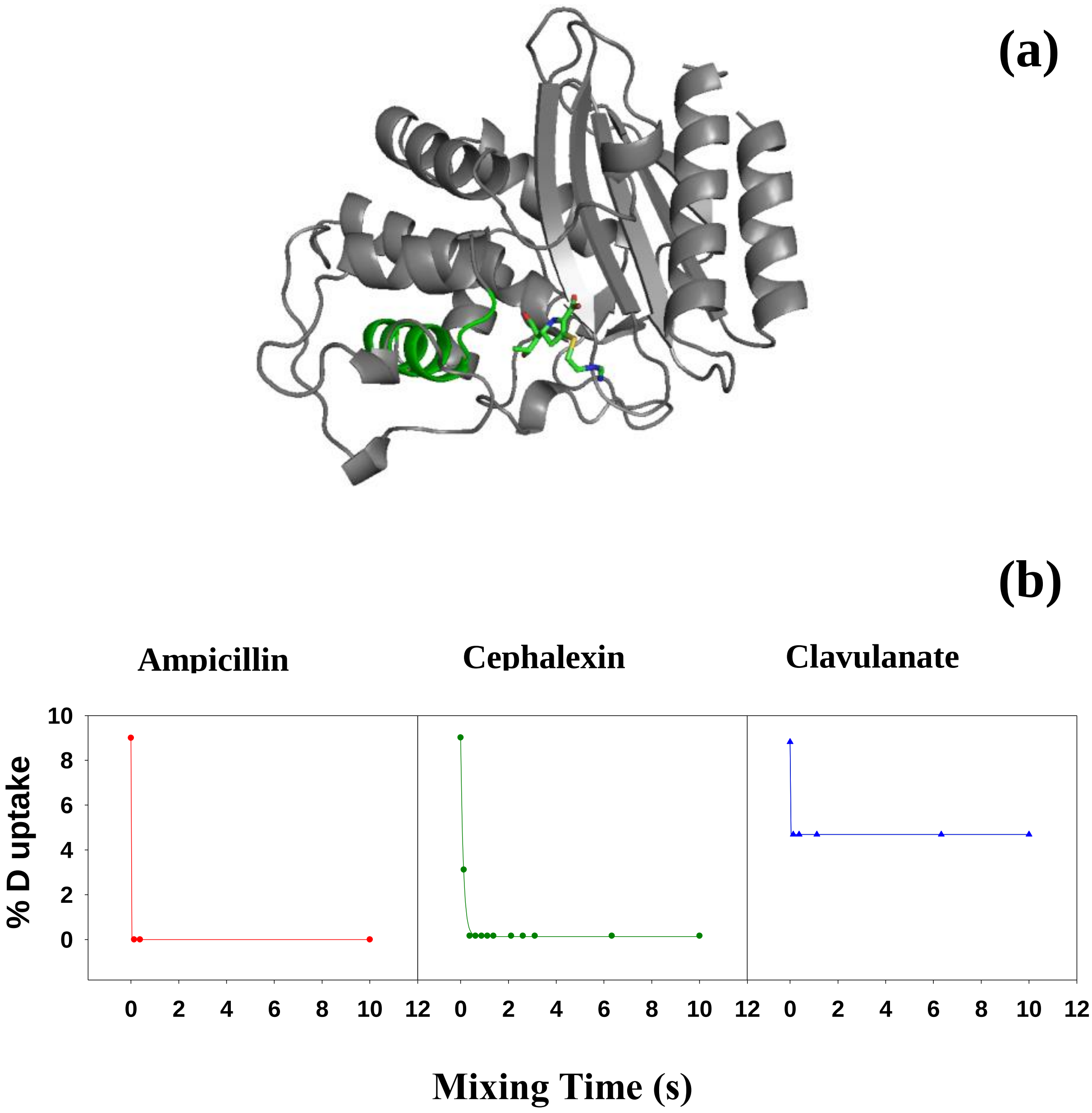

**Figure 6.4.** A comparison observed changes in dynamics associated with acylation caused by ampicillin, cephalexin and clavulanate on peptide SDNTAANLLLTTI. (a) The peptide (105-107) is mapped on the 1FQG crystal structure of TEM-1. (b) HDX profile of the peptide.

**205-223 FIADKSGAGERGSRGIIAA**

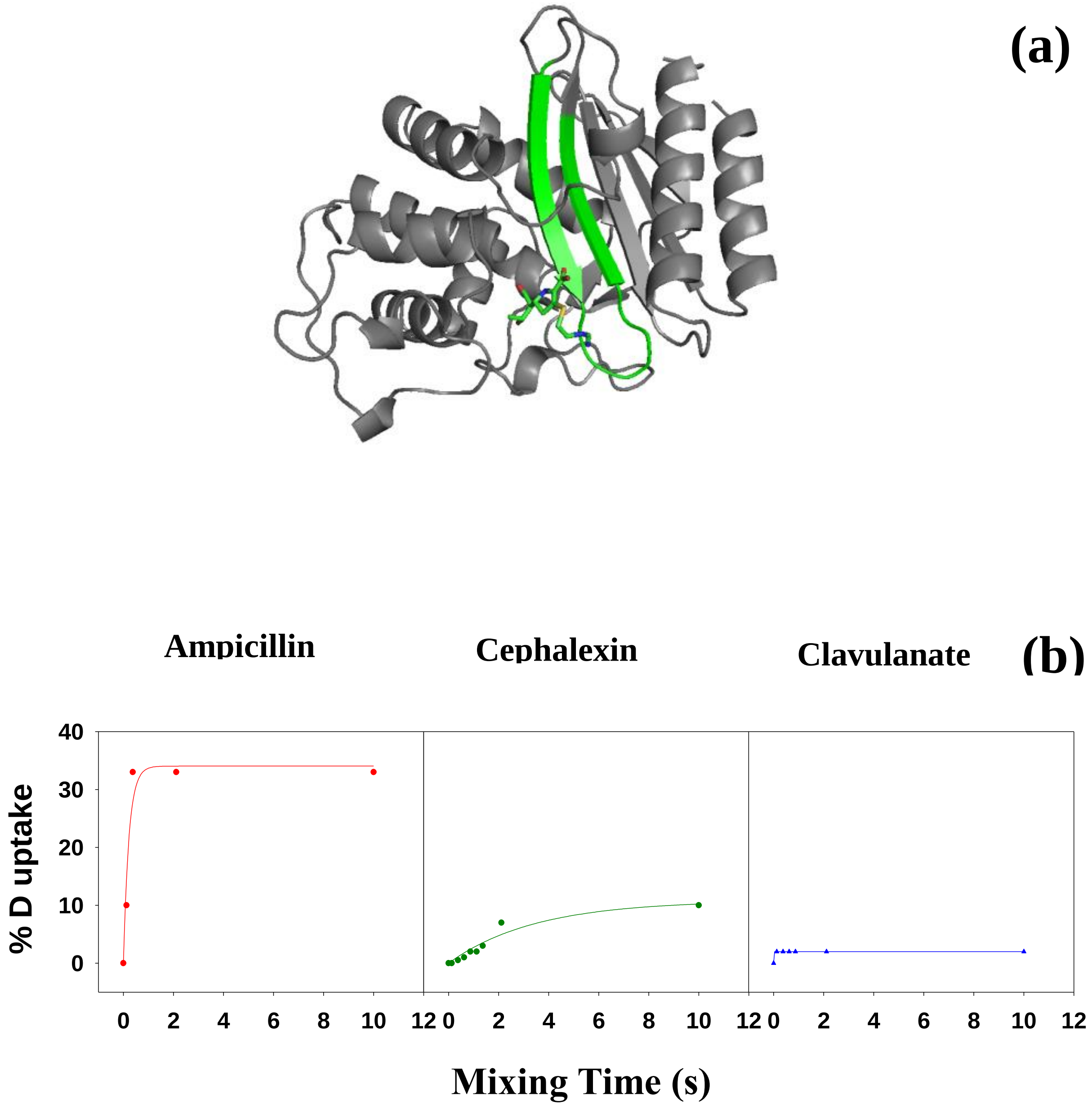

**Figure 6.5**. A comparison observed changes in dynamics associated with acylation caused by ampicillin, cephalexin and clavulanate on peptide FIADKSGAGERGSRGIIAA. (a) The peptide (205-223) is mapped on the 1FQG crystal structure of TEM-1. (b) HDX profile of the peptide.

This observation emphasizes the role of Glu166 in hydrolysis mechanism that does not occur in case of TEM-1/clavulanate system. However, the lower D-uptake by TEM-1/ampicillin system might be related to the acylation process. Ampicillin is a very good substrate of TEM-1 that is readily hydrolyzed with an exceptionally high turnover rate [28]. Therefore, most probably this loop undergoes extremely rapid fluctuations during the hydrolysis process which is not measureable under our experimental conditions and the observed D- uptake is therefore an average of those impulsive motions. Another interesting phenomenon was observed by the peptide that is neighboring the active site Ser70. In case of inhibitor, 'tightening' of the region is observed which is suggestive of locking the active site while the enzyme generally 'loosen up' to hydrolyze substrates. Therefore, the observed HDX profile can be linked to the catalytically active sites (Figure 6.6). In NMR based studies, Trp229 residue has been identified as an important modulator of allosteric communication between active site and the allosteric site. Interestingly, the peptide containing Trp229 residue shows exactly same dynamic profile in all three systems which also supports that this helix undergoes the same dynamics to serve the same purpose in all three cases [29].

Remarkably, peptides that exhibit exclusively rapid changes display dramatic correlation with the naturally occurring mutation sites. The TEM-1 variants reported to the date exhibit either point or multiple mutations at the residues 39, 69, 104, 164,166, 205, 237, 238, 239, 240, 244, 265 and 276 [10, 11, 17, 23, 25, 30]. Our observation suggests that all the residues are contained by the peptides that undergo dramatic structural change upon binding and/ or allosteric transition in all three systems that we have employed (Figure 6.2, 6.3, 6.4). In general, TEM-1 conserves specific dynamic regions that demonstrate either positive or negative conformational response towards antibiotics.

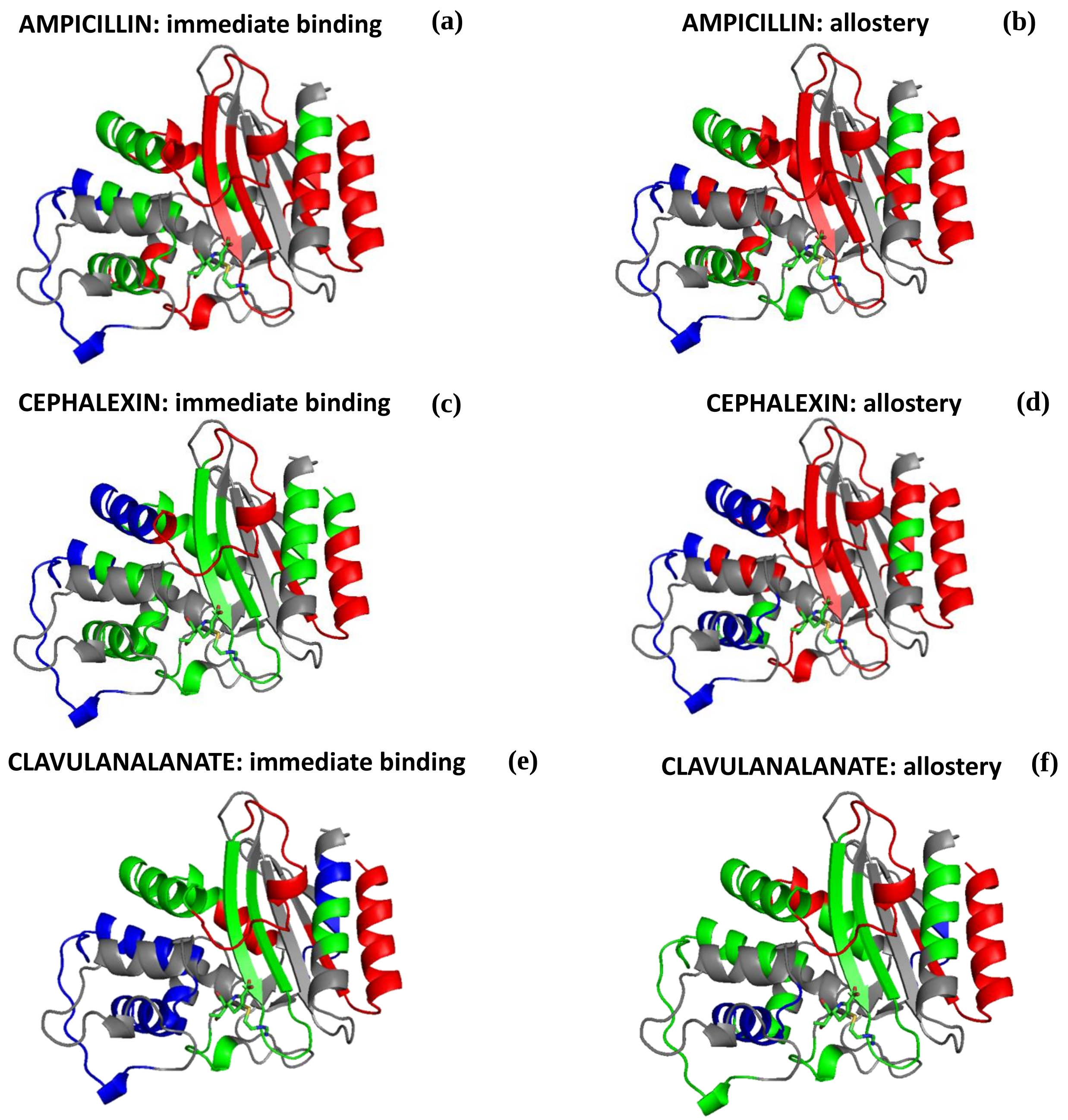

**Figure 6.6.** Changes in TEM-1 conformational dynamics upon acylation as indicated by changes in deuterium uptake. (a,c,e) Immediately upon acylation. (b,d,f) Over time after acylation. Red indicates an increase in deuterium uptake, blue indicates a decrease and green indicates no change. In (a,c,e), grey regions indicate regions where no peptides were detected. In (b,d,f) all regions that do not exhibit a slow change in deuterium uptake are grey.

Additionally, these regions are either important for catalytic activity or transmission of allosteric information [20]. This striking correlation demonstrates the potential of microfluidics enabled HDX-TRESI-MS as a powerful technique to probe the possible site of functionally relevant mutations. Conventionally, mutation sites are prepared *via* PCR based site-directed mutagenesis experimental technique or predicted by molecular simulations which are labor intense and time consuming procedures [13, 31]. As our experimental approach is extremely straightforward and simple it can be adopted as an alternative method for the prediction of mutation sites *via* the detection of allostery.

## 6.4 CONCLUSIONS

We have successfully demonstrated the utility of pulse labeling microchip as a suitable approach for comparative study of allosteric effects on enzymes upon substrate/inhibitor binding. This is a versatile technique that can be generally applicable to any enzyme / ligand system (in principle) that involves structural perturbation as a consequence of binding. In contrast to complicated and exhaustive experimental methods that are generally employed to study dynamic response of enzymes towards ligands, the current experimental approach is extremely straightforward but provides enormous amount of information. We were able to identify the dynamic regions of TEM-1 beta-lactamase that are directly involved in acylation or in close proximity of active site. The result reveals that the regions that undergo time dependent and/or abrupt structural change after binding are specifically crucial for catalytic efficiency. Interestingly the peptides that experiences extreme changes, contains residues where most of the point mutations evolved naturally. To our best knowledge this is the first experimental approach that can indirectly provide information about mutational ‘hot spots’ sites that must otherwise be obtained *via* complicated mutagenesis studies. This strong correlation demonstrates the potential of this device in rapidly predicting possible sites of mutation and can be adopted as a powerful novel approach.

# REFERENCES

1. Damblon, C., et al., *The catalytic mechanism of beta-lactamases: NMR titration of an active-site lysine residue of the TEM-1 enzyme.* Proceedings of the National Academy of Sciences of the United States of America, 1996. **93**(5): p. 1747-1752.
2. Sandanayaka, V.P. and A.S. Prashad, *Resistance to beta-lactam antibiotics: structure and mechanism based design of beta-lactamase inhibitors.* Curr Med Chem, 2002. **9**(12): p. 1145-65.
3. Bauernfeind, A., *Classification of beta-lactamases.* Rev Infect Dis, 1986. **8 Suppl 5**: p. S470-81.
4. Bush, K., *Characterization of beta-lactamases.* Antimicrob Agents Chemother, 1989. **33**(3): p. 259-63.
5. Waksman, S.A., *What is an antibiotic or an antibiotic substance?* Mycologia, 1947. **39**(5): p. 565-9.
6. Bush, K. and M.J. Macielag, *New Î²-lactam antibiotics and Î²-lactamase inhibitors.* Expert Opinion on Therapeutic Patents, 2010. **20**(10): p. 1277-1293.
7. Bush, K., G.A. Jacoby, and A.A. Medeiros, *A functional classification scheme for beta-lactamases and its correlation with molecular structure.* Antimicrob Agents Chemother, 1995. **39**(6): p. 1211-33.
8. Bush, K. and G.A. Jacoby, *Updated functional classification of beta-lactamases.* Antimicrob Agents Chemother, 2010. **54**(3): p. 969-76.
9. Meroueh, S.O., et al., *Molecular dynamics at the root of expansion of function in the M69L inhibitor-resistant TEM beta-lactamase from Escherichia coli.* J. Am. Chem. Soc., 2002. **124**(32): p. 9422-9430.
10. Sideraki, V., et al., *A secondary drug resistance mutation of TEM-1 Î²-lactamase that suppresses misfolding and aggregation.* Proceedings of the National Academy of Sciences, 2001. **98**(1): p. 283-288.

11. Zafaralla, G., et al., *ELUCIDATION OF THE ROLE OF ARGININE-244 IN THE TURNOVER PROCESSES OF CLASS-A BETA-LACTAMASES.* Biochemistry, 1992. **31**(15): p. 3847-3852.
12. Delaire, M., et al., *Site-directed mutagenesis at the active-site of escherichia-coli TEM-1 beta-lactamase - suicide inhibitor - resistant mustant reveals the role of arginine-244 and methionine-69 in catalysis.* J. Biol. Chem., 1992. **267**(29): p. 20600-20606.
13. Vakulenko, S.B., et al., *Selection and characterization of beta-lactam-beta 3-lactamase inactivator-resistant mutants following PCR mutagenesis of the TEM-1 beta-lactamase gene.* Antimicrobial Agents and Chemotherapy, 1998. **42**(7): p. 1542-1548.
14. Diaz, N., et al., *Insights into the acylation mechanism of class A beta-lactamases from molecular dynamics simulations of the TEM-1 enzyme complexed with benzylpenicillin.* Journal of the American Chemical Society, 2003. **125**(3): p. 672-684.
15. Livermore, D.M., *beta-Lactamases in laboratory and clinical resistance.* Clin Microbiol Rev, 1995. **8**(4): p. 557-84.
16. Cantu, C. and T. Palzkill, *The role of residue 238 of TEM-1 beta-lactamase in the hydrolysis of extended-spectrum antibiotics.* Journal of Biological Chemistry, 1998. **273**(41): p. 26603-26609.
17. Matagne, A., J. Lamotte-Brasseur, and J.M. Frere, *Catalytic properties of class A beta-lactamases: efficiency and diversity.* Biochem J, 1998. **330 ( Pt 2)**: p. 581-98.
18. Meneksedag, D., et al., *Communication between the active site and the allosteric site in class A beta-lactamases.* Comput Biol Chem, 2013. **43**: p. 1-10.
19. Ke, Y.Y. and T.H. Lin, *A theoretical study on the activation of Ser70 in the acylation mechanism of cephalosporin antibiotics.* Biophys Chem, 2005. **114**(2-3): p. 103-13.
20. Brown, N.G., et al., *Structural and Biochemical Evidence That a TEM-1 beta-Lactamase N170G Active Site Mutant Acts via Substrate-assisted Catalysis.* Journal of Biological Chemistry, 2009. **284**(48): p. 33703-33712.
21. Orencia, M.C., et al., *Predicting the emergence of antibiotic resistance by directed evolution and structural analysis.* Nat. Struct. Biol., 2001. **8**(3): p. 238-242.

22. Bradford, P.A., *Extended-spectrum beta-lactamases in the 21st century: characterization, epidemiology, and detection of this important resistance threat.* Clin Microbiol Rev, 2001. **14**(4): p. 933-51, table of contents.
23. Cantu, C., W.Z. Huang, and T. Palzkill, *Cephalosporin substrate specificity determinants of TEM-1 beta-lactamase.* Journal of Biological Chemistry, 1997. **272**(46): p. 29144-29150.
24. Petrosino, J.F. and T. Palzkill, *Systematic mutagenesis of the active site omega loop of TEM-1 beta-lactamase.* J Bacteriol, 1996. **178**(7): p. 1821-8.
25. Bouthors, A.T., et al., *Role of residues 104, 164, 166, 238 and 240 in the substrate profile of PER-1 beta-lactamase hydrolysing third-generation cephalosporins.* Biochem J, 1998. **330 ( Pt 3)**: p. 1443-9.
26. Swaren, P., et al., *X-ray structure of the Asn276Asp variant of the Escherichia coli TEM-1 beta-lactamase: Direct observation of electrostatic modulation in resistance to inactivation by clavulanic acid.* Biochemistry, 1999. **38**(30): p. 9570-9576.
27. Natalie C. J. Strynadka, R.M., S.E. Jensen, Marvin Gold and J. Bryan Jones, *Structure Based Design of a Potent Transition State Analogue for TEM-1 beta-Lactamase.* Nat. Struct. Biol., 1996. **3**(8): p. 688-695.
28. Miyashita, K., I. Massova, and S. Mobashery, *Quantification of the extent of attenuation of the rate of turnover chemistry of the TEM-1 β-lactamase by the α-1R-hydroxyethyl group in substrates.* Bioorganic & Medicinal Chemistry Letters, 1996. **6**(3): p. 319-322.
29. Meneksedag, D., et al., *Communication between the active site and the allosteric site in class A beta-lactamases.* Computational Biology and Chemistry, 2013. **43**(0): p. 1-10.
30. Knox, J.R., *EXTENDED-SPECTRUM AND INHIBITOR-RESISTANT TEM-TYPE BETA-LACTAMASES - MUTATIONS, SPECIFICITY, AND 3-DIMENSIONAL STRUCTURE.* Antimicrobial Agents and Chemotherapy, 1995. **39**(12): p. 2593-2601.
31. Lenfant, F., et al., *Site-directed mutagenesis of beta-lactamase TEM-1. Investigating the potential role of specific residues on the activity of Pseudomonas-specific enzymes.* Eur J Biochem, 1993. **217**(3): p. 939-46.

# CHAPTER 7

## SUMMARY AND FUTURE DIRECTION

This thesis introduces a simple, cost effective and highly reproducible microfluidic device fabrication protocol which enables integration of multiple functionalities on a common platform to develop custom polymeric microfluidic devices. These devices are directly interfaced with mass spectrometry as an alternative electrospray ionization source to conduct site specific mass spectrometric analysis on protein samples. This thesis also describes the application of these microfluidic devices in studying proteins dynamics and/or kinetics of weakly structured proteins and/or intrinsically disordered proteins that are unattainable by other conventional biophysical techniques.

Chapter 2 introduces a quick, economical, straightforward and highly reproducible fabrication protocol that is suitable for rapid prototyping. Using this new technique, a microfluidic module was developed that supports millisecond time scale rapid mixing followed by mass spectrometric analysis. The device performance was verified by an acid induced unfolding of cytochrome c. An analytical frame work for analyzing the resultant data was also introduced. This microfluidic device enables us to identify a previously unreported native-like intermediate in the acid induced unfolding of cytochrome c.

In Chapter 3, we successfully introduce a novel multistep microfluidic reactor that incorporates entire MS based HDX work flow on a single platform enabling direct measurements of rapid fluctuations in proteins on millisecond time-scale on a single online experiment. The microfluidic framework provides rapid mixing and continuous labeling on millisecond timescale followed by rapid quenching of labeling reaction for proteolytic degradation which was then directly introduced to Mass spectrometer. The device performance was tested by acquiring a single time point (100 ms) measurement of native state ubiquitin. HDX profile of ubiquitin was achieved through extensive data analysis which enables structural analysis of native state ubiquitin and clearly demonstrates the potential application of this integrated device.

This unique device is also applied to achieve a detailed time course HDX profile of native state cytochrome c (80ms to 10s) at physiological pH 7.6 which enables us to distinguish the dynamic behaviour of different loops at ms time scale. The observed dynamics suggests a reasonable agreement between the reported X-ray structure and the solution conformation under our experimental condition. Only the ‘heme’ bound loop showed significant deviation suggesting that this approach can clearly demonstrate and distinguish loop dynamics. Our observations correlate well with studies conducted in other orthogonal manner (HDX NMR) but appear to be much easier to conduct which shows the potential of this device to be adopted as an alternative methodology for studying protein conformations.

This integrated continuous labeling device is also applied to established the dynamics of DAHP synthase in absence of its substrate and compared to its available substrate bound crystal structure (1KFL) through acquiring HDX profile of free DAHP synthase (40 ms to 10 sec). Our data suggests that the free and the substrate bound forms have structural similarities only at the tetramer interface but significantly differ near the active site of the enzyme which suggests that the unbound enzyme undergoes ‘molten-globule-like’ conformational dynamics. Differences in the dynamics are concentrated to a region surrounding the active site which is largely helical in the substrate-bound species. But this region shows loop-like dynamics in the unbound protein which develops into partial structures upon substrate binding.

Chapter 4 is a continuation work of Chapter 3 where conformational changes in DAHP synthase upon ligand (substrate and different inhibitors) binding are probed *via* continuous labeling HDX experiments. Extensive data analysis helps us to characterize substantial differences in dynamics near the active sites of the enzymes among the apo and different holo enzymes. This work can be further extended by investigating global HDX of tetramer with response to all of these small molecules (substrates/ inhibitor) followed by a rapid degradation into individual monomers prior to ionization. This proposed experiment can provide us information about the asymmetric binding of the subunits and eventually will be beneficial in finding the differential dynamic behaviour of the individual monomers.

Chapter 5 introduces a pulse labeling microfluidic device that is complementary to the device described in Chapter 3. This integrated microfluidic reactor enables direct measurement of structural changes and dynamics in TEM1 β-lactamase protein due to allosteric inhibition. The observed results show some fascinating correlations with mutagenesis studies that  demonstrates the power of microfluidics enabled sub-second HDX pulse labeling as a tool for studying allostery.

The utility of this microchip is further extended in Chapter 6 where it is applied for comparative study of allosteric effects on TEM-1 upon binding to its inhibitor, good and poor substrates.  The result indicates that the regions that exhibit time dependent dynamic behaviour after binding are the regions where most of the mutations occur naturally. This intriguing correlation demonstrates the potential of this device in predicting possible sites of functionally relevant mutation and can be adopted as a novel approach in measuring allosteric interaction to predict possible sites of mutation.

In recent years, MS based HDX technique has significantly contributed in characterizing biopharmaceuticals. HDX-MS provides detailed information of inherent specificity of small drug targets with large protein molecules [1]. The approach of this dissertation work is not limited to only studying protein conformations but can also be stretched to active surface guided drug designing by measuring effect of protein- drug binding. Inherent specificity of a possible drug candidate and their alternative modes of action can be determined effectively using our microfluidic reactor facilitating Epitope mapping. Epitope mapping on microfluidic platform is an innovative approach and therefore we have applied for an intellectual property (patent) to Innovation York titled ‘Time-resolved Hydrogen Deuterium Exchange With Spatial Resolution for Epitope Mapping’ which is currently under review process at MaRS innovation Centre, ON.

Our microfluidic TR-ESI reactor is advantageous compare to all other contemporary MS and NMR based analytical techniques that utilizes HDX. In conventional experimental approaches, LC separation is an essential step which is not required in our experimental set up reducing the experimental period significantly. Using microfluidic platform, a complete data acquisition period for acquiring 10 HDX time points is less than 2 hours for one protein sample. This is advantageous in epitope mapping as many antigen and/or antigen-monoclonal antibody complex have short life span and requires quick data acquisition. NMR and MS based conventional HDX techniques are compared with microfluidic TR-ESI reactor in Table 7.1.

**Table 7.1.** Comparison of microfluidic TR-ESI rector with contemporary analytical techniques using HDX in protein conformational studies

| | Microfluidic TRESI HDX-MS | Conventional HDX-MS | Conventional HDX-NMR |
|---|---|---|---|
| Sample quality | Moderately pure | Moderately pure | Pure |
| Solvent compatibility | LC-MS friendly buffer or solvent and non-reacting with PMMA | Any LC-MS friendly buffer or solvent | Deuterated NMR solvent where the peptides are soluble |
| Total data acquisition period per time point | 8 s | 30 min to 1 hr | 30 min to 1 hr |
| Data acquisition period per scan | Milliseconds | Milliseconds | Few seconds |
| HDX labeling time | 40 ms to 24 hrs | 1 hr to 24 hr | 1hr to 24 hr |
| LC separation | Not required | ~15 min to 8 hr | ~15 min to 8 hr |
| Online/offline measurement | Online | Online | Offline |
| Temperature controller | Not required | Required | Required |
| Data Interpretation | Manual | Software assisted | Manual |

Due to the novelty and simplicity of our approach, many MS-based industries have shown interest in our microfluidic enabled ESI source. Currently we are in a process of collaboration with industries for commercialization of our enzymatic micro-reactor which will also integrate our approach with currently available data analysis software. Proper software assisted data interpretation can reduce the data analysis time significantly which is the only downside of TRESI compared to currently available commercial techniques. Commercialization of this micro-reactor will significantly increase the scope of HDX-MS and hopefully the HDX community will embrace this technique to explore many innovative applications including routine investigation of drug targets.

The scope of this dissertation work can be further extended through integrating more functional modules and also by improving the existing fabrication technique. Furthermore, these integrated devices can be interfaced with a high resolution MS which is capable of performing ion mobility on the resulting peptides to demonstrate further conformational information. Since ECD or ETD techniques are not amenable to large proteins, it is not possible to obtain single spatial resolution on huge protein or protein-complex samples.  In those cases, these devices can be applied as a “middle-down” approach to generate relatively smaller peptides than intact protein which are easily subjected to ECD or ETD fragmentation.

With the advents in MS instrumentation, software and methodologies, HDX is becoming more dominating technique in studying protein conformations, epitope mapping, comparability study and higher order protein structure determination [2]. Our device is a promising addition which allows incorporation of many new functionality such as desalting module and/or separation module if required for such studies.  These micro reactors are powerful tools that might have many other fascinating applications which need to be explored in future.

# REFERENCES

1. Houde, D., et al., *Characterization of IgG1 Conformation and Conformational Dynamics by Hydrogen/Deuterium Exchange Mass Spectrometry.* Anal Chem, 2009. **81**(14): p. 5966.

2. Wei, H., et al., *Hydrogen/deuterium exchange mass spectrometry for probing higher order structure of protein therapeutics: methodology and applications.* Drug Discovery Today, 2014. **19**(1): p. 95-102.